Insititut für Erd- und Umweltwissenschaften • Mathematisch Naturwissenschaftliche Fakultät •
Universität Potsdam

Seasonal precipitation, river discharge, and sediment flux in the western Himalaya

Hendrik Wulf

Dissertation
zur Erlangung des akademischen Grades
Doktor der Naturwissenschaften (Dr. rer. nat.)
in der Wissenschaftsdisziplin Geoökologie

eingereicht an der
Mathematisch-Naturwissenschaftlichen Fakultät
der Universität Potsdam

Potsdam, im August 2011

für Luigi & Andi

Abstract

Rainfall, snow-, and glacial melt throughout the Himalaya control river discharge, which is vital for maintaining agriculture, drinking water and hydropower generation. However, the spatiotemporal contribution of these discharge components to Himalayan rivers is not well understood, mainly because of the scarcity of ground-based observations. Consequently, there is also little known about the triggers and sources of peak sediment flux events, which account for extensive hydropower reservoir filling and turbine abrasion. We therefore lack basic information on the distribution of water resources and controls of erosion processes.

In this thesis, I employ various methods to assess and quantify general characteristics of and links between precipitation, river discharge, and sediment flux in the Sutlej Valley. First, I analyze daily precipitation data (1998-2007) from 80 weather stations in the western Himalaya, to decipher the distribution of rain- and snowfall. Rainfall magnitude frequency analyses indicate that 40% of the summer rainfall budget is attributed to monsoonal rainstorms, which show higher variability in the orogenic interior than in frontal regions. Combined analysis of rainstorms and sediment flux data of a major Sutlej River tributary indicate that monsoonal rainfall has a first order control on erosion processes in the orogenic interior, despite the dominance of snowfall in this region.

Second, I examine the contribution of rainfall, snow and glacial melt to river discharge in the Sutlej Valley ($\sim$55,000 km^2), based on a distributed hydrological model, which covers the period 2000-2008. To achieve high spatial and daily resolution despite limited ground-based observations the hydrological model is forced by daily remote sensing data, which I adjusted and calibrated with ground station data. The calibration shows that the Tropical Rainfall Measuring Mission (TRMM) 3B42 rainfall product systematically overestimates rainfall in semi-arid and arid regions, increasing with aridity. The model results indicate that snowmelt-derived discharge

(74%) is most important during the pre-monsoon season (April to June) whereas rainfall (56%) and glacial melt (17%) dominate the monsoon season (July-September). Therefore, climate change most likely causes a reduction in river discharge during the pre-monsoon season, which especially affects the orogenic interior.

Third, I investigate the controls on suspended sediment flux in different parts of the Sutlej catchments, based on daily gauging data from the past decade. In conjunction with meteorological data, earthquake records, and rock strength measurements I find that rainstorms are the most frequent trigger of high-discharge events with peaks in suspended sediment concentrations (SSC) that account for the bulk of the suspended sediment flux. The suspended sediment flux increases downstream, mainly due to increases in runoff. Pronounced erosion along the Himalayan Front occurs throughout the monsoon season, whereas efficient erosion of the orogenic interior is confined to single extreme events.

The results of this thesis highlight the importance of snow and glacially derived melt waters in the western Himalaya, where extensive regions receive only limited amounts of monsoonal rainfall. These regions are therefore particularly susceptible to global warming with major implications on the hydrological cycle. However, the sediment discharge data show that infrequent monsoonal rainstorms that pass the orographic barrier of the Higher Himalaya are still the primary trigger of the highest-impact erosion events, despite being subordinate to snow and glacially–derived discharge. These findings may help to predict peak sediment flux events and could underpin the strategic development of preventative measures for hydropower infrastructures.

Zusammenfassung

Regen, Schnee- und Gletscherschmelze speisen die Flüsse des Himalajas, die eine große Bedeutung für die Landwirtschaft, Trinkwasserversorgung und Wasserkraftnutzung in Südasien aufweisen. Welchen Anteil die einzelnen Abflusskomponenten am Gesamtabfluss in Raum und Zeit besitzen, ist jedoch kaum quantifiziert, da es in der entlegenen Region an Bodenmessstationen mangelt. Aus diesem Grund ist auch wenig über die Auslöser und Herkunftsgebiete von hohen Sedimentaustragsereignissen bekannt, die im erheblichen Maße dazu beitragen, dass die Kapazität von Wasserkraftreservoiren abnimmt und Wasserkraftturbinen abradieren. Daher fehlen bisher grundlegende Informationen zur räumlichen Verteilung von Wasserressourcen und zu den Ursachen von Erosionsprozessen.

In dieser Arbeit benutze ich verschiedene Methoden um die Eigenschaften von und die Beziehungen zwischen Niederschlag, Abflussmenge und Sedimentaustrag im Sutlej-Tal zu untersuchen. In einer ersten Studie analysiere ich Tagesniederschläge (1998-2007) von 80 Wetterstationen aus dem westlichen Himalaja, um die räumliche Verteilung von Regen- und Schneeniederschlägen zu charakterisieren. Die weitere Analyse der Magnituden-Häufigkeitsverteilung von Regenfällen zeigt, dass 40% der sommerlichen Niederschläge auf monsunale Starkregenereignisse zurückgehen, die eine höhere Variabilität im Gebirgsinneren aufweisen als an der Gebirgsfront. Die Kombination von Niederschlagsdaten mit Sedimentaustragsdaten für einen der größten Zuflüsse des Sutlejs zeigt, dass monsunaler Niederschlag der primäre Auslöser von Erosionsprozessen im Gebirgsinneren ist, ungeachtet größerer Abflussmengen durch Schnee- und Gletscherschmelze.

In einer zweiten Studie untersuche ich den Beitrag von Regen, Schnee- und Gletscherschmelze zur Abflussmenge im Sutlej-Tal (∼55.000 km^2) mit Hilfe eines hydrologischen Modells für den Jahreszeitraum 2000-2008. Um trotz der begrenzten Bodenmessungen eine hohe räumliche und zeitliche Auflösung zu erzielen, basiert das Modell auf täglichen Fernerkundungsdaten, die ich mit allen verfügbaren Bodenstationsdaten kalibriert und an diese angepasst habe. Die Kalibrierung zeigt, dass das Regenniederschlagsprodukt 3B42 der „Tropical Rainfall Measuring Mission“ (TRMM) den Bodenniederschlag in den semi-ariden bis ariden Gebirgsregionen mit zunehmender Trockenheit systematisch überschätzt. Die Modellierungsergebnisse verdeutlichen, dass die Schneeschmelze den bedeutendsten Beitrag zur Abflussmenge (74 %) zwischen April und Juni aufbringt, während Regen (56%) und Gletscherschmelze (17%) die Monsunsaison (Juli-September) prägen. Daher ist anzunehmen, dass der Klimawandel zu einer Verringerung der Abflussmenge zwischen April und Juni führen wird, was sich besonders auf das Gebirgsinnere auswirkt.

In einer dritten Studie untersuche ich mit Hilfe von täglichen Messdaten der letzten Dekade die Ursachen und Eigenschaften des Sedimentaustrags in verschiedenen Bereichen des Sutlej-Einzugsgebietes. Auf der Grundlage von meteorologischen Daten, Erdbebenaufzeichnungen und Gesteinsfestigkeitsmessungen identifiziere ich Starkregenereignisse als häufigste Ursache für extreme Erosionsereignisse, die einen Großteil des gesamten Sedimentaustrags ausmachen. Großräumig betrachtet nimmt der Sedimentaustrag flussabwärts zu, was hauptsächlich auf den Anstieg der Abflussmenge zurückzuführen ist. Zur Monsunzeit treten Erosionsprozesse entlang der Himalajafront besonders häufig auf, während im Gebirgsinneren die Erosion auf einzelne Extremereignisse beschränkt ist.

Die Ergebnisse dieser Arbeit untersteichen die Bedeutung von Schnee- und Gletscherschmelze im westlichen Himalaja, in dem große Gebiete nur vereinzelt von monsunalen Niederschlägen erreicht werden. Diese Gebiete sind daher besonders anfällig für den Klimawandel mit weitreichenden Konsequenzen für den Wasserhaushalt in der Region. Die Analyse von Sedimentaustragsdaten zeigt jedoch, dass vereinzelte monsunale Regenstürme, welche die topographische Barriere des Himalaja überqueren, die primäre Ursache von extremen Erosionsereignissen sind, trotz der größeren Abflussmengen von Schnee- und Gletscherschmelze im Gebirgsinneren. Diese Ergebnisse können dazu beitragen, große Erosionsereignisse vorherzusagen und vorbeugende Maßnahmen zum Schutz von Wasserkraftanlagen zu entwickeln.

Contents

List of Figures

List of Tables

Acknowledgements

First and foremost, I wish to express my gratitude to Dirk Scherler and Bodo Bookhagen for their expertise, guidance, and patience throughout this project. Dirk, your persistent help and constructive feedback was invaluable to me. You have been great in keeping me focused on the important things and sparking new ideas to master challenges. Bodo, you have been an excellent mentor for me. I am very grateful that you showed responsibility for my work and I thank you for a wonderful time in Santa Barbara.

I am particularly indebted to Manfred Strecker, who first sparked my passion for Earth Science and opened many doors along the way. Thank you Manfred for your enduring support and for wonderful field trips to the Rift Valley and the Himalaya.

This work would not have been possible without the generous support of Tashi Tsering Lonpo, Swami Ray, Bishan Lal, and Clara Chrzanowski during the fieldwork. I am very grateful for all the discoveries, experiences, and lessons you taught me.

This research was financed by a fellowship from the DFG (Deutsche Forschungsgemeinschaft) Graduate School GK1364 "Climate and Tectonics in the African-Asian monsoonal region" and a DAAD (Deutscher Akademischer Austausch Dienst) fellowship that enabled a 4-month stay at the University of California in Santa Barbara, USA. Thanks especially to all the countless people who made the Graduate School happen, and all the fellow PhD students for having a good time together.

In particular, I would like to thank Helmut Elsenbeer, Andreas Bergner, Rasmus Thiede, Birgit Fabian, Hauke Sattler and Daniel Vollmer for their support in various practical and technical issues.

There are several people who became dear friends during the years, and who I would like to thank for all the laughter, adventures, and magnificent moments that we shared. Henry Wichura, Heiko Pingel, Conni Hammer, Ulrich Knieß, Nicolas Kühn and Annett Junginger had been great mates since the very first days of University. I really appreciate that Angela Landgraf, Esther Hintersberger, Johanna Meyer, Jessica Zamangi, and Paolo Ballato became close companions. I am especially glad that Ryan Perroy, Burch Fisher, Frank Bäse, Peter Vorphal and Anna Schürkmann shared a common fate with me in the office.

Most important, I am deeply grateful for the support and love from my family. The confidence and sympathy of my parents paved the way to this thesis. The laughter of Laila and Casimir kept me going through all the hard times - it is just a pleasure to see you growing up. And of course “Luigi”, you made this all possible – thanx!

Matt, thank you, too!

Chapter 1

Introduction

Intense precipitation throughout the Himalaya provides a valuable natural resource for increasing water demands of growing populations and developing economies in central and southern Asia [e.g. *Barnett et al.*, 2005; *Garg and Hassan*, 2007]. However, securing the water supply to this region is a fundamental challenge, because of unsustainable groundwater depletion [*Garg and Hassan*, 2007; *Rodell et al.*, 2009] and the impacts of climate change on the hydrological cycle [*McDonald et al.*, 2011]. Although the effects of climate change on monsoon rainfall are still debated [*Duan et al.*, 2006; *Kumar et al.*, 2011; *Meehl and Washington*, 1993] an increase of extreme rainstorm events at the expense of more moderate events has been observed in central India [*Goswami et al.*, 2006]. Concurrently, meteorological data from the Himalaya and the Tibetan Plateau indicate reductions in snowfall during the past few decades [*Liu and Chen*, 2000; *Shekhar et al.*, 2010; *Yao et al.*, 2006], while the most conspicuous impact of climate change is probably the widespread melting and retreat of Himalayan glaciers [*Bhambri and Bolch*, 2009; *Kehrwald et al.*, 2008; *Scherler et al.*, 2011a]. To predict and mitigate the socio-economic impacts of climate change, however, requires rigorous assessments and quantifying the links between climate, hydrology, and surface processes.

Recent and expected future reductions in snow and ice cover reduce water storage capacities, which are thought to make an important contribution to river runoff in the western Himalaya [*Bookhagen and Burbank*, 2010; *Immerzeel et al.*, 2010]. The associated modifications of runoff patterns probably increase downstream runoff variability due to enhanced direct rainfall runoff [*Eriksson et al.*, 2009]. However, quantitative assessments of the hydrologic components and their relative contribution to river discharge are rare and include large uncertainties [*Braun et al.*, 1993; *Kumar et al.*, 2007b; *Singh and Jain*, 2003]. Due to the lack of comprehensive ground-based observations [*Winiger et al.*, 2005], detailed knowledge of precipitation patterns and glacial mass balances are limited [*Lang and Barros*, 2004; *Putkonen*, 2004; *Wagnon et al.*, 2007]. However, recent advances in hydrological research that are based on time series of high-resolution remote sensing imagery that account for the high spatial heterogeneity of climate and surface processes in alpine terrain [*Bales et al.*, 2006; *Bookhagen and Burbank*, 2010; *Molotch and Norte*, 2009]. Accurate assessments of major hydrological components are vitally important, because they define the boundary conditions and thus the outcome of any hydrological modeling study addressing climate change impacts in the Himalaya [*Akhtar et al.*, 2008; *Immerzeel et al.*, 2010; *Singh and Bengtsson*, 2004].

The impressive relief of the Himalaya is sculptured by the interplay between tectonic and isostatic forcing of the crust and erosional processes acting on the landscape [*Hodges*, 2000]. Documenting rates, patterns, and processes of erosion is crucial for understanding how mountainous regions evolve [*Small and Anderson*, 1995; *Molnar and England*, 1990]. Moreover, hillslope erosion delivers sediments to streams and therefore alters aquatic habitats [e.g. *Meehan*, 1991] and limits the operational life span of engineering reservoirs. Whereas, long-term perspectives ($>10^3$ yr) on erosion and landscape evolution can be derived from thermochronological methods [e.g. *Reiners et al.*, 2005] or cosmogenic radionuclides [e.g. *Bierman and Steig*, 1996; *von Blanckenburg*, 2005], direct measurements of sediment yields, typically spanning years to decades may provide valuable insights into the causes and mechanisms of the underlying erosional processes [*Meade*, 1988].

Precipitation, temperature, and vegetation exert a primary control on both chemical weathering and physical erosion [*Edmond and Huh*, 1997; *West et al.*, 2005; *White and Blum*, 1995]. In particular, precipitation governs the occurrence and magnitude of fluvial and glacial erosion [e.g. *Hallet et al.*, 1996; *Owen et al.*, 2005; *Roe*, 2003], which are efficient processes to redistribute material. Especially extreme weather events, like rainstorms, can have a profound impact on the character and rates of surface erosion processes [*Baker and Kale*, 1998; *Bookhagen et al.*, 2005a; *Coppus and Imeson*, 2002; *Hartshorn et al.*, 2002]. Heavy rainstorms in the Himalaya repeatedly cause devastating floods and landslides, which result in loss of life and property, and mobilize large sediment volumes that damaged hydropower infrastructures [*Houze et al.*, 2011; *Webster et al.*, 2011][International Disaster Data Base, http://www.emdat.be]. For the next century, it is projected that more intense and increasingly direct rainfall runoff will lead to more flooding and landsliding [*Chalise and Khanal*, 2001; *Immerzeel*, 2008; *Kumar et al.*, 2011]. Likewise, recent increases in surface temperatures increased the flood risk imposed by glacial lakes and caused widespread permafrost degradation, which in turn decreases the slope stability and enhances erosion processes [*Cheng and Wu*, 2007; *Eriksson et al.*, 2009; *Lawrence and Slater*, 2005; *Zhao et al.*, 2004]. These alarming trends and prospects, however, are based on comparably little ground-based data, which suggests that our knowledge of the various processes accounting for surface erosion and sediment evacuation in different climatic region of the Himalaya is still limited.

In summary, current research identifies several key questions related to climate, hydrology, and erosion within the Himalaya:

- *How is precipitation distributed and how does it control erosion processes?*
- *What are the relative contributions of rainfall, snow, and ice melt to the discharge of Himalayan rivers, and how may these change in the future?*
- *Which processes control the spatial pattern of contemporary surface erosion?*

The goal of this thesis is to provide answers to these and related questions through a better understanding of the coupled variations in precipitation, snow and ice melt, river discharge, and sediment flux in the western Himalaya, both, in space and time. To achieve this, I combined analysis of a unique and dense dataset of meteorological and river discharge data from the Sutlej catchment, with remote-sensing analysis, and hydrological modeling. This approach allows me to link the high temporal resolution of ground-based observations with the high spatial resolution of remote-sensing data to provide an assessment of regional water resources.

In the following second chapter, I provide a detailed introduction to the study area and its climatic, hydrologic, and erosional characteristics. In chapter 3, I investigate temporal and spatial precipitation gradients, rainstorm characteristics and their impact on fluvial sediment flux in parts of the Sutlej catchment in the western Himalaya. Based on a unique dataset of 80 weather stations, which cover a wide range of elevations (0.4-4.1 km) and contrasting climatic regions, I distinguish moisture supply from monsoonal and westerly sources. Magnitude-frequency relations of rainstorms at the humid orogenic front and semi-arid orogenic interior show characteristic differences and I relate these storm events to erosional processes in the orogenic interior by a case study of river and sediment discharge from the Baspa catchment, a major tributary of the Sutlej.

During the past decades hydrological research focused predominantly on the monsoonal system, as variations in summer rainfall are directly tied to the economic strength of India [*Kumar et al.*, 2011]. In contrast, winter snowfall derived from westerly moisture sources received little attention, despite its major contribution to river discharge in the western Himalaya [*Bookhagen and Burbank*, 2010]. In chapter 4, I develop a hydrological model to analyze the spatiotemporal distribution of water resources and river runoff components in the Sutlej catchment, western Himalaya. The model is based on daily remote-sensing data sets that I adjust and calibrate with ground-based observations. The model is validated based on nine gauging stations within the Sutlej Valley and reveals large spatial and temporal variations in the runoff contribution of rainfall, snow-, and glacial melt. Based on the modeling results, I draw conclusions regarding the likely impact of warming temperatures on river discharge in this region.

Trends in river discharge are of vital interest for the hydropower industry, like sediment flux, which accounts for extensive reservoir filling and turbine abrasion. In chapter 5, I investigate spatiotemporal trends in suspended sediment flux as well as triggers and sources of extreme sediment flux events. Based on eight river gauging stations in the Sutlej Valley and remotely sensed rainfall and snow cover data, air temperature and earthquake records, as well as rock strength measurements I infer relationships between peak sediment discharges and rainstorms, floods, and glacial discharge events. Furthermore, I analyze the sediment flux records in comparison with other published records from the Himalaya and draw some general conclusions about spatial erosion patterns and sediment sources.

The contents of chapter 3 to 5 form individual studies that have been submitted to peer-reviewed journals. Chapter 3 ("Seasonal precipitation gradients and their impact on fluvial sediment flux in the western Himalaya" by Hendrik Wulf, Bodo Bookhagen, and Dirk Scherler) has been published in Geomorphology [*Wulf et al.*, 2010]; chapter 4 ("Differentiating between rainfall, snow, and glacier contributions to river discharge in western Himalaya using distributed hydrological modeling" by Hendrik Wulf, Bodo Bookhagen, and Dirk Scherler) has been submitted to Water Resources Research; chapter 5 ("Controls on sediment flux in the Sutlej River Valley, western Himalaya" by Hendrik Wulf, Dirk Scherler, and Bodo Bookhagen) is in review.

Chapter 2

Geologic and Climatic setting

The Himalayan orogen is best known for its impressive size, both in lateral extent and in mountain peak elevations. The orogen stretches for about 2,400 km from the Indus River Gorge at Nanga Parbat in the western syntaxis to the Tsango River Gorge at Namche Barwa in the eastern syntaxis (Figure 2.1). Physiographically, the Himalayan arc forms a 150-400 km long transition between the low-elevated ($<$0.5 km) Indo-Gangetic Plain to the south and the high-elevated ($\sim$5 km) Tibetan Plateau to the north [*Fielding et al.*, 1994].

The formation of the Himalaya and the Tibetan Plateau is related to closure of the Tethys oceans between the two great land masses of Laurasia and Gondwana since the Paleozoic [e.g. *Molnar and Tapponnier*, 1975; *Yin and Harrison*, 2000] and the continental collision of India with Eurasia over the past 55–45 Ma [e.g. *Klootwijk et al.*, 1992; *Rowley*, 1996]. The present topography of the high, laterally extensive Tibetan Plateau and surrounding orogens exerts strong influence on atmospheric processes. On a continental scale, the high topography poses a physical obstacle to atmospheric circulations and acts as an elevated heating surface, which intensifies the South Asian monsoon [*Boos and Kuang*, 2010; *Flohn*, 1957; *Hahn and Manabe*, 1975]. At regional scale, orographic barriers influence precipitation patterns and air temperatures, which directly control runoff and surface erosion processes.

2.1 Precipitation

In general, two atmospheric circulation systems dominate precipitation in the Himalaya: the northern-hemisphere westerlies and the South Asian monsoon (Figure 2.2). Both circulation systems are characterized by a pronounced seasonality, resulting in distinct summer and winter precipitation peaks. In fact, the word "monsoon" is derived from "mausim", the Arabic word for season, and therefore tightly

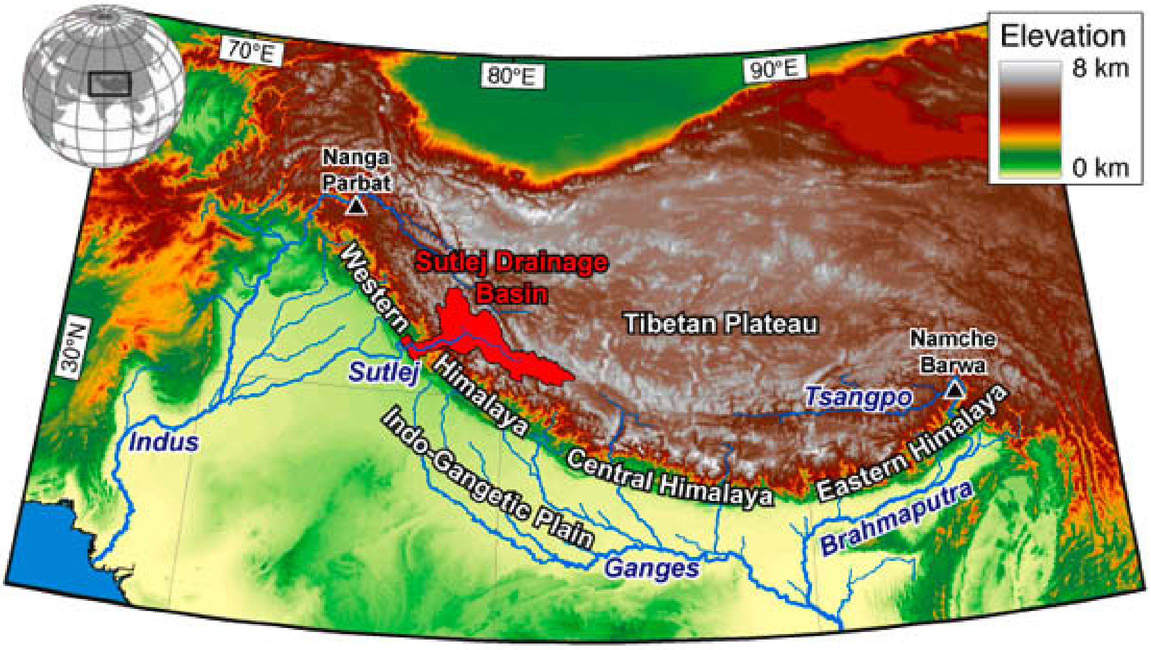

Figure 2.1: Topographic overview of central Asia and the Himalayan major river systems. Elevations and river routing is based on the SRTM30 dataset [*Farr et al.*, 2007]. The Sutlej drainage basin is the main study area of this thesis.

connected to the seasonal reversal of wind directions [*Ramage*, 1971]. Over 300 years ago, *Halley* [1686] suggested that the primary cause of the monsoon was the differential heating between ocean and land. Rapid warming of the Indian subcontinent and the Tibetan Plateau during summer induces a strong pressure gradient towards the relatively cooler Indian Ocean (Figure 2.3) [*Flohn*, 1957; *Hahn and Manabe*, 1975]. Consequently, the Inter-Tropical Convergence Zone migrates far north to the Indian plains and drives persistent landward flow of moisture from the Indian Ocean that underpins the monsoon [*Gadgil*, 2003]. Deep convection in the northern Bay of Bengal and northwestward propagating low-pressure systems characterize the peak of the South Asian summer monsoon season from June to September, and lead to large amounts of precipitation along the southern flank of the Himalaya (Figure 2.2) [*Lang and Barros*, 2002].

Orographically forced monsoonal precipitation in the Himalaya is closely linked to increases in topographic relief and is highest at elevations <4 km [*Bookhagen and Burbank*, 2006; *Putkonen*, 2004; *Seko*, 1987]. The orographic barrier effectively prevents monsoonal moisture to migrate farther north into the Tibetan Plateau and results in a ten-fold south-to-north precipitation gradient [*Bookhagen and Burbank*, 2006; *Putkonen*, 2004]. Whereas a six-fold east-to-west monsoonal rainfall gradient

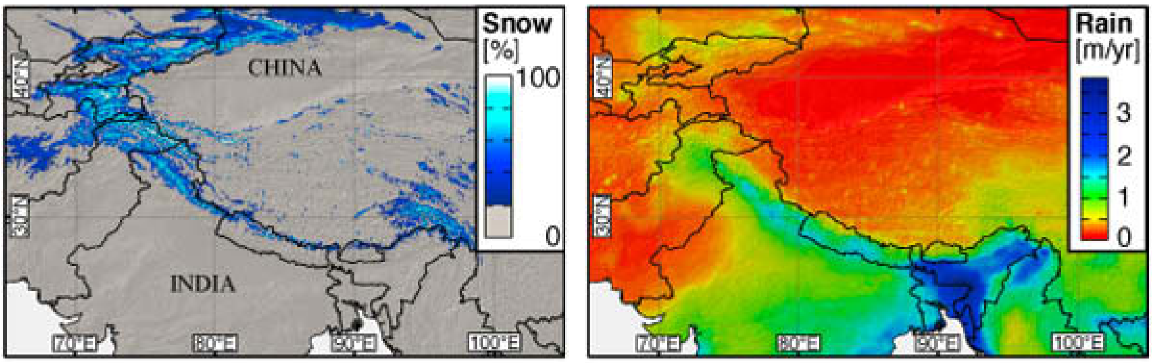

Figure 2.2: Mean annual snow cover and rainfall in central Asia. Snow cover data is derived from the MODIS (MODerate resolution Imaging Spectroradiometer) product MOD10CM [*Hall et al.*, 2002] covering the period March 2000 to February 2011. Rainfall data is derived from the TRMM (Tropical Rainfall Measurement Mission) product 3B43 [*Huffman et al.*, 2007] covering the period January 1998 to December 2010.

exists along the Himalayan foreland, average rainfall within the Himalaya remains nearly constant along strike [*Bookhagen and Burbank*, 2010]. The annual strength of South Asian monsoon varies substantially, which had been liked to the El Nino Southern Oscillation [e.g. *Meehl*, 1994; *Webster et al.*, 1998], tropospheric temperature anomalies over the Tibetan Plateau [e.g. *Fu and Fletcher*, 1985; *Yanai et al.*, 1992], and winter snow cover in the Himalayas [e.g. *Blanford*, 1884; *Kripalani et al.*, 2003]. Significant rainfall variations on small spatial and temporal scales are characteristic and due to the convective nature of the summer monsoon precipitation [*Barros et al.*, 2000; *Bollasina et al.*, 2002; *Craddock et al.*, 2007; *Yasunari*, 1976; *Yasunari and Inoue*, 1978]. Heavy summer rainfall may also occur on the Tibetan Plateau when an upper-level trough over the Pamirs displaces the westerly jet stream far to the south along the Himalayan front [*Weiers*, 1995]. The coincidence of such a upper-level westerly air flow with monsoonal depressions enables moisture to cross the orographic barrier of the Higher Himalaya and reach areas as far north as the Tibetan Plateau and the Karakoram [*Flohn*, 1956; *Weiers*, 1995].

During winter, the atmospheric pressure gradient between the continent and the Indian Ocean reverses and the ITCZ is located south of the equator. Likewise, the westerlies shift southward and split up in two branches, located north and south of the Tibetan Plateau. Along their eastward path westerly troughs influence synoptic-scale low-pressure systems, known as Western Disturbances, which take up moisture over the Mediterranean, Black, and Caspian Seas [*Dimri et al.*, 2004; *Hatwar et al.*, 2005]. From December to March Western Disturbances cause widespread rain- and snowfall (>2 km asl) across the Hindu-Kush, Pamir, Karakorum, and western Himalaya, which

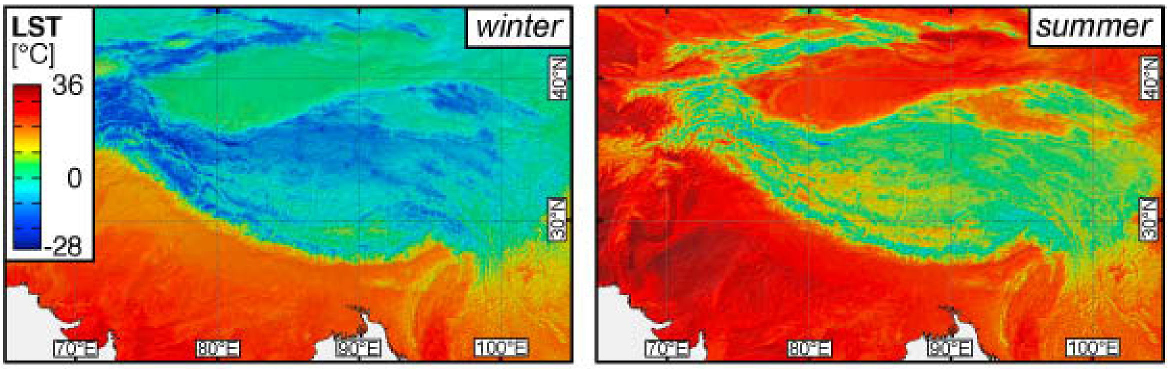

Figure 2.3: Seasonal land surface temperatures (LST) of central Asia during winter (November-April) and summer (May-October). Temperature data is derived from the MODIS product MOD11C3 [*Wan et al.*, 2004] covering the period March 2000 to February 2011.

decrease in magnitude towards the central Himalaya (Figure 2.2) [*Dimri*, 2006; *Lang and Barros*, 2004]. Due to the interactions with mid- to upper-tropospheric westerlies orographic capture occurs predominantly in areas of high topographic relief and is less efficiently blocked by orographic barriers [*Shekhar et al.*, 2010; *Singh and Kumar*, 1997].

2.2 Hydrology

The pronounced seasonality in precipitation is also reflected by the large variability in river discharge and sediment load. The Himalaya is source of major rivers, which contribute to (a) the Indus River System draining large parts of the western Himalaya into the Arabian Sea and (b) the Ganges and Tsangpo/Brahmaputra River Systems draining the eastern, central and parts of the western Himalaya into the Bay of Bengal (Figure 2.1). Along their courses these rivers erode, transport, and deposit large sediment volumes, which build up the vast Indo-Gangetic Plain and the voluminous submarine fans to both sides of the Indian peninsular.

Most rivers draining the Himalaya originate at elevations above 4 km asl and therefore inherit steep river gradients [*Seeber and Gornitz*, 1983]. In these areas of high topographic relief, rivers often form narrow, deep incised bedrock channels, which display abundant evidence of high-energy flood processes and responses [*Baker and Kale*, 1998]. Along the Indus River, for example, *Burbank et al.* [1996] found extremely high incision rates on the order of 2–12 mm/yr over the last 6–67 kyr. This incision is thought to result from quarrying and abrasion of high-magnitude floods [*Hancock et al.*, 1998], which exert a primary control on sediment transport and fluvial erosion [*Froehlich and Starkel*, 1987; *Wohl and Cenderelli*, 1988]. As a result, Himalayan rivers display frequent changes in shape, size, and position, particularly in their alluvial foreland sections [*Kale*, 2002]. For example, several courses of the Kosi River indicate progressive lateral shifting of the river by about 113 km in 228 years [*Gole and Chitale*, 1966; *Wells and Dorr*, 1987].

By the time the rivers cross over to the foreland they deposit large amounts of sediment, as expressed by extensive megafans at the Himalayan front [*Goodbred and Kuehl*, 2003; *Mohindra and Prakash*, 1994]. Studies on the Brahmaputra River inferred that about 40-80% of the total sediment inflow is retained in the floodplains [*Allison et al.*, 1998; *Goswami*, 1985]. Due to the high sediment supply [*Goodbred and Kuehl*, 2000], the Brahmaputra River provides a classic example of a large braided river that is in some places about 10–17 km wide. Large rivers are widely regarded to transport small bedload fractions in comparison to their suspended load [e.g. *Milliman and Meade*, 1983]. The bedload of the Brahmaputra River is estimated to be about 5–15% of the total flux [*Goswami*, 1985]. However, in small mountainous streams bedload can actually exceed suspended load [*Rawat et al.*, 1992]. This partition suggests that bedload constitutes a large fraction of the sediment flux in Himalaya rivers, especially in regions with steep channel gradients and abundant sediment supply. In contrast, the dissolved load contributes typically a minor fraction of about 10% to the total sediment flux, which underlines the physical character of the Himalayan erosion [*Galy and France-Lanord*, 2001]. Generally, suspended sediment load correlates well river discharge [*Milliman and Syvitski*, 1992]. Characteristic for the annual suspended sediment cycle is the peak immediately after the onset of the monsoon and its decrease thereafter [*Kale et al.*, 1986]. This pattern has been linked to the initial removal of readily available material and to increases in protective vegetation cover as the wet season progresses (Figure 2.4)[*Kale et al.*, 1986].

2.3 Sediment Transport and Erosion

The Himalaya is rapidly uplifting, and eroding at high rates. If the hillslopes were in a dynamic equilibrium with the uplift rate, the overall denudation rate would range between 1 and 10 mm/yr [*Heimsath*, 2000]. Such rates are among the highest in the world, along with that of the Southern Alps of New Zealand and the mountains of Taiwan. Assessing the erosional flux from the Himalaya is a primary concern for studies addressing the global carbon cycle[*France-Lanord and Derry*, 1997; *Raymo and Ruddiman*, 1992] and Himalayan tectonic models [*Avouac and Burov*, 1996] as

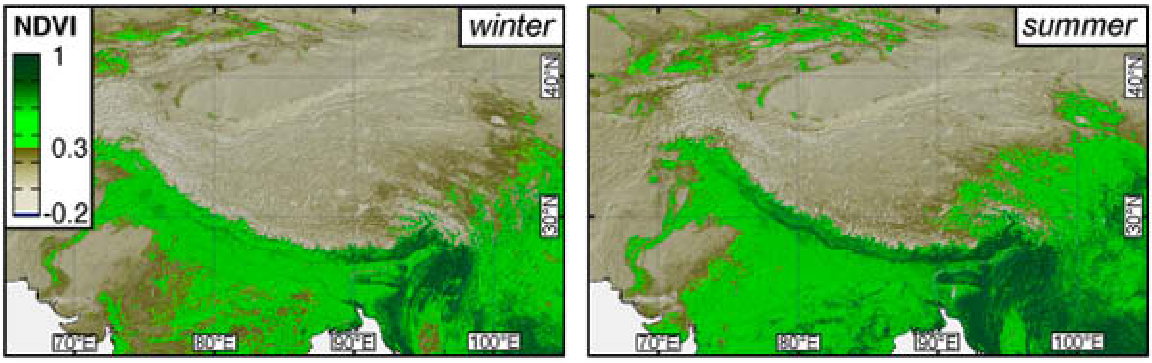

Figure 2.4: Seasonal vegetation cover in central Asia during winter (November-April) and summer (May-October). The Normalized Difference Vegetation Index (NDVI) is derived from the MODIS product MOD13C2 [*Huete et al.*, 2002] covering the period March 2000 to February 2011.

well as hydropower agencies [*Singh et al.*, 2003]. Yet, varies aspects concerning the spatial focus and dominant processes of erosion in Himalaya are controversial and speculative [*Alizai et al.*, 2011; *Chakrapani and Saini*, 2009; *Clift et al.*, 2008; *Galy and France-Lanord*, 2001; *Vance et al.*, 2003]. This is mainly due to difficulties and uncertainties in measuring glacial, periglacial, hillslope and fluvial, erosion rates and their pronounced variations in space and time [*Dortch et al.*, 2011; *Heimsath and McGlynn*, 2008; *Scherler et al.*, 2011b]. Despite these unknowns, several studies using different methodologies suggest a first-order control on erosion by monsoonal rainfall [*Gabet et al.*, 2008; *Garzanti et al.*, 2007; *Thiede et al.*, 2004]. The direct impact of rainfall on slope failure and increases in fluvial sediment flux has been well documented in several studies [*Bookhagen*, 2010; *Burtin et al.*, 2010; *Gabet et al.*, 2004].

Sediment fluxes are of particular interest for hydropower companies, as high sediment accumulation rates deplete reservoir capacities and high sediment concentrations in the water effectively abrade hydropower turbines. Besides the natural processes that contribute to sediment flux (i.e. landslides, floods) there has been a considerable increase in anthropogenic activity (i.e. deforestation, road construction, mining, overgrazing, farmland cultivation), which accentuated the erosion processes in the Himalayan region [*Ives and Messerli*, 1989; *Singh et al.*, 2003]. However, quantitative assessments of human induced erosion are limited [*Barnard et al.*, 2001; *Carson*, 1992], which exemplifies our limited understanding of the erosional processes in the Himalaya. This deficit underscores the need to investigate and quantify the complex interactions between precipitation, hydrology and erosion in diverse topographic and climatic settings.

Chapter 3

Seasonal precipitation gradients and their impact on fluvial sediment flux in the western Himalaya

Abstract

Precipitation in form of rain- and snowfall throughout the Himalaya controls river discharge next to erosional processes and has thus a first-order control on the fluvial sediment flux. Here, we analyze daily precipitation data (1998-2007) of 80 weather stations from the western Himalaya, in order to decipher temporal and spatial moisture gradients. In addition, suspended sediment data allow deciphering the impact of precipitation on the fluvial sediment flux for a 10^3-km^2 catchment (Baspa). We find that weather stations located at the mountain front receive ~80% of annual precipitation during summer (May-Oct), whereas stations in the orogenic interior, i.e., leeward of the orographic barrier, receive ~60% of annual precipitation during winter (Nov-Apr). In both regions 4-6 rainstorm days account for ~40% of the summer budgets, while rainstorm magnitude-frequency relations, derived from 40-year precipitation time-series, indicate a higher storm variability in the interior than in the frontal region. This high variability in maximum annual rainstorm days in the orogenic interior is reflected by a high variability in extreme suspended sediment events in the Baspa Valley, which strongly affect annual erosion yields. The two most prominent 5-day-long erosional events account for 50% of the total 5-year suspended sediment flux and coincide with synoptic-scale monsoonal rainstorms. This emphasizes the erosional impact of the Indian Summer Monsoon as the main driving force for erosion processes in the orogenic interior, despite more precipitation falling during the winter season.

3.1 Introduction

The spatiotemporal distribution of precipitation in mountain belts is highly complex and difficult to map [*Barros and Lettenmaier*, 1994; *Bookhagen and Burbank*, 2006; *Roe*, 2005], yet a key parameter for erosion processes [*Bookhagen et al.*, 2005a; *Reiners et al.*, 2003]. In many studies, the precipitation pattern is invoked as a first-order control on short- and long-term erosion rates [e.g. *Gabet et al.*, 2008; *Thiede et al.*, 2004]. However, the complex coupling of precipitation and erosion is difficult to quantify, as precipitation patterns may vary and affect different erosion processes [*Bookhagen et al.*, 2005a]. Therefore, it is essential to decipher precipitation gradients and their variations, as these partly govern the efficacy of hillslope processes next to fluvial and glacial dynamics [*Gabet et al.*, 2004; *Owen et al.*, 2005]. Unfortunately, reliable high-elevation precipitation data covering several years in the Himalaya remain limited to few locations [*Barros et al.*, 2000; *Winiger et al.*, 2005]. In particular, winter precipitation amounts are largely unknown due to the remoteness and difficult access of high elevations in the orogenic interior [*Putkonen*, 2004].

Here, we analyze the spatiotemporal distribution of precipitation in the vicinity of the Sutlej Valley in the western Himalaya, based on 80 weather stations (Figure 3.1). These stations provide a unique opportunity to investigate climate conditions over several decades and a wide range of elevations (0.4-4.1 km) and topographic settings, i.e., from the wet frontal to the dry interior parts of the orogen. Importantly, the stations cover an area that is influenced by both summer monsoonal and winter westerly precipitation [*Bookhagen and Burbank*, 2010; *Lang and Barros*, 2004]. This condition allows us to compare the impact of the two contrasting atmospheric circulation regimes on erosion processes, which we observe by responses in suspended sediment load in the Baspa River.

Our analysis comprises three objectives: (1) to quantify precipitation (rainfall and snowfall) gradients in space and time, (2) to analyze the magnitude-frequency relations of rainstorms in different orographic settings, and (3) to relate storm events to erosional processes in the orogenic interior by a case study of river and sediment discharge from the Baspa catchment. Based on these analysis we are able to test the hypothesis if monsoonal rainfall dominates the annual precipitation and fluvial sediment flux budget across the western Himalaya.

3.2 Precipitation patterns, orographic barriers, and river discharges in the western Himalaya

Precipitation in the western Himalaya is controlled by two atmospheric circulation systems [*Gadgil*, 2003; *Lang and Barros*, 2004]. First, the Indian Summer Monsoon draws moisture from the Bay of Bengal in the southeast and lasts from June to September. Summer monsoon rainfall amounts decrease from ∼1.5 m at the mountain front to ∼0.1 m north of the orographic barrier. Rainfall magnitudes vary considerably within short distances as a result of convective, localized monsoonal storms [*Barros et al.*, 2006]. Second, the northern-hemisphere westerlies supply moisture during December to March, derived from the Mediterranean, Black, and Caspian Sea. This winter westerly precipitation is coupled to mid/upper tropospheric, synoptic-scale low-pressure systems, known as Western Disturbances, and is thought to be of stratiform type, i.e., less intense, more prolonged, and encompassing a larger area, than the commonly convective monsoonal rainfall [*Dimri*, 2006; *Putkonen*, 2004].

The Himalayan mountain chain forms a pronounced orographic barrier, which separates the southern windward, wet frontal regions from the northern leeward, summer-dry interior parts. This barrier forces moist monsoonal air masses to ascent, which enhances condensation and cloud formation, and ultimately controls the triggering, duration, and intensity of precipitation events [*Bookhagen et al.*, 2005a]. Thus, it typically prevents the migration of moist monsoonal air masses leeward of the orographic barrier and creates an orographic rain shadow in semi-arid to arid orogenic interior. In our study area the main orographic barrier ranges between 4.0 and 6.6 km in elevation and it coincides with drainage divides of large river systems draining frontal and interior parts of the orogen (Figure 3.1). In contrast to the monsoonal air masses, winter westerly moisture is transported at higher tropospheric levels [*Weiers*, 1995]. Thus, the winter westerlies predominantly undergo orographic capture at higher elevations in the orogenic interior, where intense snowfall occurs in areas of high elevation and pronounced relief [*Lang and Barros*, 2004].

In non-glacierized catchments at the orogenic front, river discharge is closely coupled to summer rainfall, which dominates annual precipitation in these areas [*Craddock et al.*, 2007; *Putkonen*, 2004]. In contrast, within the orogenic interior snow and glacial melt waters may contribute more than 50% to the annual runoff [*Bookhagen and Burbank*, 2010; *Immerzeel et al.*, 2009; *Singh and Jain*, 2002]. Thus, in both compartments of the orogen, peak river discharge occurs in summer, although the

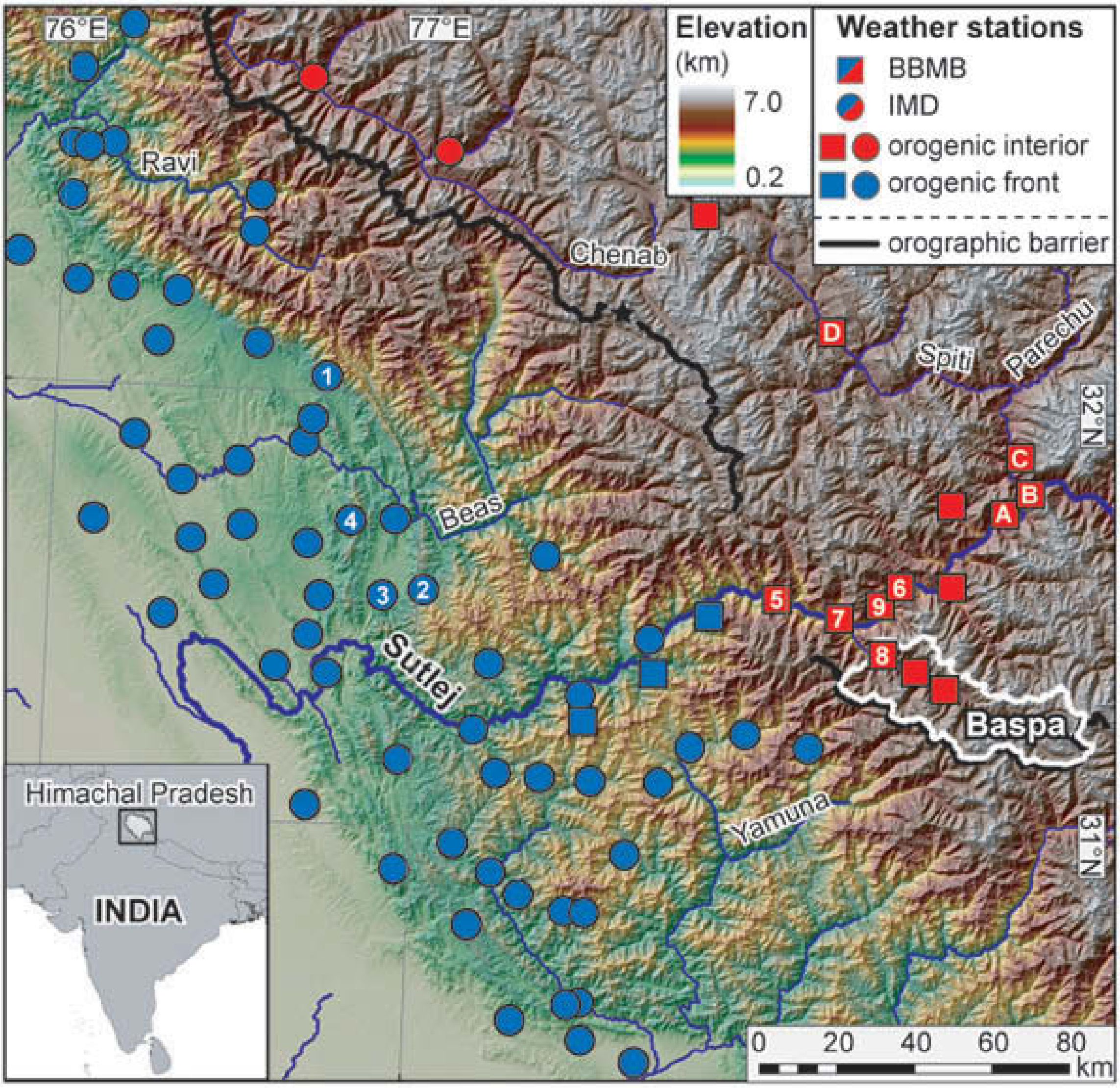

Figure 3.1: Topographic overview of the study area and weather stations. Shaded-relief and elevation map of northern India (Himachal Pradesh in the western Himalaya). Weather stations represented by black symbols are situated in the lee of the main orographic barrier (orogenic interior), whereas white symbols indicate stations located to the south of the barrier (orogenic front). Circle- and square-shaped symbols indicate the Indian Meteorological Department (IMD) and the Bhakra Beas Management Board (BBMB), respectively, as operators of these stations. Letters (A-D) and numbers (1-9) refer to weather stations analyzed in Figure 3.3 and Figure 3.5, respectively. Star denotes the snow water equivalent values reported by Wagnon et al. (2007). We point out that the Sutlej River slices through the main orographic barrier and forms a potential conduit for transport of moist air into the orogenic interior. However, the mean summer rainfall recorded by weather stations in this corridor (Figure 3.1, label 5, 6, 7 and 9) is typically low (0.4-0.2 m), as substantial amounts of the monsoonal moisture are drained at previous orographic barriers. Thus we consider these stations as part of the orogenic interior.

precipitation timing and spatial gradient of the main moisture bearing circulation regimes differ fundamentally.

3.3 Data Set and Methods

We processed daily precipitation data spanning ten years (1998-2007) from 80 meteorological stations located within the state of Himachal Pradesh in NW India (Figure 3.1). Snowfall is reported in snow water equivalent (SWE), which has been measured by melting daily snow accumulations. This data set comprises 63 weather stations from the Indian Meteorological Department (IMD) and 17 high-elevation stations from the Bhakra Beas Management Board (BBMB). At nine stations (Figure 3.1: labels 1-9) longer time-series (1961-2007) were available, which we analyzed for summer-rainstorm magnitude-frequency relations. We checked the precipitation data for plausibility according to quality-control measures introduced by [*Einfalt and Michaelides*, 2008] and excluded unreliable values from subsequent analyses. Further details on the data location and quality are given in Table A.1. The probability density function (PDF) of daily monsoonal rainfall events can be characterized by a gamma distribution [*May*, 2004]. We used the corresponding cumulative density function (CDF) to assess the fraction of total summer rainfall delivered by heavy rainstorms. The magnitude-frequency analysis of maximum summer rainfall days plots the ranked daily rainstorm amounts against their recurrence intervals, which represent the time span between two successive rainfall days of that particular magnitude at that weather station. *Gumbel* [1958] defined the recurrence interval as:

$$ri = \frac{n+1}{r} \tag{3.1}$$

where ri is the recurrence interval, n is the length of the time-series and r is the ranking number of the event.

We consider the precipitation during the summer (May-October) as predominantly monsoonal in origin and precipitation during the winter (November-April) as mainly derived from winter westerlies. In the spatial domain we distinguish between the orogenic interior and front of the mountain range. The orogenic interior is located entirely in the lee (∼northeast) of the main orographic barrier and is characterized by high elevations at the river level, i.e., >2 km asl, a high degree of glaciation, low summer precipitation (<0.4 m), and sparse to no vegetation. The orogenic front represents areas that are located southwest of the main orographic barrier and are characterized by high summer rainfall (>0.4 m), various dense vegetation types, and a low degree of glaciation.

To decipher the impact of precipitation on fluvial sediment flux within the orogenic interior, we analyzed daily river discharge and suspended sediment concentration (SSC) from 2004 to 2008 of the Baspa River, the second largest tributary of the Sutlej River. These data were provided by the Baspa-II hydropower station of JayPee Group and sampled at the location of Sangla (Figure 3.1: label 8). The SSC values represent the daily average of four filtered and weighted water samples. River discharge is measured once daily based on a stage-discharge rating curve, which is recalculated each year due to scour-and-fill of the channel bed. We assume a 20% uncertainty in these data which arises from (1) changes of the river cross-section caused by scour and fill during high discharges and (2) near-shoreline sampling of the SSC data that underestimates the average SSC. To estimate bedload contributions, we analyzed sedimentation rates in the sedimentation reservoir before the water enters the hydropower tunnel. Based on its large initial storage capacity (1.38×10^{-3} km^3), we assume that the majority of the Baspa bedload flux is captured in the reservoir over a ~500 m long and 300 m wide area, about 2 km downstream of Sangla. The sedimentation rates were derived from three depth soundings of the hydropower reservoir in January 2003, October 2004, and April 2007. Flushing of the reservoir took place during a flood from the 5th to 10th July, which excavated approximately 80% of the reservoir fill [D. P. Goel, Senior General Manager of the Baspa-II hydropower station, personal communication, September 11, 2008]. Additional daily SSC measurements downstream of the reservoir allow us to account for accumulation of suspended sediment in the reservoir due to reduced flow velocities. The confidence interval for mean values throughout this study is $\pm 1\sigma$.

3.4 Results

3.4.1 Precipitation gradients

At the orogenic front, summer precipitation accounts, on average, for 79 ± 6% (0.98 ± 0.18 m/summer) of the mean annual precipitation (1.23 m/yr), while winter precipitation in these low-elevation areas is only 21 ± 6% (0.25 ± 0.07 m/winter). In contrast, the orogenic interior receives on average 42 ± 14% (0.27 ± 0.13 m/summer) of its mean annual precipitation (0.62 m/yr) during summer and 58 ± 14% (0.35 ± 0.11 m/winter) during winter (Table 3.1). These pronounced regional distinctions in precipitation during both seasons are illustrated in more detail by the distribution of

Table 3.1: Ten-year average precipitation and intense precipitation days in the western Himalaya (Himachal Pradesh, India). Only weather stations with a minimum of four continuous years were included in this analysis (orogenic front n = 41, interior n = 10). We defined storm thresholds for each station by the respective daily precipitation amount of the uppermost 10% of the cumulative distribution function of precipitation (see Figure 3.4). Storm days, magnitudes, and percentages represent the seasonal average number of storms exceeding the threshold, their cumulative precipitation, and the percent of average storm magnitudes on the average precipitation magnitude, respectively. The entire cumulative distribution function of summer rainfall and its respective proportion of total summer precipitation is shown in Figure 3.4. The given standard deviation (±1σ) indicates the significant interseasonal variations in precipitation, which are most pronounced in the orogenic interior.

		precipitation		**10% tail of the precipitation probability distribution (storms)**			
		magnitude (mm/season)	days (#)	storm threshold (mm/day)	days (#)	magnitudes (mm/days)	percentages (%)
orog. front	summer	977 ± 182	53 ± 6	44 ± 6	6.0 ± 0.6	393 ± 64	40 ± 2
	winter	252 ± 71	20 ± 5	30 ± 6	2.6 ± 0.5	97 ± 27	39 ± 3
orog. interior	summer	268 ± 128	39 ± 7	16 ± 7	4.6 ± 0.7	121 ± 77	44 ± 7
	winter	354 ± 106	31 ± 6	27 ± 5	3.8 ± 0.8	140 ± 44	40 ± 4

mean monthly precipitation (Figure 3.2). The most pronounced precipitation gradient occurs during summer, when monsoonal rainfall decreases by more than one order of magnitude within 100 km. Mean summer rainfall magnitudes of up to 2.5 m at high relief sites at the orogenic front decrease sharply to ∼0.3 m leeward of the main orographic barrier and reach values of ∼0.1 m in the Spiti valley, 30 km northeast of the orographic barrier (Figure 3.1). This negative orogenward precipitation gradient is reversed during winter, when precipitation increases gradually from ∼0.2 m over lower elevations (∼0.5 km asl) at the orogenic front to ∼0.4 m over high elevations (∼3 km) in the orogenic interior. As a result, SWE as well as the winter fraction of the annual precipitation increases linearly with elevation (Figure 3.3). Weather stations in valley locations within the orogenic interior (Figure 3.1: labels A-C), which are shielded by high relief, are less representative, as these are characterized by low mean annual SWE (<0.1 m) irrespective of their elevation (Figure 3.3).

3.4.2 Precipitation intensity and variability

Frequency analyses of the ten-year precipitation data show that during both seasons and in both regions the most intense 10% and 20% of the probability distribution of all precipitation days account for approximately 40% and 60% of the total seasonal precipitation, respectively (Figure 3.4). For example, ∼40% of the summer rainfall is

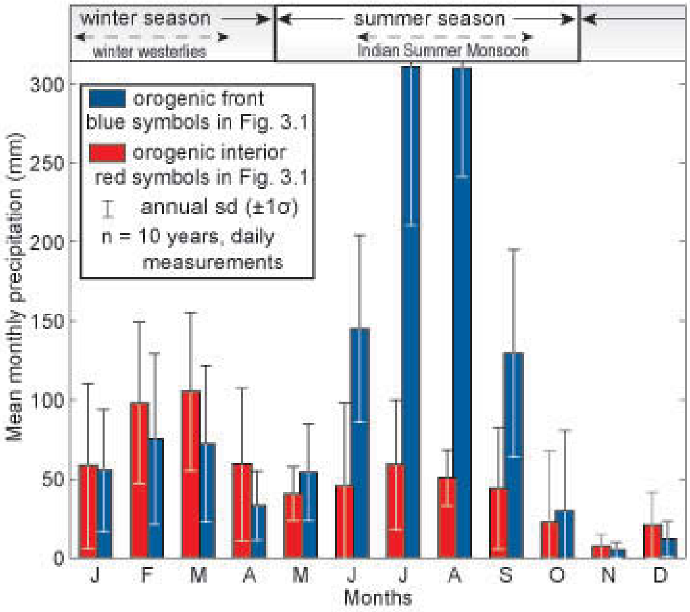

Figure 3.2: Average monthly precipitation from 1998 to 2007 of weather stations in the orogenic interior and front. Precipitation during the winter season (November-April) derives predominantly from the winter westerlies, whereas most summer precipitation (May-October) derives from the Indian Summer Monsoon. The error bars represent ±1σ.

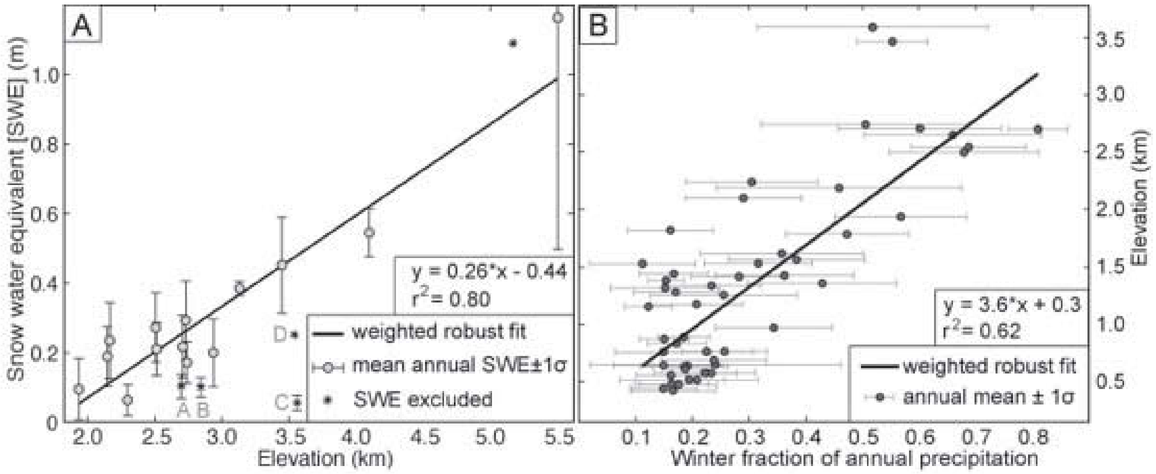

Figure 3.3: (A) Relation of snow water equivalent (SWE) and elevation. Annually measured minimum SWE values above 5 km are taken from *Wagnon et al.* [2007]. Due to high annual variations we excluded data from two locations with less than three continuous years ("D"), as well as three orographically shielded valley stations ("A-C") at the Sutlej-Spiti confluence which are characterized by unrepresentative low annual precipitation. These three stations ("A-C") affect the regression by a reduced coefficient of determination ($r^2 = 0.65$) with the following linear model: $y = 0.24 \cdot x - 0.42$. **(B) Fraction of winter precipitation on annual precipitation vs. elevation.** We excluded data from stations with less than four continuous years to account for high annual variations. The robust linear fit implies an increasing dominance of winter precipitation in high elevations. In both figures the robust correlation was weighted by the number of measurement years and error bars reflect ±1σ.

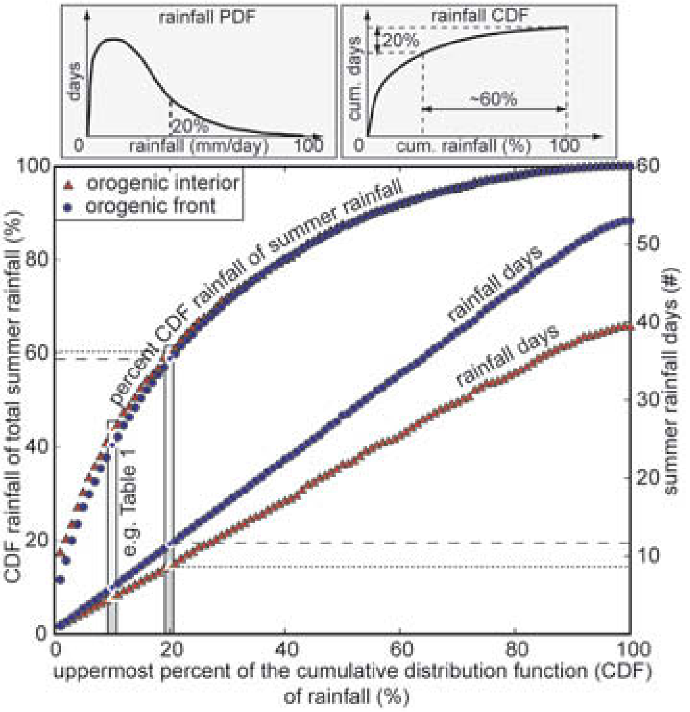

Figure 3.4: Percentage of heaviest rainfall and its respective fraction of the summer rainfall budget and rainfall days, which account for these fractions in the orogenic interior and the orogenic front. Two sketches on the gamma probability density function (PDF) of summer rainfall and the corresponding cumulative distribution function (CDF) illustrate the derivation of the x-and-y-variables using the example of the 20% heaviest rainfall days, which account for approximately 60% of the total summer precipitation. In both regions, only a few rainfall days account for large proportions of the summer precipitation budget. Precise numbers for the case of the 10% heaviest precipitation days are given in Table 3.1.

derived from only 4-6 high-magnitude rainfall days throughout the whole study area (Table 3.1). Total precipitation during both seasons, in particular within the orogenic interior, is characterized by large interseasonal variations. To verify this regional contrast in summer rainfall variations we analyzed a 40-year precipitation time series from nine stations in the orogenic interior and at the front (Figure 3.1: labels 1-9). In these data we observe an increase in interseasonal summer rainstorm variability with elevation. The magnitude-frequency distribution of maximum summer rainfall days reveals that the rate of increase in storm magnitude with respect to return time is higher in the orogenic interior than at the orogenic front (Figure 3.5). As a result, the magnitude of a 2-year rainstorm is 3.8 times smaller in the interior region than compared to the frontal region, whereas the 20-year rainstorm is only 1.9 times smaller. Furthermore, 10-year peak rainstorms in the orogenic interior are comparable in strength to annual peak rainstorms at the orogenic front.

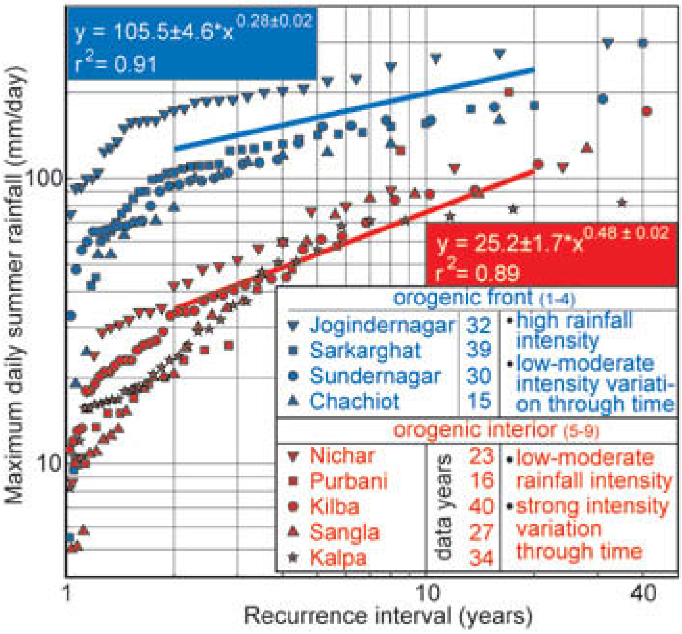

Figure 3.5: Rainfall magnitude frequency at the orogenic front vs. the orogenic interior. Maximum daily summer precipitation at the orogenic front (open symbols, 1-4) and at the orogenic interior (filled symbols, 5-9), see Figure 3.1 for locations. Data cover the period 1961-2007; years with missing data were excluded. The trend lines represent a power-law fit to all data within a recurrence interval of 2 to 20 years in both spatial regions. The coefficient of determination (r^2) represents the mean fit of individual station correlations within each region. The orogenic interior shows a steeper increase in recurrence interval with respect to rainfall rate that indicates a higher intensity variation of rainstorms as compared to the orogenic front.

3.4.3 Case study:

The Baspa River is the second largest tributary of the Sutlej (Figure 3.1). Its 1102-km^2 catchment is situated in the orogenic interior and is glacierized with 20%. Based on the Shuttle Radar Topographic Mission (SRTM) Version 2 topographic data with a 90-m grid-cell size, the hillslopes of the Baspa valley are on average 27° steep and basin elevations range from 1.8 to 6.4 km. Three valley-weather stations in Sangla (2.7 km asl), Rakchham (3.1 km), and Chhitkul (3.4 km) indicate 0.31 ± 0.06 m mean summer precipitation and 0.37 ± 0.13 m mean winter precipitation. Throughout the year, precipitation increases with elevation at a rate of ~0.12 m/km. River discharge and suspended sediment concentrations start to rise in April/May due to snow and glacier melt and peak in July/August due to additional monsoonal rainfall. Low-flow conditions are regained by mid to late October. Due to low river transport capacities and suspended sediment concentrations during winter, more than 99% of the fluvial sediment transport takes place during summer (Table 3.2).

Table 3.2: Annual suspended sediment load, runoff, and erosion rates of the Baspa catchment from 2004 to 2008. Suspended sediment load during summer accounts for >99% of the annual budget. Peak SSC events, as shown in Figure 3.7, account for large fractions of the annual suspended sediment load budget and high erosion rates. Annual runoff reflects variations in annual precipitation and temperatures. Annual erosion rates, which account for suspended sediment load and bedload, vary significantly due to varying magnitudes of peak SSC events.

year	suspended sediment load (SSL)					runoff	modern erosion rate		
	annual	summer	summer/ annual	peak SSL/ annual	peak SSL erosion	annual	SSL	bedload (2:1 ratio)	combined load
	10^5 t	10^5 t	%	%	mm/events	m/yr	mm/a	mm/a	mm/a
2004	2.06	2.05	99.6	0.0	0.00	0.83	0.15	0.07	0.22
2005	15.27	15.24	99.8	63.0	0.67	1.37	1.10	0.55	1.65
2006	5.12	5.07	99.0	35.6	0.13	1.24	0.37	0.18	0.55
2007	19.60	19.56	99.8	81.3	1.15	1.07	1.42	0.71	2.12
2008	6.22	6.21	99.7	48.2	0.21	0.92	0.45	0.22	0.67
mean	9.65	9.62	99.6	45.6	0.43	1.09	0.70	0.35	1.05
std	7.43	7.42	0.3	30.7	0.47	0.22	0.54	0.27	0.80

Daily SSC correlate by a power law with daily river discharge (Q) as described by the sediment rating curve [*Campbell and Bauder*, 1940]: SSC (g l^{-1}) $= 3.8 \times 10^{-4}$ (g l^{-1}s m^{-3}) $\times$ Q$^{1.6}$ (m^3 s^{-1}), $r^2 = 0.77$ (Figure 3.6).

This correlation suggests increased reworking of sediment storage in the riverbed as the river discharge increases. A clockwise hysteresis loop in the suspended sediment flux is weakly pronounced and indicates slightly more suspended sediment transport on the rising limb of the hydrograph (May, June) than on the falling limb (September, October) for a given discharge. Within the five-year SSC record we identified eight peak events with anomalously high suspended sediment concentrations (SSC > 2 g/l), which are characterized by large residuals from the sediment rating curve. These eight peak SSC events lasted for 1-5 days and occurred almost exclusively during June to August (Figure 3.7). In total, they account for 62% (3×10^6 t) of the total five-year suspended sediment load. The two most prominent of these eight events (starting 5th July 2005 and 11th August 2007) coincided with several-day-long and extensive monsoonal rainstorms and account for 50% (2.4×10^6 t) of the total five-year suspended sediment load. Maximum daily rainfall in the Baspa Valley during these two events (1st and 7th event in Figure 3.7) amounted to 54 mm and 35 mm, respectively. Based on the magnitude-frequency relation of maximum summer rainstorms in the orogenic interior, such daily rainstorms re-occur at intervals of three to five years (Figure 3.5). Additional analyses of all 80 weather stations in Himachal Pradesh reveal that these two storms were characterized by a large spatial extent (>100 km), lasted 2-3 days in

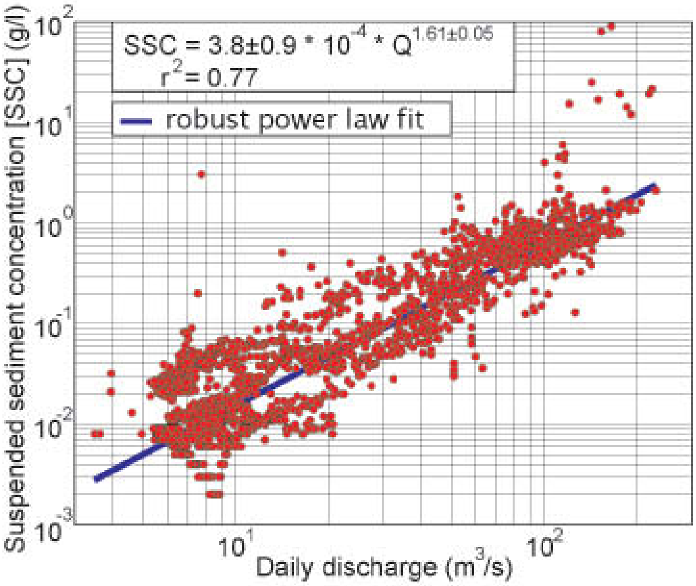

Figure 3.6: Sediment rating curve of the Baspa River showing suspended sediment concentration (SSC) as a function of daily river discharge (Q). Events with anomalously high SSC values (>2 g/l) are analyzed further and shown in Figure 3.7. SSC variance is typically on the order of two magnitudes for a given discharge level due to annually varying sediment availability, seasonal hysteresis effects, and sudden sediment delivery events caused by landslides, snow avalanches or glacial sediment discharges. Note that the rating curve underestimates sediment flux as it does not capture the peak SSC events adequately. The power-law fit is based on the least square method.

most records, and migrated form the orogenic front across the main orographic barrier into the orogenic interior. The 10-year record indicates that 17 such rainstorms occurred at the orogenic front, but only ten reached the orogenic interior.

An example of the hillslope processes that took place during the first event, starting on 5th July 2005, is a 2.5×10^5-m^3 landslide, which occurred 4 km downstream of Sangla (Figure 3.1: label 8) and is therefore not included in our SSC data. On 5th July 2005 the rainstorm magnitude in Sangla culminated with 41 mm/day and triggered slope failure along a 0.5 km reach (Figure 3.8). The landslide eroded parts of a fan, which was covered by sparse vegetation and subject to previous slope failures as indicated by its morphology. The only road to Sangla and into upstream villages crossed this landslide area and was subsequently cut off. Access to the Baspa Valley was inhibited for three months *Sharma* [2006].

We estimate modern erosion rates in the Baspa Valley by accounting for suspended sediment load (SSL) and bedload flux. The average erosion rate derived from suspended sediment load, ESSL, is calculated according to

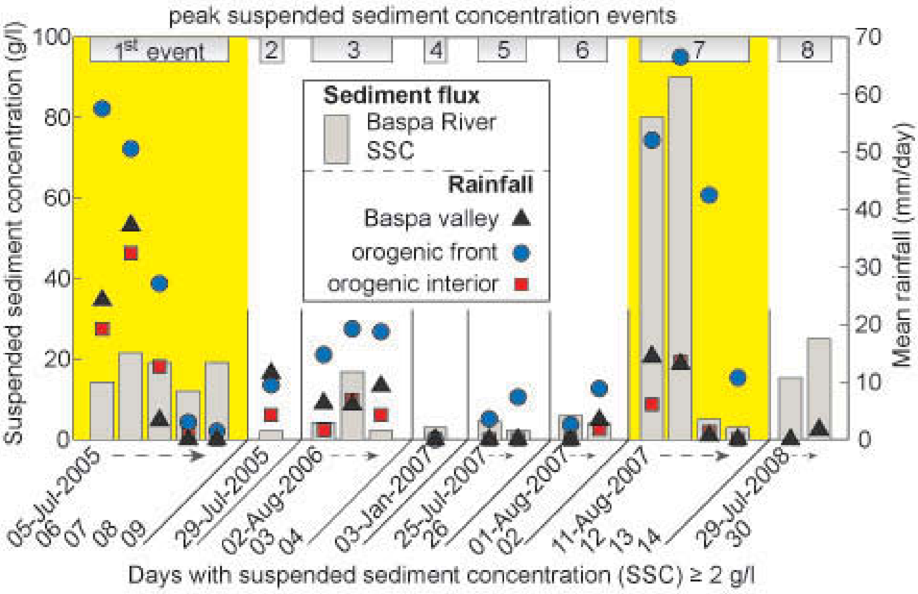

Figure 3.7: Comparison of peak sediment flux events and rainfall. Days with suspended sediment concentration (SSC) ≥ 2 g/l in the Baspa River. Daily rainfall represents the mean of three stations in the Baspa Valley, 17 in the orogenic interior, and 63 at the orogenic front. Note the coincidence of heavy precipitation, lasting for 2-3 days, and the two most significant SSC events (1st and 7th).

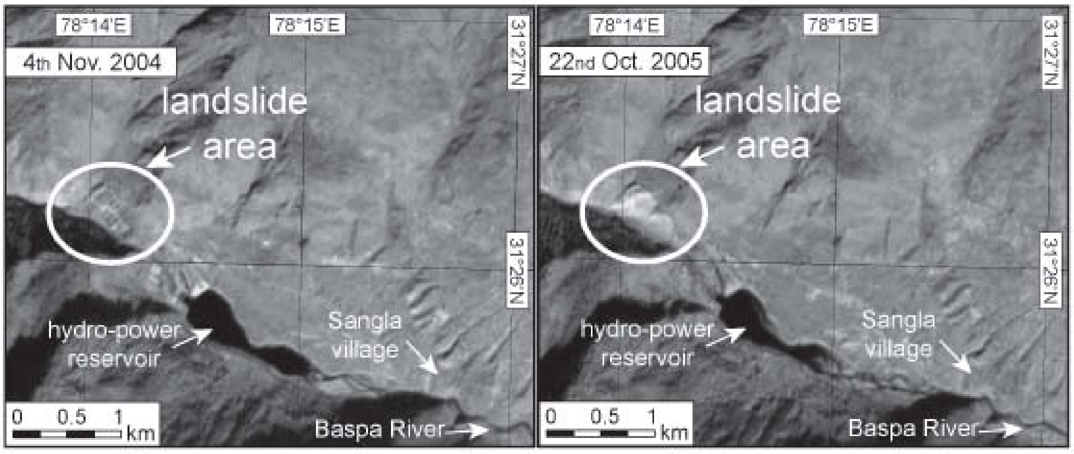

Figure 3.8: Landslide area in the Baspa Valley 4 km downstream of Sangla shown by Advanced Spaceborne Thermal Emission Reflection Radiometer (ASTER) images before and after the event (5th July 2005).

Table 3.3: Estimation of the Baspa River bedload. The reservoir sedimentation volumes were derived from depth soundings. We converted these volumes into mass by assuming a reservoir fill bulk density of 2 t/m^3. On average, 14% of suspended sediment load influx during summer accumulates in the reservoir due to reduced flow velocities. The suspended sediment-to-bedload ratio differs considerably, which is in large part due to peak SSC events that occurred during the second period. We consider both SSL-bedload-ratios as end members of a possible range. It is likely that the SSL during the first period would further increase, due to increased river discharge following pronounced snowfall during the winter 2002/03 (0.5 m SWE in Chhitkul at 3.4 km asl). During the second period, the bedload component is underestimated, as bedload was not captured during the flood in July 2005.

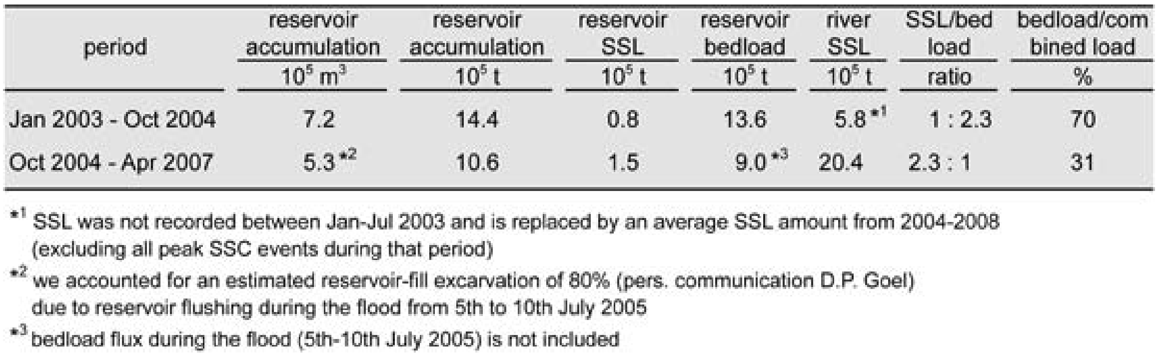

period	reservoir accumulation 10^5 m^3	reservoir accumulation 10^5 t	reservoir SSL 10^5 t	reservoir bedload 10^5 t	river SSL 10^5 t	SSL/bed load ratio	bedload/combined load %
Jan 2003 - Oct 2004	7.2	14.4	0.8	13.6	5.8 *1	1 : 2.3	70
Oct 2004 - Apr 2007	5.3 *2	10.6	1.5	9.0 *3	20.4	2.3 : 1	31

*1 SSL was not recorded between Jan-Jul 2003 and is replaced by an average SSL amount from 2004-2008 (excluding all peak SSC events during that period)

*2 we accounted for an estimated reservoir-fill excarvation of 80% (pers. communication D.P. Goel) due to reservoir flushing during the flood from 5th to 10th July 2005

*3 bedload flux during the flood (5th-10th July 2005) is not included

$$E_{SSL} = \sum_i \frac{SSC_i \cdot Q_i}{\rho \cdot A} \tag{3.2}$$

where SSC_i is the mean daily suspended sediment concentration, Q_i is the daily Baspa river discharge, ρ is the density of the suspended sediment (1.4 t/m^3), and A is the drainage area (989 km^2) of the Sangla subcatchment. We estimate bedload contributions based on reservoir sedimentation rates of the hydropower plant within the Baspa valley (Table 3.3). The analyzed two periods (1st period: Jan 2003 to Oct 2004; 2nd period: Oct 2004 to Apr 2007) exhibit large differences, which are mostly related to the occurrence of high SSC events during the second period. For example, during the flood in June 2005 the high SSC increased the daily SSL by a factor of 19.3, whereas river discharge, which controls the quantity of bedload transport, increased only by a factor of 1.3. Thus, high SSC events increase the SSL several times more than bedload, which consequently increases the SSL-bedload-ratio. Since high SSC events occurred frequently from 2005 onwards, we assume that the approximate 2:1 SSL-bedload-ratio of the second period is a reliable estimate for the entire five-year SSL time-series (2004-2008). The average modern erosion rate of the Baspa River based on SSL and bedload from 2004 to 2008 is 1.05 ± 0.8 m/yr (Table 3.2). The pronounced variability relates in large part to the occurrence of peak SSC events, which vary strongly in magnitude. For example, the two most prominent peak events (1^{st} and 7^{th} event in Figure 3.7) account for 61% and 77% of the high annual SSL in 2005 and 2007, which translate into 0.67 mm/5days and 1.09 mm/4days erosion rates, respectively (Table 3.2).

3.5 Discussion

Our analysis shows that the spatially and temporally varying moisture fluxes have very different effects on the hydrologic and erosional regime of the Baspa Valley. In the high-elevation areas of the orogenic interior, winter snowfall is higher than summer rainfall and thus leads to significant glacial accumulation. Studies by *Bookhagen and Burbank* [2010] and *Singh and Jain* [2002] show that snow and ice melt during summer contribute significantly (>50 %) to river discharge in the Sutlej Valley but high-magnitude/low-frequency monsoonal rainstorms dominate our historic short-term records of fluvial sediment flux. Similar observations on extreme events have been made in other semi-arid to arid mountainous environments [*Coppus and Imeson*, 2002; *Wolman and Miller*, 1960]. The rare occurrence of these events in the orogenic interior implies that reliable estimates of mean erosion rates derived from SSC data need to be based on longer observation periods as compared to the orogenic front [cf. *Gabet et al.*, 2008].

In frontal regions, intense monsoonal rainfall accounts for vigorous fluvial incision and mass wasting on an annual basis [e.g. *Burtin et al.*, 2010; *Craddock et al.*, 2007; *Gabet et al.*, 2004]. The large spatial extent (>100 km) and duration (>2 days) of the two intense rainstorm events that triggered vast sediment discharges in the Baspa Valley is characteristic for synoptic-scale rainstorms, which intrude far into the interior of the orogen and are therefore different from typically more localized convective rainfall events [*Barros et al.*, 2004]. We argue that such extensive rainstorms are able to mobilize large amounts of sediment material in the orogenic interior, which is characterized by steep vegetation-free hillslopes and numerous bare alluvial fans that provide readily erodible sediment sources. Indeed, a study by *Bookhagen et al.* [2005a] shows that during an abnormally strong rainfall year in 2002, erosion on non-vegetated hillslopes mostly occurred through debris flows.

We found that maximum annual rainstorm events in the orogenic interior exhibit strong variations in rainfall intensity (Figure 3.5). This implies that peak erosional events, which are linked to heavy rainstorm events, also undergo large variations, as reflected by the large deviations in annual suspended sediment flux (Table 3.2).

Precipitation data from the central Himalaya, suggest similar differences in the variability of monsoonal storm intensity between the orogenic interior and the orogenic front [*Craddock et al.*, 2007]. This regional contrast in monsoonal storm variability between frontal and interior regions throughout the Himalaya is presumably related to the main orographic barrier. In a similar setting further west in the Karakoram, rare occurrences of summer monsoon rainfall far behind the main orographic barrier have been associated by *Weiers* [1995] to the coincidence of monsoonal depressions with southerly air flows at the 500 hPa level. This synoptic configuration during summer is given when troughs in the upper tropospheric westerly jet are located above the Hindu Kush-Pamir region and divert the westerlies southwards [*Weiers*, 1995]. However, the interaction of westerly airflow and monsoonal depressions, which leads to large annual variations in rainstorm magnitudes, is restricted to the western end of the Himalaya.

Slope failure induced by significant monsoonal rainstorms is a common phenomenon in the orogenic interior, as documented by *Bookhagen et al.* [2005a] and witnessed by the authors in the years 2002, 2005, 2007 and 2009. Based on these observations, we deduce that heavy monsoonal rainfalls triggered two of the eight peak SSC events and infer that these were linked with hillslope processes as shown in Figure 3.8. During the remaining six peak SSC events the recorded daily rainfall amounts in the Baspa Valley were moderate to low (Figure 3.7) and no earthquakes occurred in the region. It is likely that rainfall amounts in the valley locations underestimate the rainfall at higher elevations and that convective monsoonal rainstorms vary considerable in intensity within short distances [*Barros et al.*, 2006]. Antecedent moisture may also increase the regolith field capacity such that moderate rainfall amounts produce positive pore pressures, which reduce slope stabilities [*Gabet et al.*, 2004]. Alternatively, transiently stored sediments in the riverbed could have been remobilized due to increased discharge by snow and glacial melt. Most notably here is the effect of rain-on-snow, which results in rapidly rising river discharges that occasionally reach flood levels [*McCabe et al.*, 2007; *Singh et al.*, 1997]. In addition, *Gabet et al.* [2008] also found a dependence of high sediment flux on high temperatures during the absence of rainfall in July and August and suggests a subglacial origin as a potential sediment source.

Our modern erosion rate estimates, based on SSL and bedload data, reflect the erosion of fluvial sediment storage and possibly include sediments from hillslope erosion, which is suggested by the rapid increase in SSC levels of more than one magnitude during the two major rainstorm events. This modern erosion rate does not necessarily reflect the catchment-wide erosion, as the rivers that aggrade or incise under- or over-represent the amount of eroded material in the catchment. Furthermore, we acknowledge that our estimated bedload rates, which were derived from reservoir sedimentation rates, contain interpolated SSL data and missing bedload flux due to the reservoir flushing during the flood in July 2005. However, the bedload component of the sedimentary flux in alpine rivers is typically difficult to measure [*Leopold and Emmett*, 1976]. Given the scarce bedload data from the Himalaya, we rely on these locally derived estimates. The applied 2:1 SSL-bedload-ratio is also consistent with mapped lacustrine (SSL) and deltaic (bedload) deposits from a mid-Holocene landslide-dammed lake in the upper Marsyandi catchment, a similar environment in the central Himalaya [*Pratt-Sitaula et al.*, 2007]. Nevertheless, this ratio might underestimate the real bedload, as *Galy and France-Lanord* [2001] suggest that bedload fluxes in the Himalayas may be of the same magnitude as suspended sediment fluxes. If this were the case for the Baspa Valley, the modern erosion rate increases by 33% to ∼1.4 mm/yr.

Gabet et al. [2008] analyzed modern mean erosion rates from individual catchments in the Marsyandi Valley in the central Himalaya, which range from 0.1 ± 0.1 mm/yr to 2.0 ± 0.6 mm/yr, and found an increase in modern erosion rates with increasing average monsoonal rainfall amounts. Tributary catchments from the Marsyandi region, which are comparable to the Baspa Valley, show lower mean erosion rates (0.5 ± 0.3 mm/yr), as those catchments are characterized by less annual runoff and moderate magnitudes of peak SSC events [*Gabet et al.*, 2008]. To evaluate the impact of monsoonal precipitation on erosion rates within a 10^4-year time-scale, we compare our modern estimate (1.05 ± 0.8 mm/yr) with Holocene erosion yields in the context of varying monsoonal strength. Volumetric analyzes of lake sediments behind an early to mid-Holocene landslide deposit in the Baspa Valley indicate upstream erosion yields of 4.3 ± 0.4 mm/yr, about four times higher than present-day average yields [*Bookhagen et al.*, 2005b]. This period was characterized by intensified monsoon rainfalls and highlights the susceptibility of semi-arid regions behind the orographic barrier to millennial-scale monsoonal strength variations.

3.6 Conclusion

Precipitation data from 80 weather stations from the western Himalaya reveal that summer precipitation from May to October accounts for ∼80% of the mean annual precipitation at the orogenic front, whereas winter precipitation from November to April accounts for ∼60% of the annual budget in the orogenic interior. Although 40% of summer precipitation falls during 4-6 rainstorm events in both regions, rainstorm intensity in the orogenic interior varies considerably more than at the orogenic front. Analysis of a 40-year time series indicates that on average, peak rainfall magnitudes vary significantly more between years in the orogenic interior than at the front. Not surprisingly, these rainstorm events have a large impact on sediment flux: During a five-year period, the two highest suspended sediment load (SSL) events lasted a total of nine days and accounted for ∼50% of the total suspended sediment flux of the Baspa Valley. These high SSL events coincide with extensive, synoptic-scale rainstorms that last on average for 2-3 days. Such peak erosional events, which re-occur at intervals of three to five years, account for large variations of modern erosion rates in the Baspa Valley (1.05 ± 0.8 mm/yr). Thus, despite the great importance of winter westerly-derived moisture for glaciers and river discharge in the orogenic interior, sporadic heavy monsoonal rainstorms dominate the fluvial sediment flux.

Chapter 4

Differentiating between rainfall, snow, and glacier contributions to river discharge in western Himalaya using distributed hydrological modeling

Abstract

The discharge of large Himalayan rivers is mainly sourced by rainfall, snow and glacial melt. Their relative contributions are not well understood, because this remote region lacks ground-based climatological data, despite the river's importance for maintaining agriculture, drinking water and hydropower generation. Here, we quantify the spatiotemporal distribution of hydrologic components and their relative contribution to river discharge in the Sutlej Valley (∼55,000 km^2) in the western Himalaya. We model daily runoff from 2000-2008 derived from rainfall, snow and glacial melt, and evapotranspiration losses. Rainfall is based on adjusted TRMM (Tropical Rainfall Measuring Mission) product 3B42. TRMM-derived rainfall compared to 81 weather stations performs reasonable well (within $<$10%) at the humid orogenic front but increasingly overestimates rainfall by a factor of 2-6 in the arid orogenic interior. Snow and glacial melt are computed from a distributed enhanced temperature index model based on MODIS (MODerate resolution Imaging Spectroradiometer) imagery corrected for snow-cloud misclassifications, cloud-cover gaps, and viewing angle artifacts. Our hydrological model indicates that the Sutlej River's annual discharge is derived to 47% by effective rainfall (rainfall reduced by evapotranspiration), and to 43% by snow and to 10% by glacial melt and experiences strong seasonal and spatial variations. The glacial contribution to river discharge equals an average glacial ablation of 0.93±0.18 m/yr for the ice-covered areas. Our findings underscore the importance of calibrating and adjusting remote-sensing data to constrain hydrological models with reasonable accuracy in regions that lack sufficient ground-based data.

4.1 Introduction

Runoff from the Himalaya is an important source for drinking water, hydropower generation, and agriculture in the densely populated Indo-Gangetic Plains [*Barnett et al.*, 2005; *Bookhagen and Burbank*, 2010]. In light of recent climate change [*IPCC*, 2007], glacier retreat [*Bhambri and Bolch*, 2009; *Scherler et al.*, 2011a], steady population growth [*Jodha*, 1985; *WDI*, 2010] and the occurrence of widespread groundwater lowering [*Rodell et al.*, 2009] quantitative assessment of the available water resources in this region is a crucial task [*Immerzeel et al.*, 2010]. Although discharge generated from melting of snow and ice is generally assumed to be significant, the scarcity of detailed ground-based observations make quantification of their relative contributions to Himalayan discharge difficult.

Hydrological models are useful tools to explore and quantify fluvial discharge. Runoff from melting snow and ice is commonly estimated using either surface-energy balance [*Anderson*, 1976] or temperature-index models [*Lang and Braun*, 1990; *Martinec*, 1975; *Rango and Martinec*, 1995]. In the Himalayan region, surface-energy balance approaches are not feasible, because of the weakly constrained boundary conditions (e.g. wind speed, water-vapor pressure). In contrast, temperature-index models, which represent simplified empirically based alternatives, require less input data that are usually available for most regions on Earth. However, their simplicity may lead to lower accuracy and larger uncertainties of the results [*Ferguson*, 1999; *Hock*, 2003; *Pellicciotti et al.*, 2005]. To better capture the generation of melt water, the shortwave radiation balances can be included in so-called enhanced temperature-index models [*Hock*, 1999; *Pellicciotti et al.*, 2005; *Rango and Martinec*, 1995]. Furthermore, spatially distributed models are able to account for the high spatial variability of meteorological parameters in mountain regions [*Gurtz et al.*, 1999], but require input data that match the spatial resolution of the model domain.

To achieve complete input data coverage in distributed models, previous studies have commonly extrapolated low-elevation station data to higher altitudes [*Braun et al.*, 1993; *Li and Williams*, 2008; *Singh and Bengtsson*, 2003]. Extrapolation of station data for catchment areas $>$1000 km^2 in mountainous regions is problematic because of the high spatiotemporal variability in precipitation and temperature [*Barros et al.*, 2004; *Bookhagen and Burbank*, 2006; *Lundquist and Cayan*, 2007]. Alternatively, several satellite systems provide processed and gridded data products that can be used for hydrological modeling. In the Himalaya, this has been successfully done in studies that focused on mean-monthly discharges [e.g. *Bookhagen and Burbank*, 2010], or daily discharges in very large watersheds [e.g. *Immerzeel et al.*, 2009]. Such approaches take advantage of temporal and/or spatial averaging, which reduces the uncertainties in the remote-sensing input data that typically contain noise, artifacts, and data gaps introduced by varying surface and atmospheric conditions, specific sensor characteristics, and data processing methods [*Dozier et al.*, 2008]. Remote-sensing based modeling of daily discharges in small to medium-sized watersheds therefore requires calibration and interpolation of the input data.

The objective of this study is to analyze the spatiotemporal distribution of water resources and river runoff components of small-to-medium sized tributaries in the Sutlej catchment in the western Himalaya. We developed a hydrological model based on remote-sensing data that we calibrated with ground-based observations. As part of our modeling effort, we assess to what degree remote-sensing data, collected over steep and high relief terrain, improves the model results. We emphasize the importance of extreme monsoonal precipitation events in this part of the Himalaya that are rather short-lived but can be of high intensity and have large hydrological and geomorphological implications [*Bookhagen et al.*, 2005a; *Bookhagen*, 2010; *Wulf et al.*, 2010]. These events are difficult to capture with single snapshots provided by the remote-sensing data. Therefore, we calibrated and adjust the input data sets based on comparisons with data from 81 meteorological stations. The ground stations cover a steep north-south precipitation gradient across the main Himalayan crest and range in elevation from 0.4 km to 4.1 km above sea level (asl) [*Wulf et al.*, 2010]. We use daily river-discharge records from five gauging stations on the Sutlej River and four of its major tributaries to calibrate and validate our model between 2004 and 2008. This enables us to quantify the discharge components, their uncertainties, and their spatial variation across different climatic zones in the Sutlej catchment.

4.2 Study area

The Sutlej River is a tributary of the Indus River and has the third largest catchment in the Himalaya. Its mountainous catchment area is 55,000 km^2 with approximately two-thirds located in China (Tibet) and one third in India (Figure 4.1). Surface elevations range from 0.4 km to 7.2 km asl with a catchment-average altitude of 4.4 km asl. More than 80% of the catchment area is located at >4 km asl and extends up to 200 km northeast of the mountain front into the semi-arid to arid orogenic interior (Figure 4.2). Vegetation cover is thick and dense at lower elevations at the mountain front, but decreases rapidly above an elevation of 3.0 km asl and is virtually

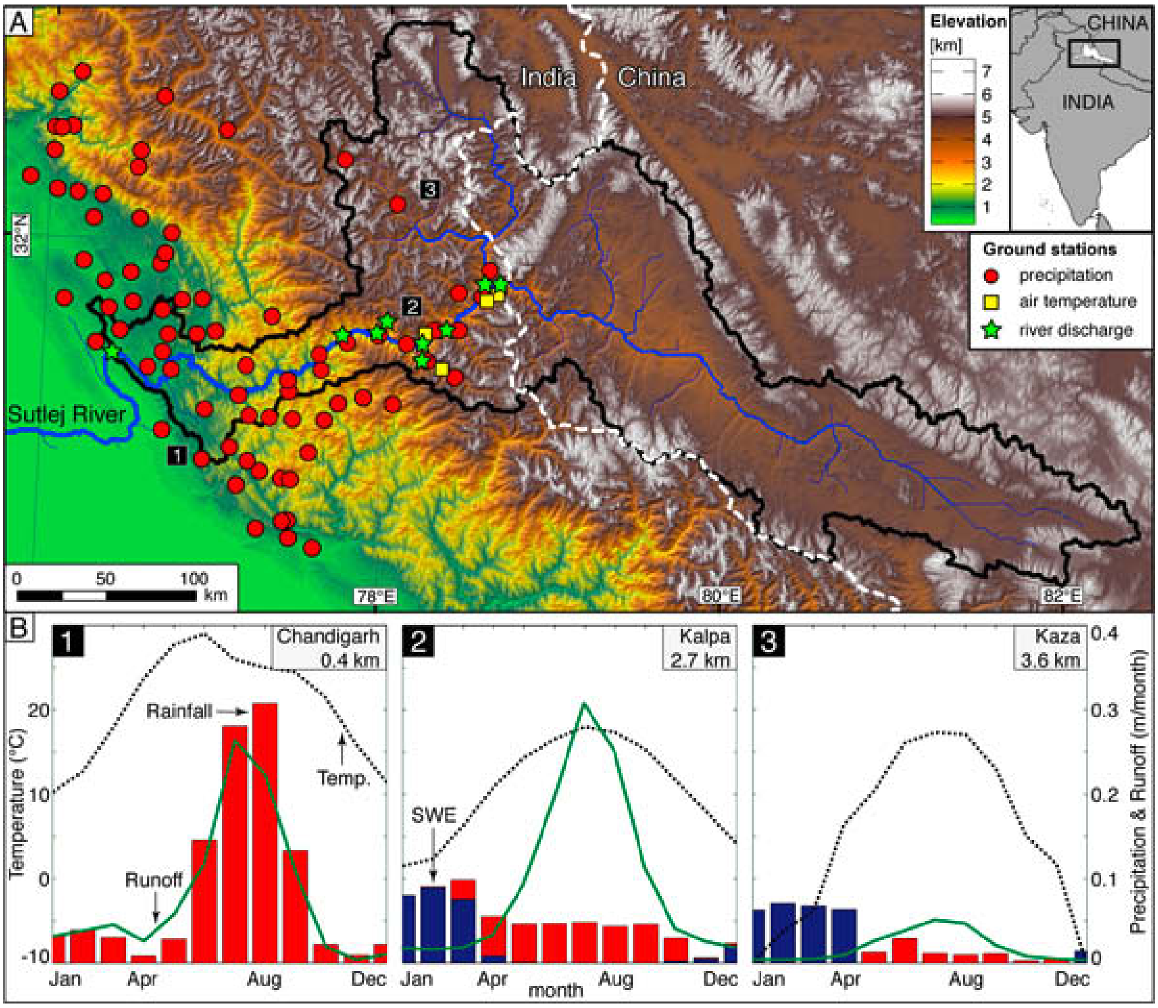

Figure 4.1: Overview of the study area, ground stations, and regional climatic characteristics. (A) Shaded relief and elevation map of the western Himalaya with inset showing map location. Black polygon outlines the Sutlej catchment and defines the hydrologic model domain; white dashed line is the international border between India and China. Red circles indicate weather stations recording rainfall and partially snow water equivalent. Yellow squares represent weather stations in Rakchham, Kalpa, Khab and Namgia (south to north), which additionally record daily minimum and maximum temperatures. Green stars denote river gauging stations of the Sutlej main stem and tributaries (t) at Bhakra, Ganvi (t), Wangtoo, Wanger (t), Baspa (t), Powari, Karoo, Spiti (t), Namgia (west to east). (B) Characteristic ground-station data showing mean monthly temperature, precipitation, and runoff at the orogenic front (1), at the main Himalayan crest (2), and at the southern Tibetan plateau (3).

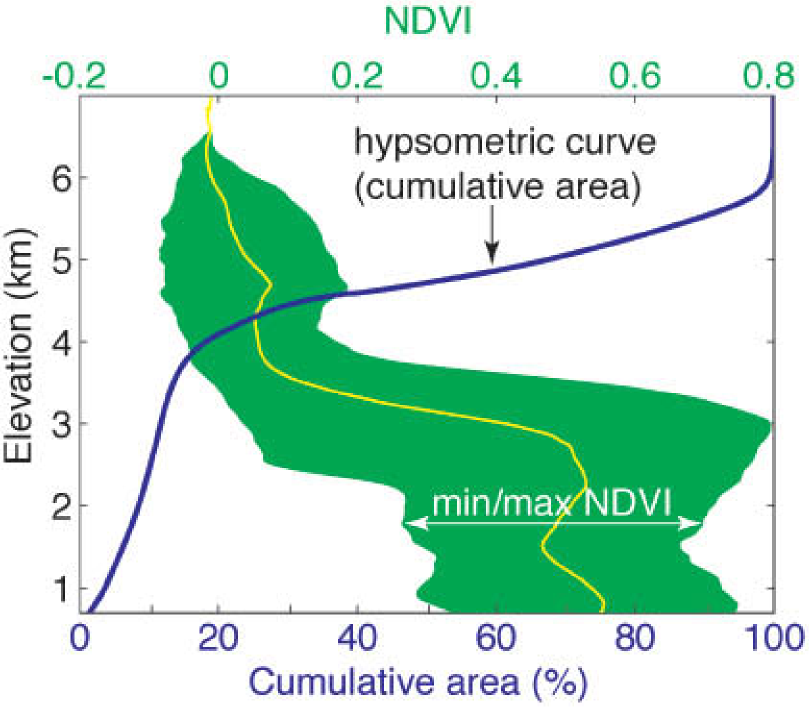

Figure 4.2: Hypsometry of the Sutlej River catchment and its vegetation distribution illustrated by the Normalized Difference Vegetation Index (NDVI) based on MODIS vegetation data. Note that the vast majority of the catchment is situated at elevations above 3.5 km asl displaying no vegetation cover.

absent >3.5 km asl. Therefore, the primary land cover in the Sutlej Valley is bare ground (81.2 %), as compared to trees and shrubs (7.2 %), cultivated areas (6.8 %), glaciers (3.7 %), and lakes (1.1 %) [*FAO*, 2009]. This indicates that developed soils are present only in the lower part of the Sutlej catchment, which constitutes a small fraction (<15%) of the entire catchment area (Figure 4.2) and therefore is likely to have a low impact on overall water storages.

Precipitation in the western Himalaya has pronounced seasonal and spatial variations [*Bookhagen and Burbank*, 2010]. Snowfall occurs mostly between December and March and increases with elevation [*Singh and Kumar*, 1997; *Winiger et al.*, 2005]. During the summer months, the Indian monsoon (mid July – mid September) accounts for intense precipitation, which is focused windward of orographic barriers along the frontal Himalaya [*Bookhagen and Burbank*, 2006]. Previous studies suggest that at ~78ºE in the vicinity of the Sutlej Valley exists a longitudinal break in seasonal moisture supply: Regions to the east of the Sutlej (including the Sutlej) are heavily affected by the Indian Summer Monsoon with more than 60% of rainfall occurring between the months of May and October. In contrast, regions to the west of the Sutlej receive most rainfall outside the summer monsoon season [*Barros et al.*, 2004; *Bookhagen and Burbank*, 2010]. The orographic barrier of the Higher Himalaya prohibits monsoonal moisture to migrate northward into the orogen and creates a steep orographic rainfall gradient. Rainfall decreases from >2 m at the fontal parts to <0.2 m in the interior parts of the orogen over a horizontal distance of <100 km [*Wulf et al.*, 2010]. Several studies suggest that during active monsoon phases strong convective cells migrate across this orographic barrier and result in heavy rainfall events in the orogen interior, where these can mobilize enormous amounts of sediments [*Bookhagen et al.*, 2005a; *Craddock et al.*, 2007; *Wulf et al.*, 2010].

4.3 The hydrological model

We use a hydrological model to simulate mean daily river discharge from April 2000 to August 2008. The model calculates runoff in each 500 x 500 m grid cell for the Sutlej catchment (Figure 4.1). Daily river discharge (Q_{sim}) at a given location is computed from the upstream runoff, derived from snow melt (M_S), glacial melt (M_G), and effective rainfall that is rainfall (PR) reduced by evapotranspiration (ET), according to:

$$Q_{sim} = M_S + M_G + P_R - ET \tag{4.1}$$

The input data for rainfall and evapotranspiration are obtained from calibrated remote-sensing products, and discussed in section 4.4.2 and 4.4.7.

4.3.1 Snow- and glacial melt

Based on previous studies [*Cazorzi and Dallafontana*, 1996; *Hock*, 2003; *Li and Williams*, 2008; *Martinec*, 1975; *Pellicciotti et al.*, 2005; *Rango and Martinec*, 1995], we developed a spatially distributed temperature-index model that incorporates the influences of solar radiation, snow albedo, and cloud cover. Daily snow melt (M_S in mm day^{-1}) is calculated for every snow-covered pixel according to:

$$M_S = \begin{cases} T \cdot R_{net} \cdot A_{snow} \cdot mf_{snow}, & T > 0°\mathrm{C} \\ 0, & T > 0°\mathrm{C} \end{cases} \tag{4.2}$$

where T (°C) is the mean daily temperature (see section 4.4.4), R_{net} (W m^{-2}) is the mean daily net solar radiation, A_{snow} (m^2) is the snow-covered area, and mf_{snow} (mm °C^{-1} W^{-1} day^{-1}) is a constant melt factor for snow (Table 4.1).

Glacial melt M_G (mm day^{-1}) is calculated by the same approach as snow melt but occurs only if the corresponding pixel is snow-free:

$$M_G = \begin{cases} T \cdot R_{net} \cdot (A_{ice} + A_{debris} \cdot 0.5) \cdot mf_{ice}, & T > 0°\mathrm{C} \\ 0, & T > 0°\mathrm{C} \end{cases} \tag{4.3}$$

where A_{ice} (m^2) is the glacier area with clean ice exposure, A_{debris} (m^2) is the glacier area with debris cover and mf_{ice} (mm °C^{-1} W^{-1} day^{-1}) is a constant melt factor for clean ice melt, which we reduce for debris-covered ice by 0.5 due to its shielding effect on radiation and heat fluxes [*Braun et al.*, 1993; *Huss et al.*, 2008]. We optimize the melt factors (mf_{snow}, mf_{ice}) based on the best fit between the observed and simulated river discharge.

Net solar radiation is the balance between incoming and outgoing shortwave (R_S) and longwave (R_L) radiation.

$$R_{net} = (R_{S\downarrow} - R_{S\uparrow}) + (R_{L\downarrow} + R_{L\uparrow}) \tag{4.4}$$

We compute net shortwave radiation as [*Pellicciotti et al.*, 2005]:

$$R_{S\downarrow\uparrow} = R_{sky} \cdot f_{cc} \cdot (1 - \alpha) \tag{4.5}$$

where, $R_{clear\,sky}$ (W m^{-2}) is the incident clear sky solar radiation as described in section 4.4.5, f_{cc} is a dimensionless factor, ranging between 0.63 and 1, which accounts for reduction of clear sky radiation due to cloud cover (see section 4.4.5) and a is the snow or ice albedo.

We computed the longwave radiation balance based on the following equation [*Plummer and Phillips*, 2003]:

$$\begin{aligned} R_{L\uparrow\downarrow} = \; & \left\langle (1 + 0.26 \cdot fcc) \cdot \left\{ 1 - 0.261^{\left[-7.77 \cdot 10^{-4} \cdot \left(273 - T_a^2\right)\right]} \right\} \cdot \sigma \cdot T_a^4 \right\rangle \cdot V_f \\ & + (0.4 \cdot \sigma \cdot T_s^4) \cdot (1 - V_f) - 0.99 \cdot \sigma \cdot T_s^4 \end{aligned} \tag{4.6}$$

where *fcc* is the fractional cloud cover, T_a (K) is the mean daily air temperature, T_s (K) is the mean daily surface temperature, V_f is the sky-view factor ranging from 0 to 1 and σ (=5.67 x 10^{-8} W m^{-2} K^{-4}) is the Boltzmann constant. As melting snow and ice have an approximate surface temperature of 0°C, we use a constant T_s of 273.15 K [*Brock and Arnold*, 2000]. A more detailed description of input parameters and the physical background is given by *Plummer and Phillips* [2003], *Arnold et al.* [1996], and *Male and Granger* [1981].

4.3.2 Runoff routing

Due to the travel distance between runoff producing pixels and the downstream discharge observation there exists a time lag between the daily temperature cycle and the corresponding discharge cycle. We account for the time lag by computing the flow time for each pixel, based on its flow path and its approximate flow velocity. We calculated the flow paths by the D8 flow accumulation algorithm and the flow velocities based on Manning's equation for gravity flow in open channels, which we tuned by field observations from the Sutlej River. Subsequently, we delayed runoff for each pixel according to its flow time in integer days (n) and portioned its sub-daily fractions (hourly delay) between day (n) and day (n+1) based on the inverse ratio of the fractions.

To account for runoff storage in subsurface reservoirs we employed two linear stores as for example used in the hydrological modeling system PREVAH [*Gurtz et al.*, 1999; *Viviroli et al.*, 2009]. In our approach, we use the minimum of two adjustable parameters to avoid unpredictable parameter interaction. The first parameter adjusts between fast and delayed runoff formation from the upper store, the second parameter controls the percolation into the lower store, which generates the baseflow based on a constant recession coefficient. We argue that this simplified, but computationally efficient approach, captures transient runoff storage in these environments and at the timescales considered.

4.4 Model input data and calibration procedures

4.4.1 Ground station data

The weather station data comprise 63 weather stations from the Indian Meteorological Department (IMD) and 17 high-elevation stations operated by the Bhakra Beas Management Board (BBMB) (Figure 4.1). The IMD stations record rainfall only, while BBMB stations additionally measure snow water equivalent (SWE). Furthermore, three BBMB stations (Figure 4.1) record daily maximum and minimum temperatures and one automated weather station at Khab records hourly data of rainfall, temperature, and incident solar radiation. We checked the precipitation data for plausibility according to quality-control measures introduced by *Einfalt and Michaelides* [2008] and excluded unreliable values from subsequent analyses [*Wulf et al.*, 2010]. The available precipitation records cover a ten-year time span from 1998 to 2008, but lack completeness by 33% on average.

In the Indian part of the Sutlej Valley, several hydropower companies operate a dense network of river gauging stations. Most station records cover the time span from January 2004 to August 2008, although a severe flood in the Sutlej River on June 26, 2005 has led to some interruptions. The stream measurements are based on stage-discharge rating curves, which are annually recalculated during low flow conditions in winter, because of channel bed changes.

4.4.2 Rainfall

Rainfall in the runoff model is derived from the TRMM product 3B42, which has a spatial resolution of 0.25° x 0.25° (∼30 km x 30 km) and a temporal resolution of 3 h. This data set combines microwave and infrared rain-rate estimates from sensors onboard several low-earth orbit and one geosynchronous satellite, which are rescaled to monthly rain-gauge data [*Huffman et al.*, 2007].

Previous studies suggest that the TRMM 3B42 product is comparable to other satellite based rainfall products, which generally show a lower performance in complex terrain [e.g. *Dinku et al.*, 2008; *Maussion et al.*, 2010; *Sapiano*, 2009; *Tian et al.*, 2009]. Although the spatial resolution of the TRMM 3B42 data makes direct comparison to weather station data difficult, *Pan et al.* [2010] found in a recent comparison of different satellite-based precipitation products for the United States that rain-gauge assisted corrections of satellite products significantly enhance their skill in hydrologic predictions, especially over mountainous areas.

We assessed the quality of the TRMM 3B42 product by comparison with weather station rainfall records across our study area. This validation shows that filtering and scaling of TRMM 3B42 rainfall data is required, as it does not capture adequately the reduction in rainfall towards the high-elevated arid orogenic interior (see section 4.5.1).

4.4.3 Fractional Snow Cover (FSC)

Snow melt in our model occurs when a given pixel is snow covered and temperatures are above zero. We used daily fractional snow cover (FSC) observations that are derived from the MODIS instrument onboard the Terra and Aqua satellites of the NASA Earth Observation System. The globally available MOD10A1 (Terra) and MYD10A1 (Aqua) products (current version 5) provide daily observations of FSC and snow albedo, with a spatial resolution of 500 m [*Hall et al.*, 1995]. Terra images are available since March 2000 and Aqua images since July 2002. The MODIS snow detection algorithm employs the Normalized Difference Snow Index (NDSI), which determines the difference in reflectance of snow between visible and short infrared wavelengths [*Hall et al.*, 2002, 1995]. FSC gives the fraction of a pixel, which is snow covered, and is computed from a functional relationship between MODIS NDSI and higher resolution Landsat FSC data [*Salomonson and Apple*, 2004]. Comparison of MODIS snow products with in situ snow measurements in the western US and Austria have yielded accuracies of 94% to 95% [*Klein and Barnett*, 2003; *Parajka and Blöschl*, 2006].

The utility of the MODIS snow-cover products for hydrological modeling is limited by cloud cover, which causes data gaps. We reduced these data gaps by first combining Terra and Aqua observations from the same day [*Dozier et al.*, 2008; *Gafurov and Bárdossy*, 2009]. As a result, the average data gaps caused by clouds reduce from 42.1±27.8% to 25.8±21.6%. In a next step, we corrected for artifacts introduced by large viewing angles and other systematic errors with spline interpolation on the FSC time series. The smoothing splines are weighted based on the sensor zenith angle, which is provided in the MODIS surface reflectance product MOD09GA [*Dozier et al.*, 2008]. Finally, we filled the remaining data gaps by piecewise linear interpolation [*Fritsch and Carlson*, 1980].

Besides cloud cover gaps, the daily MODIS snow-cover product is also affected by snow/cloud discrimination errors [*Dozier et al.*, 2008; *Hall and Riggs*, 2007]. Despite improvements in the cloud detection algorithm in the recent version (v5), MODIS occasionally confuses cloud with snow cover. These problems are associated with cloud-shadowed land and cloud type identification errors [*Hall and Riggs*, 2007]. To filterer erroneous snow cover, we established a daily minimum snow-cover elevation, which is based on the daily average snow cover at discrete 0.1 km elevation intervals (Figure B.1A). Clouds misclassified as snow result in a low average snow cover (ca. 1-5%) at low elevations. These unusual low snow-cover elevations exhibit large residuals to elevation intervals with an average snow cover of >20%, which are less affected by clouds confused with snow and typically follow the annual altitudinal snow-cover cycle (Figure B.1A). To identify days with snow misclassifications, we correlated daily elevation intervals with 1% versus 20% average snow cover, and filtered days beyond the 95% confidence interval (Figure B.1B). Finally, we fill snow-cover elevations of filtered days by linear interpolation and lower the 1% snow-cover elevation by a 0.3 km buffer to establish the daily minimum snow-cover elevation (Figure B.1A).

Based on this minimum snow-cover elevation, we analyze the temporal distribution of clouds misclassified as snow for Terra and Aqua observations (Figure 4.3).

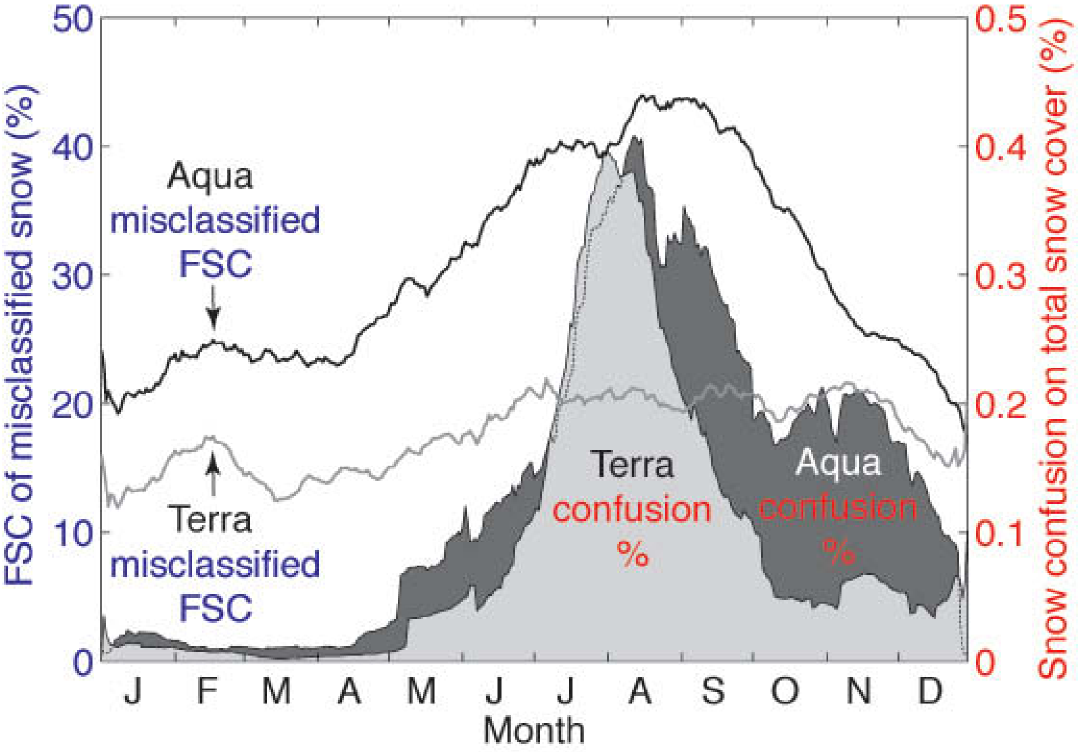

Figure 4.3: Comparison of misclassified snow by Terra and Aqua sensors. Mean annual (2000 to 2008) distribution of the mean Fractional Snow Cover (FSC) of clouds misclassified as snow and the percentage of misclassified snow on total snow cover. Although this misclassification percentage is low, it is important to filter these confusions, as they are typically associated with low elevations and high temperatures, which cause considerable snow melt runoff. We applied a 30-day moving average filter for enhanced visibility.

Here, we find pronounced snow/cloud confusions during the summer, when the Himalayan front is affected by a dense monsoonal could cover and annual snow cover is at its minimum. Because these snow misclassifications are often associated with high summer temperatures, they increase annual snowmelt in Sutlej Valley by about 6%. On an annual basis, misclassified FSC of Aqua is 2.8 times higher as compared to Terra (Figure 4.3). We also find that during dual snow-cover observations the Aqua FSC is by a factor of 0.81 lower than that Terra FSC (Figure B.2), which indicates an overall lower FSC performance of the Aqua sensor as compared to Terra.

4.4.4 Temperature

The temperature data in our model is based an average daily atmospheric lapse rate derived from the MODIS land surface temperature (LST) product (MOD11A1 and MYD11A1, current version 5). MODIS-derived LST is based on the view-angle dependent split-window LST algorithm, which corrects for atmospheric and emissivity effects in the thermal infrared signal over various land cover types [*Wan and Dozier*, 1996]. Refinements in the algorithm of the latest LST version 5 improved the accuracy and stability of LST data especially in high-altitude regions [*Wan*, 2008]. Most validation studies indicate that the accuracy of MODIS LST data is better than 1 K [*Coll et al.*, 2005; *Wan et al.*, 2004; *Wan*, 2008]. However, the precise retrieval of snow-surface temperatures is difficult, because snow emissivity varies with depth, density, and grain size [*McFarland et al.*, 1990].

Temperature-index models for estimating snow and ice melting are usually run with above-ground air temperatures, which reflect both, longwave atmospheric radiation and sensible heat flux, and thereby more than three-quarters of the entire energy source for melting [*Ohmura*, 2001]. Although surface and air temperatures correlate well throughout the year, they are not correlated during the melt period of snow and ice as surface temperatures remain isothermal at 0°C [*Datt et al.*, 2008].

The comparison of daily maximum and minimum air temperatures with MODIS Aqua and Terra day- and nighttime surface temperatures at three weather stations in our study area reveals pronounced deviations between the day- and nighttime correlations (Figure 4.4). The difference between surface and air temperatures is mainly controlled by the surface energy balance [*Prince et al.*, 1998]. Thus, daytime surface temperatures are strongly affected by radiation fluxes (e.g., solar radiation), whereas nighttime surface temperatures are less affected (Figure 4.4B).

Due to the good agreement between MODIS nighttime surface temperatures and minimum air temperatures [*Vancutsem et al.*, 2010] we calculate the average daily atmospheric lapse rate within the Sutlej Valley based on MODIS Aqua and Terra nighttime LST data (Figure 4.5). Depending on seasonal variations in the atmospheric moisture content we observe a high lapse rate during winter and a low lapse rate during summer [*Dury*, 1981]. Similar lapse rate trends and magnitudes have been observed in the neighboring Bhagirathi catchment based on mean daily weather station data [*Thayyen et al.*, 2005]. An additional comparison with eight mean monthly minimum air temperature records across the western Himalaya, ranging from 0.3 to 3 km asl, indicates a similar trend but a lower overall lapse rate (Figure 4.5). We consider the lapse rate derived from MODIS LST nighttime data as more representative, because it includes significantly more observations covering all altitudinal and spatial ranges, which is crucial for lapse rate estimations [*Rolland*, 2003]. In our temperature index model we therefore use the daily atmospheric lapse rate to extrapolate continuous daily maximum and minimum weather station temperatures from Kalpa (Figure 4.1) across our study area.

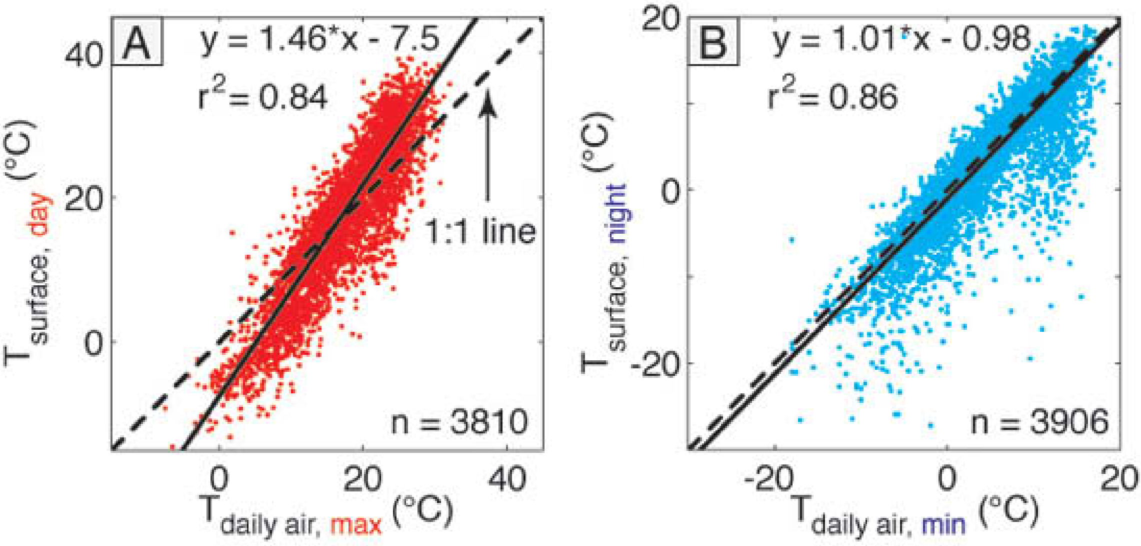

Figure 4.4: Regression of MODIS surface temperatures versus weather station air temperatures. (A) Linear regression of daily maximum air temperatures from Kalpa, Rakchham, and Namgia (cf. Figure 4.1) versus daytime MODIS Terra land surface temperatures (LST) weighted by the satellite sensor angle. In general, data with high residuals have higher sensor angles. (B) Same regression as in A for daily minimum temperatures versus nighttime MODIS Terra LST. Regressions for the MODIS Aqua sensor display the same trend (Figure B.3).

To derive melt rates based on maximum and minimum temperatures, we differentiate between two cases: First, for daily minimum temperatures above 0°C we simply use the mean of maximum and minimum temperatures. Second, during periods of nighttime freezing and daytime thaw the time span with positive degrees during day should account for melt, even if the daily mean is below zero (Figure B.4A). Therefore, we introduce a simple approach to approximate the daily mean positive temperature (T>0°C) by factorizing the maximum temperature (T_{max}) with values between 0 and 0.5, based on the minimum (T_{min}) and maximum daytime temperatures:

$$T_{>0^\circ\mathrm{C}} = T_{max} \cdot 0.5 \cdot \left(\frac{T_{max}}{T_{max} - T_{min}} \right)^{0.62} \tag{4.7}$$

4.4.5 Net radiation

The incoming shortwave radiation (clear sky radiation) is calculated using standard Geographic Information Science methods by accounting for direct and diffusive components [*Fu and Rich*, 2002]. We computed daily averages of hourly free sky incoming solar radiation, based on a digital elevation model derived from the Shuttle Radar

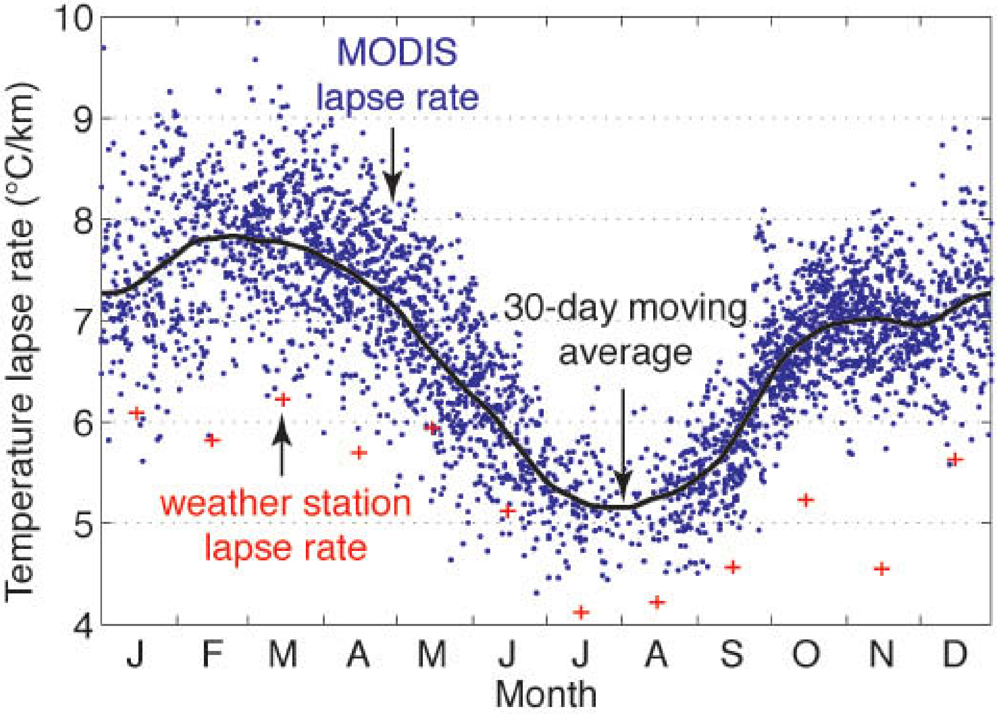

Figure 4.5: Mean daily MODIS LST nighttime atmospheric lapse rate in the Sutlej Valley. Data displays daily lapse rate of each Julian day during the period April 2000 to December 2008 from MODIS Aqua and Terra. We excluded lapse rate data with $r^2 < 0.8$ (35%) or covering less than 10% of the Sutlej Valley (3%). The black line represents the smoothing curve with a moving average of 30 days. Black crosses indicate the mean monthly temperature lapse rate of minimum temperatures from eight weather stations in western Himalaya ranging from 0.3 to 3.6 km asl.

Topography Mission (version 2) [*Farr et al.*, 2007], where voids have been patched with data from topographic maps [*de Ferranti*, 2006].

Clouds reflect and absorb incoming solar radiation [*Stephens et al.*, 1996]. We estimate this reduction in our study area by comparing observed solar radiation, measured at Khab (Figure 4.1), with the computed clear sky radiation and the daily cloud cover (Figure 4.6).

We derived a fractional cloud cover (FCC) for each pixel by averaging the cloud-flags (0 for cloud-free and 1 for cloud-covered) from MODIS observations by the Aqua and Terra satellites at three different times during the day. These are included in the FSC product (mean acquisition time: 7:44 ± 0:23 h), and the LST product from Aqua (13:12 ± 0:20 h) and Terra (16:22 ± 0.22 h).

Information on the snow albedo is part of the MODIS snow-cover product (see section 4.4.3). In situ measurements of snow albedo typically range between 0.3 and 0.9 [e.g. *Greuell and Oerlemans*, 2005], which we set to be the lower and upper snow

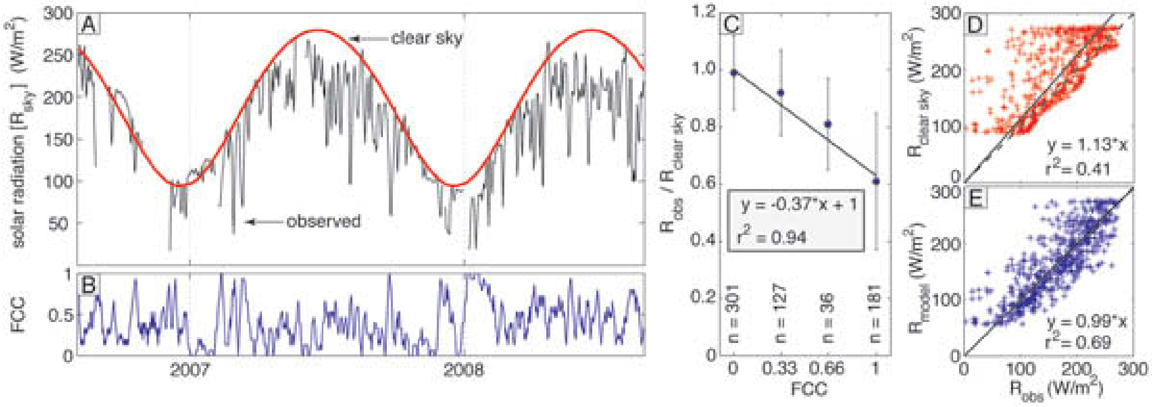

Figure 4.6: Influence of cloud cover on incoming solar radiation. (A) Comparison of mean daily observed (R_{obs}) and computed (R_{comp}) incoming solar radiation from August 2006 to August 2008. (B) Fractional cloud cover (FCC) is derived from three MODIS daytime measurements. For enhanced visibility, we smoothed FFC and R_{obs} by a 5-day running average window. (C) Correlation of R_{obs} and R_{comp} versus fractional cloud cover. The linear fit is weighted by the occurrences (n) of cloud cover fractions and fixed to the origin (x=0, y=1). (D) Scatter plot of R_{obs} and R_{comp}. (E) Scatter plot of R_{obs} and modeled solar radiation (R_{model}), which is based on R_{comp} and FCC.

albedo limits, respectively.

4.4.6 Glacial cover

We mapped the glacial inventory of the Sutlej catchment based on the following approach: First, we classified snow and debris-free ice using binary images that we generated from Landsat Thematic Mapper (TM) band TM4/TM5-ratio images [*Kääb et al.*, 2002; *Paul et al.*, 2002]. We selected Landsat ETM+ images that were acquired during late summer and autumn when snowlines are high, between the years 2000 and 2002. Second, we delineated manually the debris-covered glacial parts based on high-resolution Google Earth™images from 2010. We neglect changes in glacial coverage during our study period, because these are small compared to the spatial resolution of our model [*Scherler et al.*, 2011a]. Based on the high-resolution maps we generated fractional debris-free and debris-covered ice areas for each pixel that contains ice (Figure 4.7). For the shortwave radiation balance of the glacial surface area we use a constant surface albedo of 0.34 for debris-free ice and 0.15 for debris-covered ice [*Brock et al.*, 2010].

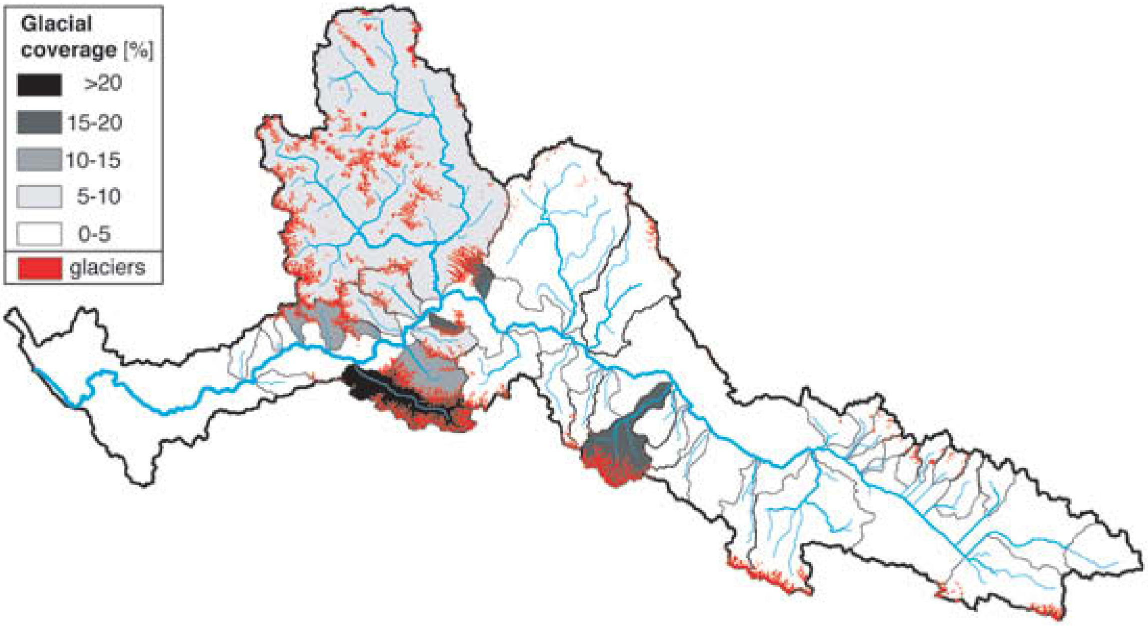

Figure 4.7: Glacial coverage for Sutlej tributary basins $>$ 100 km^2 overlain by glacial extent. The total glaciated area within the Sutlej accumulates to 2004 km^2 of which ~30% are debris-covered.

4.4.7 Evapotranspiration

Evaporation in our model is represented by a global evapotranspiration product, which is based on MODIS and global meteorological data [*Cleugh et al.*, 2007; *Mu et al.*, 2007]. The evapotranspiration algorithm is based on the Penman-Monteith method and considers surface-energy partitioning and environmental constraints on evapotranspiration [*Cleugh et al.*, 2007; *Monteith*, 1965]. The improved algorithm developed by *Mu et al.* [2007] was evaluated across different terrain types in North America and shows a reasonable good correlation ($r^2 = 0.76$) with ground-based data. However, we are aware about the difficulties of applying the Penman-Monteith method in high-relief terrain with spatially limited data for validation.

The gridded evapotranspiration data are 8-day composites with a spatial resolution of 1 km. After resampling the data to the model projection and spatial resolution (500 m) we disaggregated the 8-day composite to daily data. Because there are no developed soils in more than 85% surface area of the Sutlej catchment, we assume soil water storage is negligible. Therefore we consider only evaporation from the surface layer during days with rainfall. The resulting effective precipitation (rainfall reduced by evapotranspiration) has an average annual evaporated fraction of 0.16 (Figure B.5), which agrees well with field-based data from the Central Himalaya, where ~15% of the daily moisture supply is recycled by evapotranspiration *Barros and Lang* [2003].

4.5 Results and Discussion

4.5.1 TRMM 3B42 vs. weather station rainfall

The comparison of TRMM 3B42 with 81 weather station data reveals that TRMM captures in situ rainfall at the humid orogenic front within <10% but overestimates rainfall by >60% in the high-elevated arid orogenic interior (Figure 4.8). This mismatch in rainfall magnitudes is especially pronounced during the summer season (May-October), when monsoonal rainfall magnitudes decrease significantly leeward of the orographic barrier. During the winter season TRMM also indicates substantial rainfall amounts in the high-elevated orogenic interior, although winter westerly moisture precipitates predominantly in form of snow (Figure 4.8B). Given the coinciding increase in TRMM rainfall rates with snowfall, it appears that TRMM 3B42 mixes the signals and has difficulties to distinguish between snow- and rainfall. To overcome this problem we filtered the satellite-based rainfall data using MODIS snow cover and maximum daily temperatures (see section 4.4.4). With this approach, we aim to remove snow-rain confusions at higher elevations throughout the year.

Across our study area we find a strong correlation between mean annual rainfall magnitude of weather stations and the scaling factor by which TRMM 3B42 over- or under-predicts ground measurements (Figure 4.9A). This negative exponential relation shows that TRMM 3B42 data overestimates in situ rainfall in the high-elevated arid orogenic interior by a factor of 2-6, whereas it slightly underestimates rainfall peaks at the humid orogenic front (Figure 4.9C). It is not clear if this is a systematic bias in the TRMM-based rain rate, an effect of the temporally sparse sampling, discharge-rescaling effects, or due to high spatial variability of rainfall and associated aliasing. To test the ability of TRMM to detect daily rainfall events we compare daily rain rate observations by TRMM with the weather station records (Figure 4.8B). The comparison examines the TRMM performance based on its ability to detect (hit), not detect (miss), and falsely predict (false alarm) rainfall events. Similar to the trend in mean annual rainfall we find a reasonably good performance (∼80% hit rate, ∼40% false alarm rate) of TRMM 3B42 at the orogenic front, whereas towards the interior of the orogen, TRMM has fewer hits and greater false alarms (∼60% hit rate, ∼70% false alarm rate) compared to the weather station rainfall events. This comparison also reveals that the performance of TRMM 3B42 increases with increasing rainfall magnitudes throughout the region. The overall trend in the TRMM 3B42 performance with respect to weather-station records shows that TRMM does not capture adequately the reduction in rainfall within the orogenic interior, which requires a

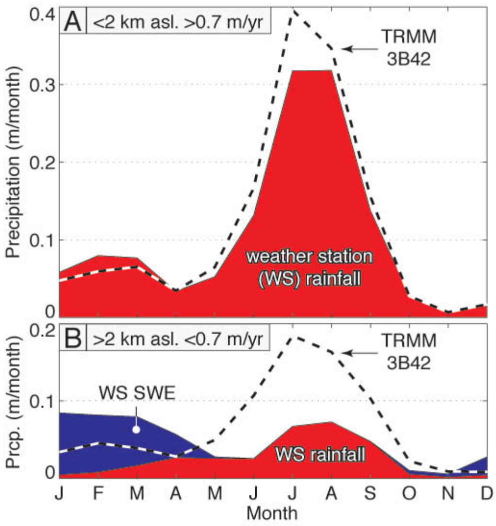

Figure 4.8: Comparison of TRMM 3B42 and weather station rainfall data. (A) Comparison of TRMM 3B42 with WS rainfall data at 52 locations below 2 km asl for the time period 2000 to 2007. Mean annual rainfall in this region is >0.7 m/yr. (B) Comparison of TRMM 3B42 (2000 to 2007) with snow water equivalent (SWE) and rainfall data of 17 weather stations (WS) located above 2 km asl, where mean annual rainfall is <0.7 m/yr.

spatially varying filter. We scale the mean annual TRMM 3B42 rainfall based on its relation to ground rainfall (Figure 4.9A) und use the ratio of scaled and original mean annual TRMM rainfall to correct the daily TRMM 3B42 rainfall input in our hydrological model.

4.5.2 Simulated river discharge

Based on our enhanced distributed hydrological model and the remotely sensed input data we simulated river discharge at nine locations (green stars in Figure 4.1) covering various spatial scales and climatic environments (Table 4.1). In order to assess the performance of the hydrological model we calculate the Nash-Sutcliffe efficiency measure (NSE) [*Nash and Sutcliffe*, 1970] and a normalized benchmark efficiency measure (BE). The BE is recommended by the *WMO* [1986] for the intercomparison of temperature index models, as the NSE has a lower explanatory power for time series with a pronounced seasonal signal [*Garrick et al.*, 1978; *Schaefli and Gupta*, 2007]. Contrary to the mean observed discharge utilized in the NSE, the BE is based on the interannual mean discharge for every calendar day. With the exception of Ganvi River discharge (2001-2005), we calibrated the model for each catchment based on observed daily river discharges during 2004 to 2008, which allows for direct comparison between catchments.

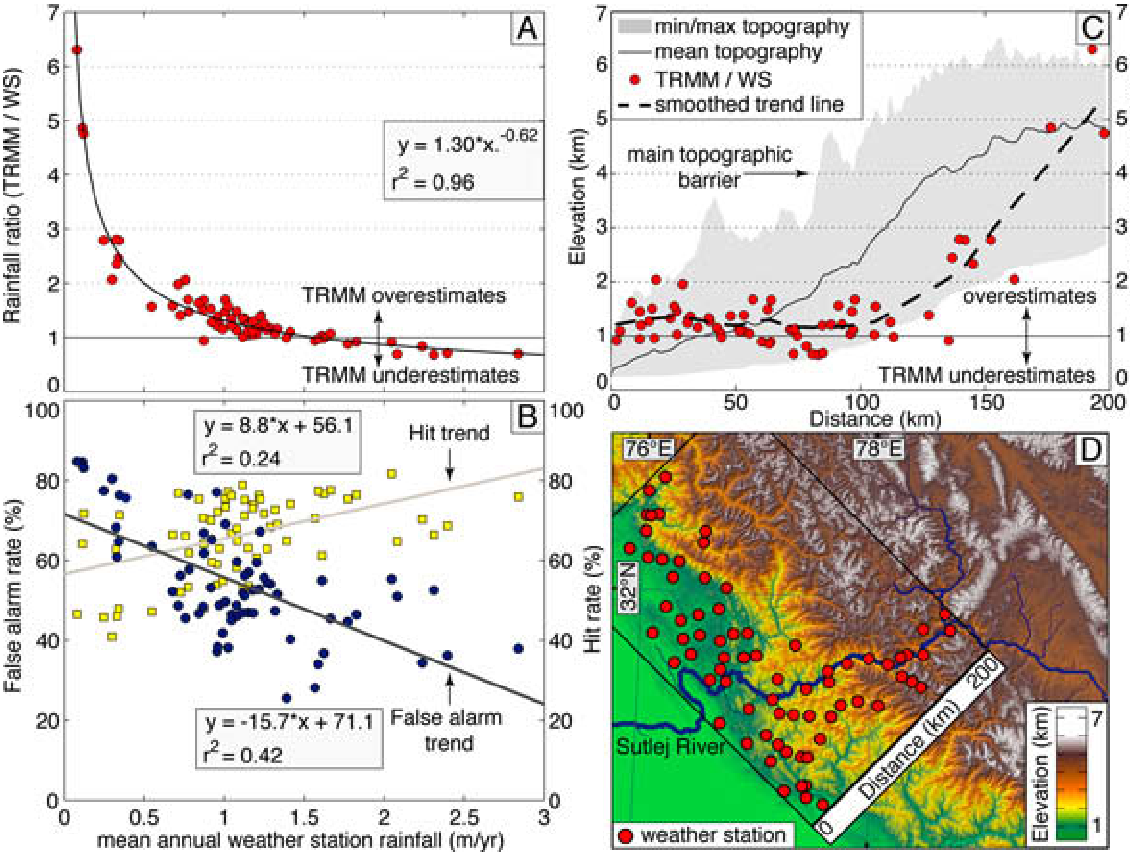

Figure 4.9: Relation of TRMM 3B42 to weather station rainfall data. (A) Correlation of mean annual weather station (WS) rainfall data versus the ratio of mean annual TRMM 3B42 to WS data for the period 2000 to 2008. This rainfall ratio indicates a scaling factor by which TRMM over- (>1) or underestimates (<1) weather station records. (B) Analysis of TRMM 3B42 data regarding its probability of detection and misinterpretation of daily rainfall at weather stations. The comparison only includes rainfall records above 2 mm, which represents the minimum recording level of weather stations. False Alarm (FA) rate = FA/(Hit+FA)*100, Hit rate = Hit/(Hit+Miss)*100. (C) Topographic swath profile of the western Himalaya and the mean annual precipitation ratio of TRMM 3B42 and WS records. (D) Location of weather stations and the topographic swath profile.

Table 4.1: Topographic and hydrological characteristics of the modeled watershed and their modeling results. Locations of the catchments are indicated in Figure 4.1.

Catchments		*Characteristics*							*Hydrological Model*						
		Area	Elevation		Relief	Ice	Runoff		Model coefficients		Discharge sources			Performance	
			min	max	(km/	area	(m		mf$_{SNOW}$	mf$_{ICE}$	Snow	Ice	Rain-ET	NSE	BE
		(km^2)	(km)	(km)	5 km)	(%)	yr^{-1} m^{-2})		(mm °C^{-1} W^{-1} day^{-1})		(%)	(%)	(%)		
Tributaries	Spiti	12,477	2.6	6.7	1.68	6.7	0.23		0.026	0.026	68	20	12	0.79	0.21
	Baspa	989	2.5	6.4	2.21	24.0	1.16		0.040	0.023	70	13	17	0.84	0.30
	Wanger	264	2.5	5.7	2.24	17.2	1.59		0.049	0.027	80	11	8	0.81	0.47
	Ganvi	117	1.6	5.6	2.58	3.7	1.25		0.050	0.022	64	1	36	0.44	-0.58
Watersheds	Sutlej at Namgia	30,950	2.6	7.2	0.93	1.8	0.06		0.018	0.022	49	14	37	0.72	0.25
	Sutlej at Karoo	46,025	2.2	7.2	1.21	3.6	0.14		0.029	0.026	66	17	17	0.82	0.33
	Sutlej at Powari	46,291	1.9	7.2	1.22	3.6	0.15		0.030	0.027	66	17	18	0.83	0.18
	Sutlej at Wangtoo	48,316	1.5	7.2	1.27	4.1	0.20		0.034	0.026	68	15	17	0.84	0.21
	Sutlej at Bhakra	54,926	0.4	7.2	1.30	3.6	0.23		0.031	0.024	43	10	47	0.78	0.29

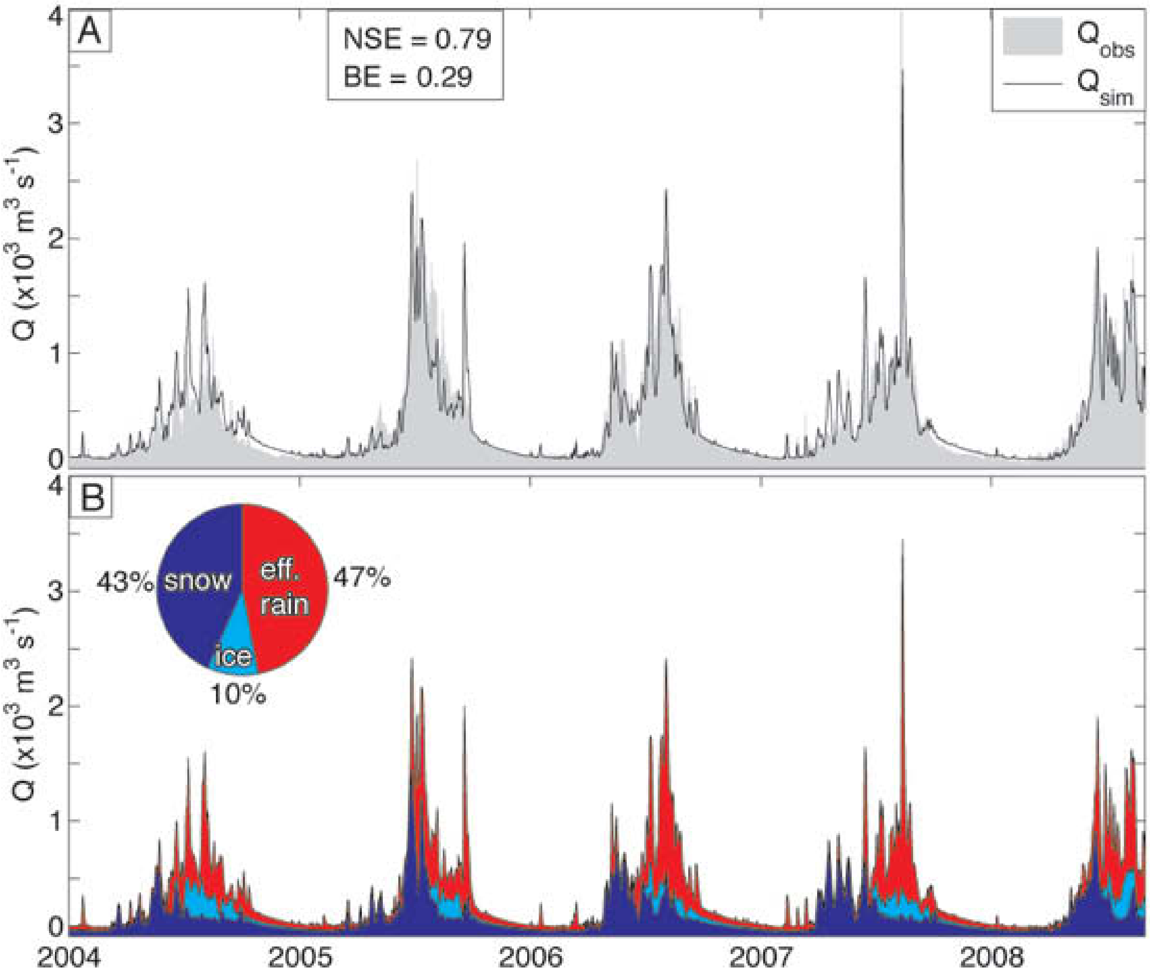

Figure 4.10: (A) **Comparison of the observed and simulated daily discharges** of the Sutlej River at Bhakra near the outlet at the mountain front (cf. Figure 4.1) from January 2004 to August 2008. (B) Sum of the single simulated discharge components illustrating the different contributions to total runoff. Pie chart represents the contribution of each runoff component to total discharge over the 5-year period.

In general, simulated river discharges capture very well the observed discharges (Figure 4.10), with one exception. The smallest and lowest elevated tributary (Ganvi), which is most influenced by rainfall, is not represented adequately by the model. The remaining watersheds yield high performance measures with NSE values ranking between 0.72 and 0.84 and show a high degree of consistency among each other (Table 4.1).

Our modeling results indicate that annual Sutlej River discharge (Sutlej at Bhakra) is sourced approximately half by effective rainfall (47%) and half by snow (43.3%) and glacial melt (9.7%) (Table 4.1). The contribution of glacial melt to Sutlej River discharge ranges between 10-20%. Rainfall dominates runoff in catchments at the

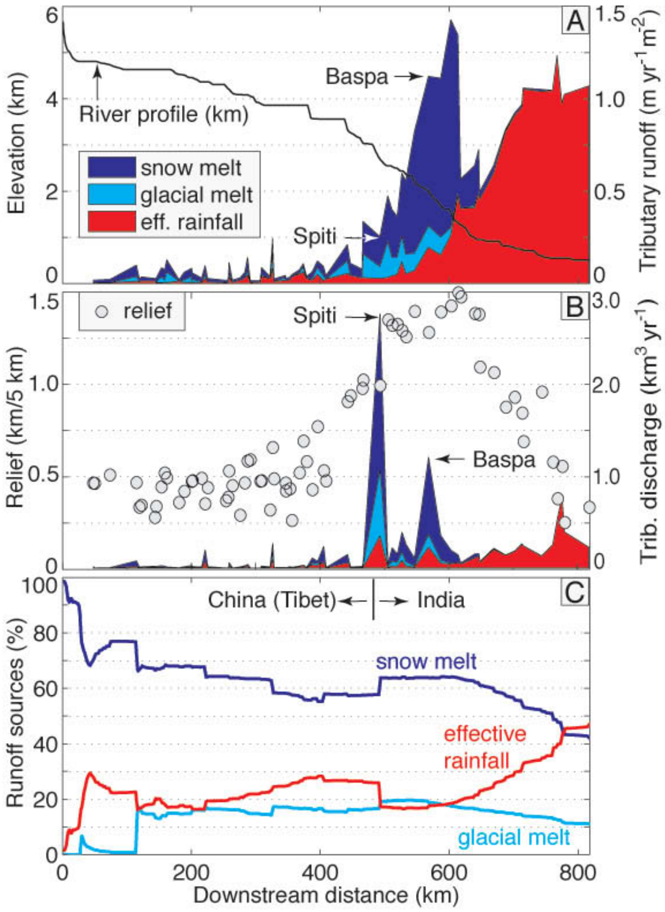

Figure 4.11: Spatial variation of hydrological components. (A) Distance and elevation of the Sutlej longitudinal river profile along with mean annual (2000-2008) runoff of tributaries >100 km^2. (B) Local relief within a 5-km radius and mean annual (2000-2008) river discharge of Sutlej River tributaries >100 km^2. Color-coding is given in A. (C) Runoff sources of the mean annual Sutlej river discharge along its river profile.

Himalayan front, whereas snow melt dominates catchment runoff in the high elevated southern Tibetan Plateau and the main Himalayan crest.

4.5.3 Spatiotemporal distribution of hydrologic components

In general, mean annual runoff within the Sutlej Basin is characterized by major regional differences (Figure 4.11A). The southern Tibetan Plateau is characterized by low precipitation and runoff due to its low relief and its location leeward of the main orographic barrier. The high-relief region of the main Himalayan crest effectively captures snowfall, which is also reflected by a high glacial density (Figure 4.7). Increases in snow and glacial melt are accompanied by moderate increases in monsoonal rainfall and result in an increase of the mean annual river discharge by up to one order of

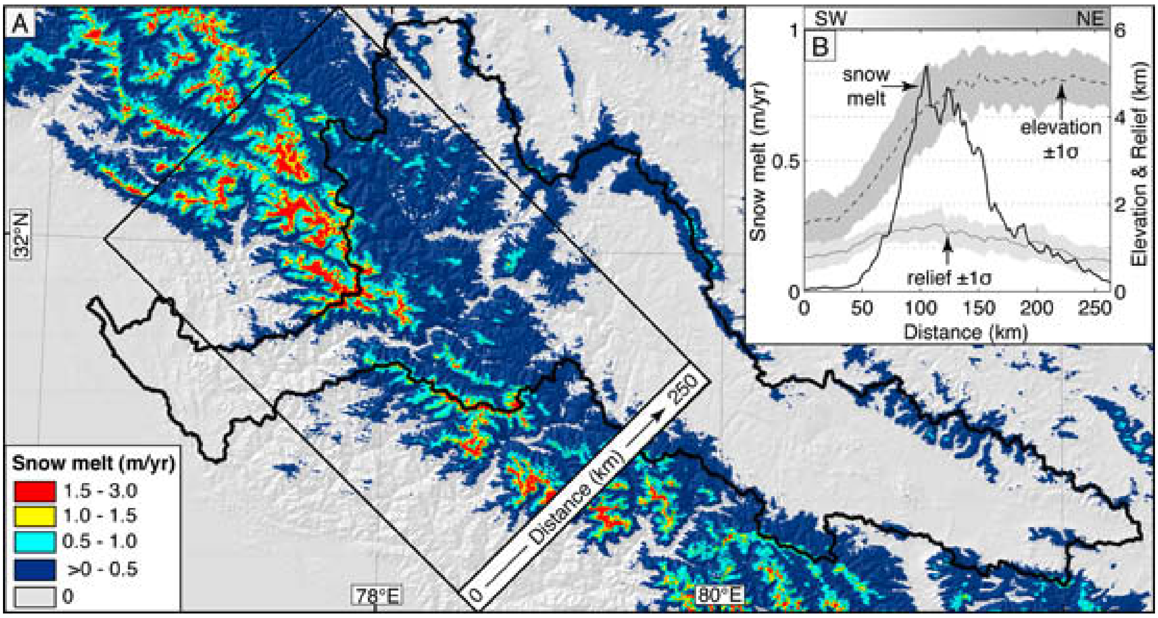

Figure 4.12: (A) **Mean annual snow melt** (2001-2007) of the western Himalaya based on an average snow melt factor of mfsnow = 0.03 mm °C^{-1} W^{-1} day^{-1}. (B) Swath profile across the western Himalaya showing the average distribution of snow melt along with elevation ($\pm 1\sigma$) and a 5-km radius relief ($\pm 1\sigma$).

magnitude. Interestingly, this region of pronounced snow and glacial melt coincides with the steepest section of the Sutlej River profile where topographic relief is highest (Figure 4.11A, 4.11B). The Himalayan front is dominated by rainfall due to lower elevations and its location windward of the main orographic barrier. Increasing vegetation cover and temperatures cause high evapotranspiration rates while snow and glacial melt decrease significantly.

The cumulative runoff of each Sutlej River tributary ($>$100 km^2) shows that the Spiti and Baspa River are the major contributors of the Sutlej River (Figure 4.11B). Analysis of the relative contributions to Sutlej River discharge in the downstream direction reveals that snowmelt is the dominant runoff source up to the point where monsoonal rainfall becomes the dominant component at the Himalayan front (Figure 4.11C).

We quantify the spatial distribution of snow melt for the period 2001 to 2007 by the “inverse melt” approach [*Molotch and Norte*, 2009] (Figure 4.12A). This annual summation of daily snow melt yields represents all melted snow during a year. Although snow can persist throughout the melt season at high elevations, snow accumulation areas are mainly restricted to glacial accumulation zones. Therefore, we assume that our snow melt summation is roughly equal to annual amounts of SWE.

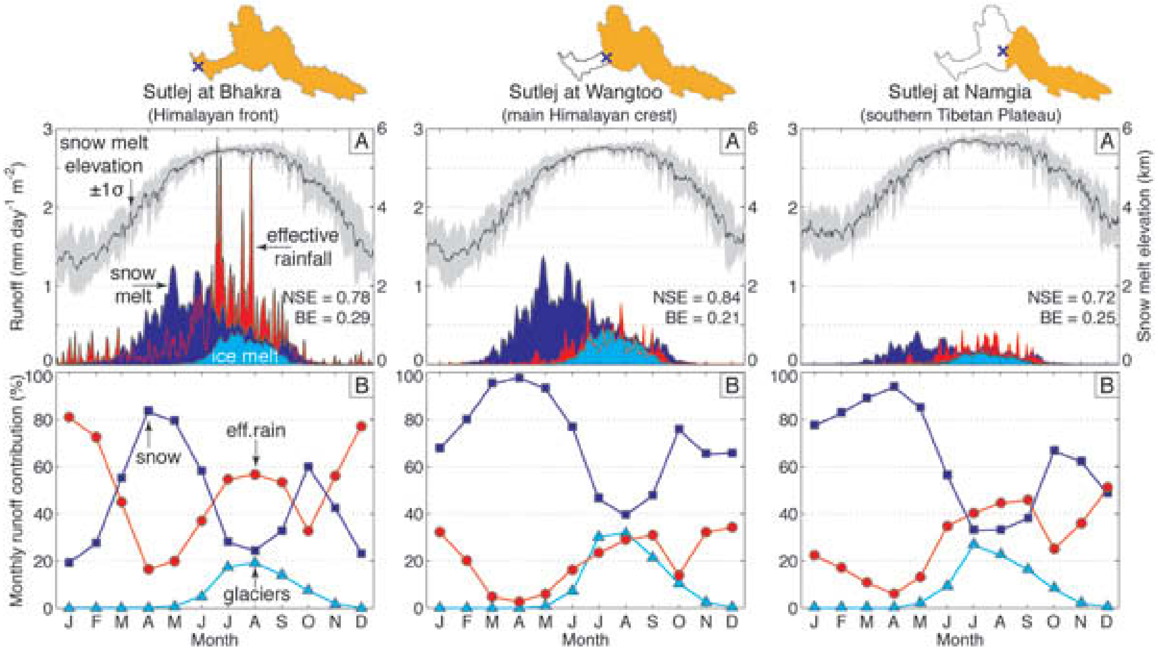

Figure 4.13: Temporal variation of hydrological components. (A) Mean daily runoff of hydrologic components for the Sutlej River (2001-2007) at Bhakra, Wangtoo and Namgia gauging stations (cf. Figure 4.1). Mean catchment-wide snow melt elevation (±1σ) increases to above 5 km asl during the summer months. (B) Monthly percentages to total runoff as shown in A. During the pre-monsoon season (April to June) snow melt dominates river discharge regardless of geographic location. During the monsoon season (July to September) rain, snow and glacial melting have an approximately similar runoff impact at and upstream of the mean Himalayan crest.

We analyze snow melt across the western Himalaya using swath profiles, which show increases in snow melt upstream from about 2 km asl along with increases in elevation and relief (Figure 4.12B). Snow melt is high (>0.5 m) in the region of the main Himalayan crest, from where it decreases towards the Tibetan Plateau. Despite high elevations, this decline is mainly due to an increasing leeward distance from the main orographic barrier and a decrease in topographic relief (Figure 4.12B).

Annual river discharge throughout the Sutlej Valley is characterized by a pronounced seasonal cycle with low flow during winter and peak runoff during summer (Figure 4.13). Snow melt initiates in March and dominates river discharge until June. During that period snow melt migrates to higher elevations, with peak snow melt at elevations of 4.5 to 5.5 km asl. From June to September monsoonal rainfall and glacial melt contribute significantly to river discharge.

4.5.4 Annual variations of hydrological components

The observed Sutlej River discharge at its outlet has a high annual variability, as discharge almost doubles between individual years. If we compare the annual variation of ground-based measurements with simulated runoff of each hydrological component, we find that variations in snow melt ($r^2 = 0.84$) and adjusted TRMM-derived rainfall ($r^2 = 0.78$) are captured well. We also find an inverse correlation ($r^2 = 0.67$) between the observed winter snowfall and the glacial snow-free period during the subsequent summer (Figure 4.14). This variation in the glacial melt duration explains 57% of the glacial melt variation. Thus, winter snowfall on glaciers contributes not only to glacial accumulation but also influences glacial ablation, as prolonged snow cover shields glaciers from radiation influx in the subsequent summer season [*Thayyen et al.*, 2007]. Our modeled annual variations in glacial ablation also agree with ablation stack measurements of the nearby Chhota Shigri glacier, which show significant decrease in glacial melt in 2005 [*Wagnon et al.*, 2007]. In addition, we calculate average glacial ablation rates for the Sutlej Valley based on the glacial melt contribution to river discharge and the glacial surface area (2004 km^2). Glacial ablation in the Sutlej Valley varies considerably between the years 2001 to 2007 with an average ablation rate of 0.93 ± 0.18 m/yr.

4.5.5 Limits and characteristics of the hydrological model

Due to the remoteness and climatic variability of the Sutlej Valley it is difficult to model its hydrology based on the sparse ground-station coverage. Therefore, we based our hydrological model on calibrated remote sensing data, which we validated by all for us available ground station data. Despite our use of remote sensing data with high spatial and temporal resolution, several shortcomings of the input data and the model setup warrant attention when interpreting the results:

First, there exists a trade-off in the TRMM 3B42 precipitation product between high temporal (3 hrs) and low spatial resolution (30 x 30 km^2). Consequently, TRMM 3B42 does not capture the high spatial variability of monsoonal rainfall resulting from small-scale convection. However, the high sampling rate is crucial to detect the occurrence of convective monsoonal rainstorms, which have a relative short lifetime of a half hour to several hours and small spatial footprints of a few to several dozen km^2 [*Barros et al.*, 2006]. Overall, we find that in those areas where rainfall is high (>0.7 m/yr), TRMM 3B42 performs reasonably well compared to the ground based measurements, whereas TRMM performs poor in areas where the importance

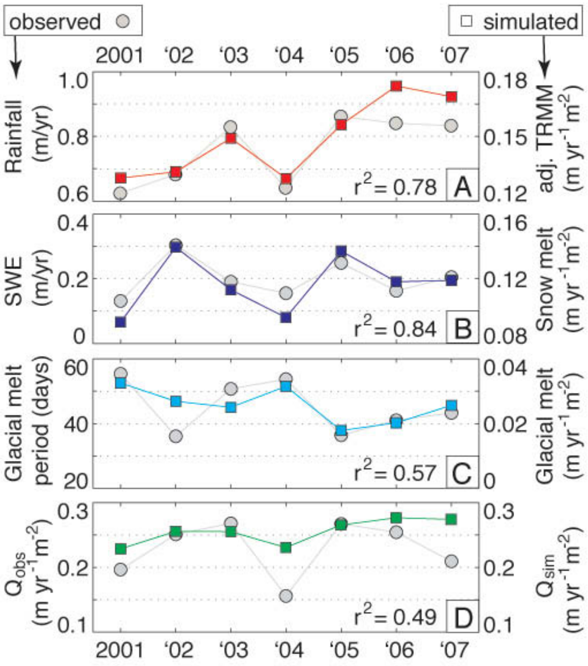

Figure 4.14: Annual variations in observed and simulated hydrological components within the Sutlej Valley. (A) Mean annual rainfall of 23 weather stations versus the mean annual runoff of the adjusted TRMM 3B42 product. (B) Mean annual SWE records of 15 weather stations versus the modeled mean annual snow melt runoff. (C) Mean annual glacial melt period based on MODIS snow-cover data on glaciers versus modeled mean annual glacial melt runoff. (D) Observed river discharge versus modeled river discharge at the Sutlej River outlet (Sutlej at Bhakra).

of rain as compared to snow and ice melt is much lower, which therefore still leads to reasonable model results.

Second, the air temperature data, which drive snow and glacial melt, are based on the average daily atmospheric lapse rate to distribute temperature records from the weather station in Kalpa. We are aware that daily temperature variations at this station may not represent variations within the entire Sutlej Valley [*Blandford et al.*, 2008; *Lundquist and Cayan*, 2007] and that we do not account for spatial variations in the lapse rate [*Minder et al.*, 2010]. However, Kalpa is located central to the most prominent snow and ice reserves in the Sutlej Valley and is thus likely to provide representative average conditions.

Third, a major constrain in most MODIS land products is that they are only available during clear sky conditions, as clouds prevent observations in the visible and thermal infrared spectral ranges. As described in section 4.4.3 we combined Aqua and Terra observations to reduce cloud cover gaps. However, snow and cloud cover are focused predominantly at mountaintops (Figure B.6), which leads to larger interpolation uncertainties during transitions between snow and no-snow cover.

Fourth, our modeling approach is deliberately simple and includes only the key components (snow melt, glacial melt, effective rainfall) to distinguish and quantify each runoff source and to avoid including unknown and difficult to constrain parameters. Therefore, we neglect losses to the ground, sublimation of snow and ice, rain on snow events, areal changes in glacier cover, and transient water storage in soils and vegetation. The latter may be of lower importance in the upstream parts of our study area, because vegetation cover is only pertinent in the lower-elevation regions of the catchment area (Figure 4.2).

Fifth, we use a constant melt factor for snow and ice (equation 4.3.1 and 4.3.1), because our temperature index model accounts for variations in radiation influx and snow properties (e.g., incoming solar radiation, snow albedo). However, our melt factor for snow varies spatially among different catchments as it decreases with increasing mean basin elevation. This is expected as sublimation plays a major role in the heat budget in high-elevated low-latitude regions [*Hock*, 2003; *Sicart et al.*, 2008; *Wagnon et al.*, 1999]. Due to high energy consumption of sublimation, the energy available for melt is reduced and thus lowers the corresponding melt factors [*Lang and Braun*, 1990]. The variation of the melt factor for ice is less pronounced as glaciers are confined to altitudes of similar solar radiation influx.

4.6 Conclusion

In this study, we provide a comprehensive analysis of hydrologic components and their contribution to daily Sutlej River discharge, based on extensive remote-sensing calibration and adjustment procedures. Most notably, we have improved (1) fractional snow cover by filling cloud cover gaps, identifying cloud pixels misclassified as snow, and correcting for viewing angle artifacts, (2) temperature constrains by seasonal lapse rate data based on MODIS nighttime surface temperatures, (3) net radiation balance by incorporating daily fractional cloud cover data, and (4) rainfall estimates based on TRMM 3B42 data, which we validated and adjusted with data from 81 weather stations.

Based on our hydrological modeling study and calibration analysis we identified the following three key aspects:

First, the TRMM 3B42 moderately well depicts rainfall in humid frontal regions of the Himalaya within 10% of the weather station records, whereas it significantly overestimates weather station rainfall by a factor of 2-6 in the orogenic interior. This

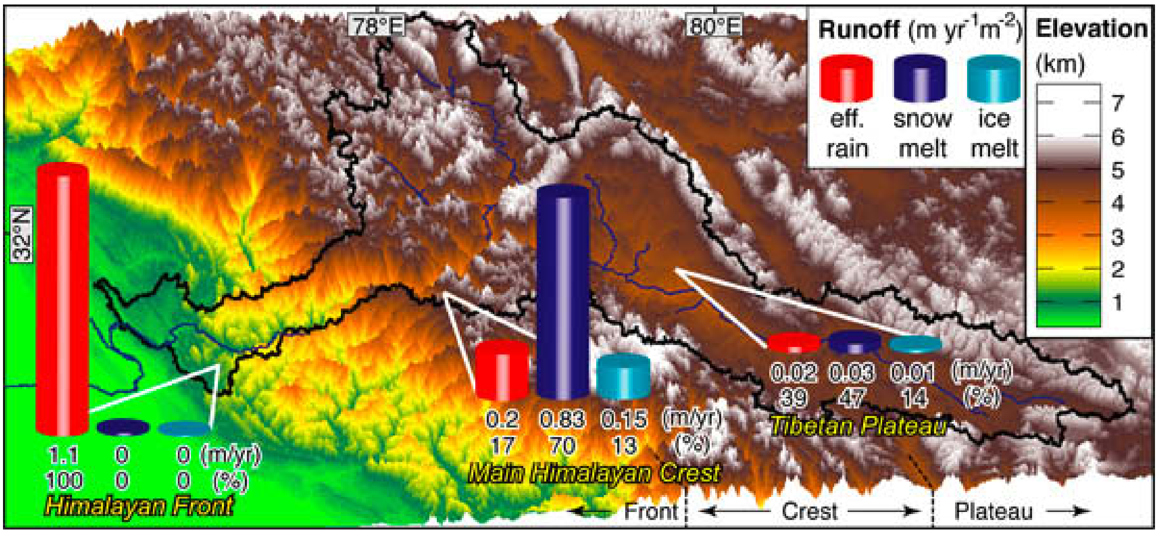

Figure 4.15: Summary figure of spatial variations in hydrological components. 3D oblique view of the Sutlej catchment with 10× exaggerated elevations. We illustrate characteristic changes in mean annual runoff of Sutlej River tributaries along its course from the southern Tibetan Plateau through the main Himalayan crest to the Himalayan front.

bias follows an inverse power-law relationship with mean annual precipitation and suggests that TRMM 3B42 performs low in semi-arid to arid regions of high relief and elevation.

Second, based on our modeling results, the average annual river discharge at the outlet of the Sutlej River is sourced to ∼47% by effective rainfall, ∼43% by snow melt, and ∼10% by glacial melt. The discharge components vary strongly by season with snow melt dominating (74%) the pre-monsoon season (April to June) whereas the summer season from July to September is dominated by rainfall (55%), followed by snow (28%) and glacial melt (17%). Thus, transient water storage in ice and snow is an important source for discharge in the Sutlej River. However, peak discharges and daily variations are usually controlled by rainfall events.

Third, snow and glacial melting in the western Himalaya is highest near the main Himalayan crest, about 100 km inwards from the mountain front (Figure 4.15). Downstream of the main Himalayan crest, rainfall contribution becomes more important during both the winter and summer seasons. Pronounced inter-annual variations in winter snowfall also affect glacial melt, as the snow-cover duration controls radiation influx during the subsequent summer season. Based on our model, the average glacial melt in the Sutlej Valley between 2001 and 2007 has a water equivalent of 0.93±0.18 m/yr.

Under scenarios of future climate change, including higher temperatures, rising snowlines and declining glaciers, the long-term discharge of the Sutlej River is likely to be reduced, especially in the high-elevated internal parts of the orogen. Snow melt runoff may occur earlier in the year and decrease in magnitude while contributions from rainfall and glacial melt may increase on a short- to intermediate-term basis.

Chapter 5

Controls on suspended sediment flux in the Sutlej River Valley, western Himalaya

Abstract

Sediment transport in Himalayan rivers represents active erosion of the orogen, which holds implications for landscape evolution models and hydropower infrastructures. Despite the recent boost in Himalayan hydropower exploitation, little is known about triggers and sources of extreme sediment flux events, which account for extensive reservoir filling and turbine abrasion. Here, we present comprehensive analysis of spatiotemporal trends in suspended sediment flux based on daily data during the past decade from four sites along the Sutlej River and from four of its main tributaries. In conjunction with TRMM (Tropical Rainfall Measurement Mission) 3B42 rainfall data, MODIS (Moderate Resolution Imaging Spectroradiometer) snow cover data, air temperature and earthquake records, and rock strength measurements we infer triggers and causes of peak suspended sediment concentrations (SSC) events, which account for the bulk of the suspended sediment flux in the semi-arid interior of the orogen. Besides occasional floods and glacial sediment discharges, we find that rainstorms coincide frequently (57-63%) with peak SSC events. Overall, there is an increasing trend in suspended sediment flux from the southern Tibetan Plateau to the Himalayan front, which is driven by a 20-fold increase in runoff, despite a 8-fold decrease in SSC towards the main Himalayan crest. This trend indicates, that modern erosion in the western Himalaya is most pronounced at frontal regions, which are characterized by intense monsoonal rainfall and developed soils. The high runoff and low SSC levels at the main Himalayan crest suggest most suitable conditions for small to medium sized hydropower stations in this region.

5.1 Introduction

Pronounced erosion in the Himalaya delivers large amounts of sediment to the Indus and the Ganges-Brahmaputra river systems, which build up the worlds two largest submarine fans in the Arabian Sea (10 km thick) [*Clift et al.*, 2001] and the Bay of Bengal (16.5 km thick) [*Curray et al.*, 2003], respectively. The sediment loads (Indus: 250, Ganges: 520, Brahmaputra: 540 x 10^6 t/yr) rank among the highest in the world and contribute ~10% to the total sediment load reaching the global oceans [*Milliman and Syvitski*, 1992]. Knowledge of the magnitude and distribution of orogenic erosion rates as well as the operating processes is crucial for understanding how these landscapes evolve [*Molnar and England*, 1990; *Small and Anderson*, 1995] and how erosion might affect active tectonics [*Burbank et al.*, 1996; *Wobus et al.*, 2005] and global climatic changes [*Raymo et al.*, 1988; *Raymo and Ruddiman*, 1992]. Furthermore, quantifying the spatiotemporal patterns and variation of fluvial sediment flux is important, because it affects the lifetime of hydropower reservoirs and abrades hydropower turbines [*Singh et al.*, 2003].

High topographic relief, steep river profiles, and elevated stream power indicate high erosion rates throughout the Himalaya [*Finlayson et al.*, 2002; *Vance et al.*, 2003]. Several authors have argued that high erosion rates result from rapid rock uplift and heavy monsoonal precipitation which drives rapid physical erosion along the southern front of the Himalaya [e.g. *Burbank et al.*, 2003; *Galy and France-Lanord*, 2001; *Thiede et al.*, 2004]. Particularly the eastern and western syntaxis are areas of high exhumation and erosion (1-10 mm/yr) [*Burbank et al.*, 1996; *Burg et al.*, 1998; *Stewart et al.*, 2008; *Zeitler et al.*, 2001]. In contrast, on the Tibetan Plateau, erosion rates are significantly lower ($<$0.03 mm/yr), due to lower precipitation and lower relief [*Lal et al.*, 2003].

Long-term ($>10^3$ yr) rates of erosion and models of landscape evolution are typically based on thermochronological [e.g. *Reiners et al.*, 2005] cosmogenic nuclide data [e.g. *Bierman*, 1994; *von Blanckenburg*, 2005]. More direct measurements of sediment yields, spanning years to decades, can be inferred from sediment accumulation rates in reservoirs (sediment trapping), or from measurements of suspended sediment and bedload fluxes in streams (sediment gauging) [*Meade*, 1988]. Although fluvial sediment fluxes often miss out infrequent, high-intensity events and rarely include the bedload fraction, they provide valuable insights into the behavior of rivers and their coupling to weather and climate.

In this study, we analyze daily river discharge and suspended sediment concentration (SSC) data from the Sutlej drainage basin in the northwestern Himalaya. We use data from four sites along the Sutlej River and from four of its main tributaries, to study the sediment flux characteristics in different climatic regions. We compare the sediment flux data with remotely sensed rainfall and snow cover data, as well as air temperature and earthquake records, and rock-strength measurements to investigate their controls on peak SSC events, which often account for the bulk of the sediment budget [*Wulf et al.*, 2010]. We further compare our new data with published sediment flux data from across the Himalaya to identify spatial patterns and first-order controls on sediment transport.

5.2 Study area

The Sutlej River is the largest tributary of the Indus River and drains the third largest catchment area (ca. 55,000 km^2 above 500 m asl) in the Himalaya. Approximately two-thirds of its mountainous catchment area is located in China and drains the Zhada Basin, which stretches along the southern edge of the Tibetan Plateau. To the West, the Indian part of the Sutlej Valley covers a wide range of elevations between the Indo-Gangetic Plains (0.4 km above sea level, asl) and the main Himalayan crest (6.4 km asl) (Figure 5.1). The catchment-average altitude is 4.4 km asl. More than 80% of the catchment area is located at >4 km asl and has virtually no vegetation cover (Figure 5.1A). The lower part of the catchment area (<4 km asl) is located at the monsoon-impacted southern front of the Himalaya, where vegetation is lush and dense.

Therefore the primary land cover in the Sutlej Valley is bare ground (81.2%), next to trees and shrubs (7.2%), cultivated areas (6.8%), glaciers (3.7%), and lakes (1.1%) [*FAO*, 2009]. This indicates that developed soils cover a small fraction (<15%) in the lower part of the Sutlej Valley. Glacial cover is particularly dense at the main Himalayan crest, which represents the region of highest snowfall [*Singh and Kumar*, 1997]. As a result, river runoff from the high, rainfall-shielded interior part of the Sutlej Valley is comparable in magnitude to the Himalayan front, which is dominated by monsoonal rainfall [*Wulf et al.*, in review].

Precipitation in the western Himalaya has pronounced seasonal and spatial variations [*Bookhagen and Burbank*, 2010]. Most snowfall occurs between December and March and increases with elevation [*Singh and Kumar*, 1997; *Winiger et al.*, 2005]. From mid-July to mid-September the Indian monsoon accounts for intense rainfall,

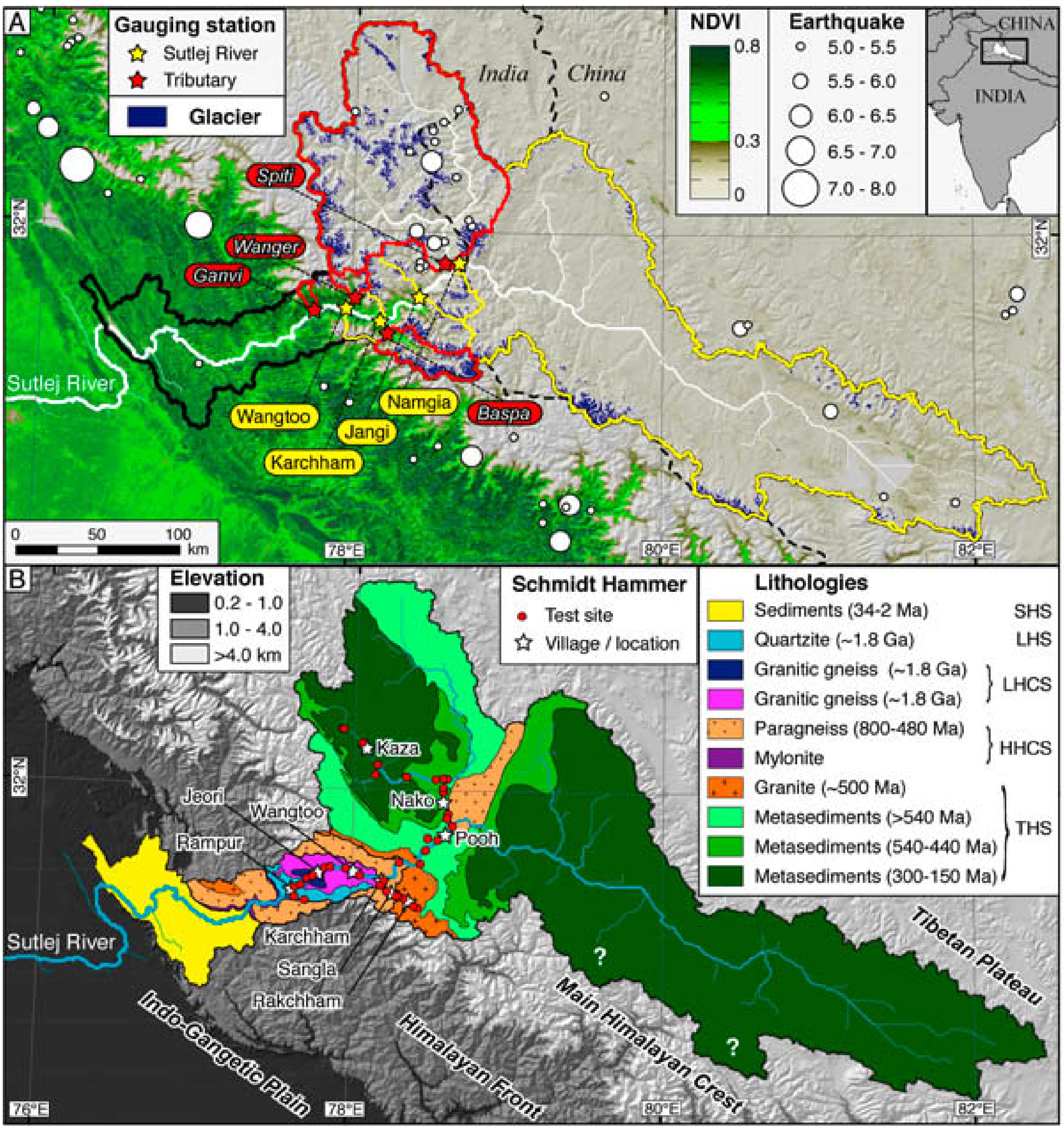

Figure 5.1: Overview of the studied catchments, vegetation cover, and lithologies. (A) Map of the normalized difference vegetation index (NDVI) [*Huete et al.*, 2002] in the study area overlain by glaciers and earthquake locations, scaled by their magnitude (http://www.iris.washington.edu) (Table C.1). Gauging stations indicate locations of river discharge and SSC measurements. The corresponding upstream areas of Sutlej River tributaries and watersheds are indicated in red and yellow, respectively. (B) Shaded-relief and elevation map of the western Himalaya overlain by lithologies and Schmidt Hammer test site in the Sutlej Valley. Lithologies are grouped into the Sub-Himalaya Sequence (SHS), Lesser Himalayan Sequence (LHS), Lesser Himalayan Crystalline Sequence (LHCS), Higher Himalayan Crystalline Sequence (HHCS), and Tethyan Himalayan Sequence (THS).

Table 5.1: Topographic, climatic and hydrological characteristics of the studied watersheds. Locations of the catchments are indicated in Figure 5.1.

	Catchments	Topography				Climate				Hydrology				
		Area	*Elevation*		*Relief*	*Ice*	*Snow*	*Rain*	*Vegetation*	*Runoff*		*Sediment Concentration*		*Sediment yield*
		(km^2)	min (km)	max (km)	(km/ 5 km)	area (%)	area (%)	TRMM (m/yr)	NDVI	(m/yr)	summer (%)	(g/l)	summer (%)	(t km^{-2} yr^{-1})
Tributaries	Ganvi	117	1.6	5.6	2.58	3.7	25.8	1.12	0.39	1.27	78.3	0.93	-	1507
	Wanger	264	2.5	5.7	2.24	17.2	54.1	0.74	0.11	1.67	85.4	0.29	-	614
	Baspa	989	2.5	6.4	2.21	24.0	54.0	0.93	0.09	1.14	89.5	0.80	96.5	1717
	Spiti	12,477	2.6	6.7	1.68	6.7	37.4	0.36	0.03	0.26	86.9	1.45	-	499
Watersheds	Sutlej at Namgia	30,950	2.6	7.2	0.93	1.8	19.8	0.38	0.08	0.06	85.1	2.59	-	223
	Sutlej at Jangi	44,738	2.2	7.2	1.21	3.6	25.6	0.39	0.07	0.13	81.5	1.85	-	302
	Sutlej at Karchham	46,291	1.9	7.2	1.22	3.6	25.7	0.39	0.07	0.16	85.3	2.37	-	556
	Sutlej at Wangtoo	48,316	1.5	7.2	1.27	4.1	26.5	0.41	0.07	0.20	85.9	2.20	91.6	615

which is focused at elevations of 0.9 ± 0.4 km and 2.1 ± 0.3 km asl at the southern Himalayan front [*Bookhagen and Burbank*, 2006]. The Higher Himalaya acts as an orographic barrier that inhibits most monsoonal moisture to migrate northward into the orogen and therefore creates a steep orographic rainfall gradient. Rainfall decreases from >2 m at the fontal parts to <0.2 m in the interior parts of the orogen over a horizontal distance of <100 km [*Wulf et al.*, 2010]. Several studies suggest that during active monsoon phases strong convective cells can migrate across this orographic barrier and result in heavy rainfall events, which can mobilize enormous amounts of sediments in the orogen's interior [*Bookhagen et al.*, 2005a; *Craddock et al.*, 2007; *Wulf et al.*, 2010].

The continuous northeastward movement of India with respect to Eurasia at a present rate of ca. 35mm/yr [*Larson et al.*, 1999] causes considerable seismic activity in the Himalaya [*Bilham et al.*, 2001]. During the past century, 20 earthquakes with magnitude ≥5 occurred in the Sutlej Valley (Figure 5.1A).

The lithology in the study area can be subdivided into several contrasting units, which are bounded by major north-dipping tectonic faults systems that run parallel along strike the mountain belt [e.g. *Burchfiel et al.*, 1992; *Fuchs*, 1975; *Gansser*, 1964; *Heim and Gansser*, 1939; *Hodges*, 2000]. From southwest to northeast these units comprise (a) the Sub-Himalaya foreland basin, which contains detrital sediments derived from erosion of the orogen [*Vannay et al.*, 2004]; (b) the Lesser Himalaya Sequence (LHS), which mainly consists of massive quartz-arenites intruded by basalts [*Miller et al.*, 2000]; (c) the medium- to high-grade metamorphic sequence of the Lesser Himalayan Crystalline Sequence (LHCS), which consists of mylonitic micaschist, granitic gneiss with minor metabasite and quartzite [*Vannay and Grasemann*, 1998]; (d) the Higher Himalaya Crystalline Sequence (HHCS), which is composed of amphibolite facies to migmatitic paragneisses, with minor metabasites, calc-silicate gneisses, and granitic gneisses often intruded by granitic plutons [*Vannay and Grasemann*, 1998]; and (e) the weakly metamorphosed sediments of the Tethyan Himalayan Sequence (THS), which consists of metapelites and metapsammites that comprise the former Indian continental margin [*Vannay et al.*, 2004].

Throughout this study we distinguish between the Himalayan Front, the main Himalayan crest, and the Tibetan Plateau region based on topographic and climatic characteristics (Figure 5.1B). The Himalayan Front marks the area between the Indo-Gangetic Plains and the peaks of the Higher Himalaya, which is characterized by high monsoonal rainfall and dense vegetation at elevations <4 km. The first of our study areas, the Ganvi catchment, is part of this region, although somewhat set back into the orogen due to the broad and deeply incised Sutlej Valley. The main Himalayan crest region comprises the peaks of the Higher Himalaya and leeward areas that are characterized by high relief, intense snowfall, high degree of glaciation, and sparse vegetation. The Baspa, Wanger, and southern part of the Spiti catchments belong to this region. High elevations, low relief and almost no vegetation due to arid climatic conditions characterize the Tibetan Plateau region. Northern parts of the Spiti catchment and the Sutlej catchment upstream of Namgia (i.e., the Zhada basin) comprise this region.

5.3 Data sets and methods

In the Indian part of the Sutlej Valley, several hydropower companies operate a dense network of river gauging stations, which measure river discharge and suspended sediment concentrations (SSC) twice daily. River discharge measurements are based on stage-discharge rating curves, which are annually recalculated during low flow conditions in winter, because of channel bed changes. Year-round SSC sampling of the Sutlej River and its tributaries is done at the surface of the water column and close to the riverbank, because of highly dynamic and rapid flow conditions. Given the high turbulence of the streams, we assume a high degree of sediment mixing. In our analysis, river discharge and SSC data represent the daily average of usually two measurements, one in the early morning and one during late afternoon. In the Baspa River and the Sutlej River at Wangtoo measurements are conducted on a 6-hourly and hourly basis, respectively.

To assess the consistency of the individual discharge and SSC measurements we cross correlate all gauging sites (Table 5.2). As expected, we find strong correlations

Table 5.2: Consistency check of river discharge and SSC measurements. Number of coinciding daily measurements (lower left) of river discharge (top) and suspended sediment concentration (bottom) and their correlation among different gauging sites (upper right, marked italic). Neighboring stations along the Sutlej, which are expected to correlate strongly, are marked bold.

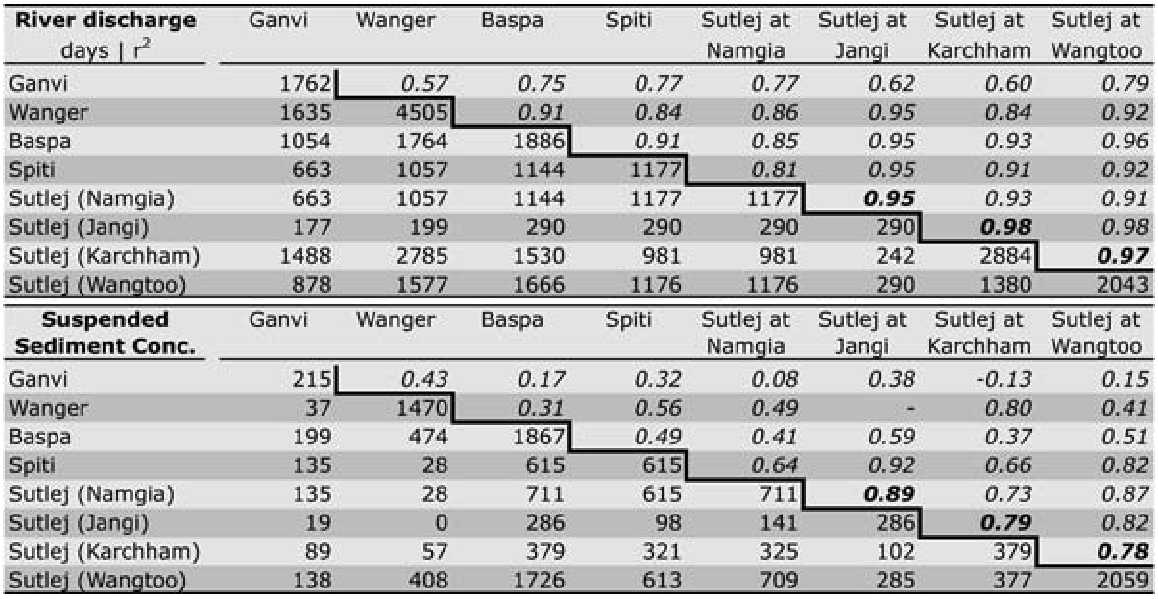

River discharge days | r^2	Ganvi	Wanger	Baspa	Spiti	Sutlej at Namgia	Sutlej at Jangi	Sutlej at Karchham	Sutlej at Wangtoo
Ganvi	1762	*0.57*	*0.75*	*0.77*	*0.77*	*0.62*	*0.60*	*0.79*
Wanger	1635	4505	*0.91*	*0.84*	*0.86*	*0.95*	*0.84*	*0.92*
Baspa	1054	1764	1886	*0.91*	*0.85*	*0.95*	*0.93*	*0.96*
Spiti	663	1057	1144	1177	*0.81*	*0.95*	*0.91*	*0.92*
Sutlej (Namgia)	663	1057	1144	1177	1177	***0.95***	*0.93*	*0.91*
Sutlej (Jangi)	177	199	290	290	290	290	***0.98***	*0.98*
Sutlej (Karchham)	1488	2785	1530	981	981	242	2884	***0.97***
Sutlej (Wangtoo)	878	1577	1666	1176	1176	290	1380	2043

Suspended Sediment Conc.	Ganvi	Wanger	Baspa	Spiti	Sutlej at Namgia	Sutlej at Jangi	Sutlej at Karchham	Sutlej at Wangtoo
Ganvi	215	*0.43*	*0.17*	*0.32*	*0.08*	*0.38*	*-0.13*	*0.15*
Wanger	37	1470	*0.31*	*0.56*	*0.49*	-	*0.80*	*0.41*
Baspa	199	474	1867	*0.49*	*0.41*	0.59	*0.37*	*0.51*
Spiti	135	28	615	615	*0.64*	0.92	*0.66*	*0.82*
Sutlej (Namgia)	135	28	711	615	711	***0.89***	*0.73*	*0.87*
Sutlej (Jangi)	19	0	286	98	141	286	***0.79***	*0.82*
Sutlej (Karchham)	89	57	379	321	325	102	379	***0.78***
Sutlej (Wangtoo)	138	408	1726	613	709	285	377	2059

in river discharge between neighboring measurement sites along the Sutlej River and the weakest correlations to the smallest, most rain fed Ganvi catchment.

We use the data on daily river discharge, Q (m^3/s), and suspended sediment concentration, SSC (g/l), to calculate the suspended sediment load [SSL] (t yr^{-1}) and the suspended sediment yield [SSY] (t km^{-2} yr^{-1}) according to:

$$SSL = cf \cdot \sum_{i=1}^{365} \left(Q\left(i\right) \cdot SSC\left(i\right) \right) \tag{5.1}$$

$$SSY = SSL/A \tag{5.2}$$

where A is the catchment area (km^2) and cf is a non-dimensional conversion factor of 86.4 to account for the conversion of measurement units. We convert daily river discharge (m^3/s) to part of the annual runoff (m/yr) according to:

$$runoff = \frac{cf \cdot \sum_{i=1}^{365} \left(Q\left(i\right) \right)}{1000 \cdot A} \tag{5.3}$$

To investigate links between peak SSC events and rainstorms we use the TRMM product 3B42, which has a spatial resolution of 0.25° x 0.25° (∼30 km x 30 km) and a temporal resolution of 3 h. This data set combines microwave and infrared rain-rate estimates from sensors onboard several low-earth orbit and one geosynchronous satellite, which are rescaled to monthly rain-gauge data [*Huffman et al.*, 2007]. Although the spatial resolution of the TRMM 3B42 data makes direct comparison to weather station data difficult, *Wulf et al.* [in review] found that annually summed TRMM 3B42 data appears to overestimate rainfall in semi-arid regions of the Himalaya by a factor of 2-6. This discrepancy is most likely due to confusion of snow and rainfall during winter (November-April), whereas in this study, we focus on the monsoonal period (June-September) during summer. We define rainstorms as rain events exceeding 10 mm/day, peak SSC days as days exceeding the 99th SSC percentile, and peak SSC events as the period that encompasses the increase and decrease of SSC before and after a peak SSC day, respectively.

We further use daily fractional snow cover (FSC) observations that are derived from the MODIS instrument onboard the Terra and Aqua satellites of the NASA Earth Observation System [*Hall et al.*, 2002, 1995] to study the impact of snow and glacial melt sediment discharges. Comparison of MODIS snow products with ground-based snow measurements in the western US and Austria have yielded accuracies of 94-95% [*Klein and Barnett*, 2003; *Parajka and Blöschl*, 2006]. Further information on data processing and interpolation to eliminate artifacts and fill data gaps due to clouds and are presented by [*Wulf et al.*, in review].

In order to obtain information on spatial variations in rock strength, rock compressive strength was estimated with a Schmidt Hammer on fresh bedrock surfaces at steep cliff faces of road cuts [*Katz et al.*, 2000]. We conducted measurements in the Spiti, Sutlej, and Baspa valley, which cover different rock types that are characteristic for the entire Sutlej Valley (Figure 5.1C). Individual measurements returning rebound values <10 R probably indicate fractured rock and were discarded [*Craddock et al.*, 2007]. Consequently we did not measure weak, but intact rocks with this method. At each site, 10 to 40 measurements were made at 20-cm intervals.

5.4 Results and Discussion

5.4.1 Peak suspended sediment concentration events

Rainstorms, floods, and glacial discharges are related to peak SSC events and account for the bulk of the suspended sediment flux. In all catchments leeward of the main orographic barrier the 90th SSC percentile accounts for more than 50% of the total suspended sediment flux (Figure 5.2).

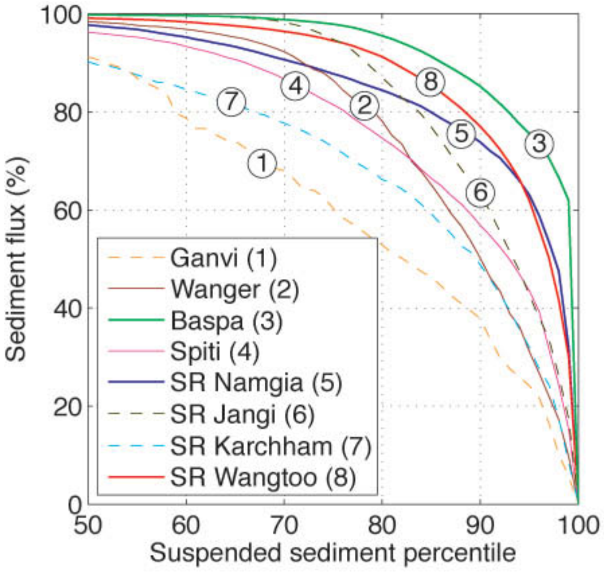

Figure 5.2: Percentage of peak SSC events on total suspended sediment flux. Dashed lines indicate gauging stations that cover less than one year.

Influence of Rainstorms

We find that rainstorms frequently coincide with peak-SSC events in the discharge of the Sutlej River and tributaries (Figure 5.3). Rainstorms typically occur during the monsoon season from June to September (Figure 5.4) and last for 1-3 days [*Wulf et al.*, 2010]. Our most complete SSC time series, which cover five to seven years of the Wanger and Baspa rivers and the Sutlej River at Wangtoo, indicate that 57-63% of all peak-SSC events are directly related to rainstorms (Table 5.3). Rainstorm related peak-SSC events occur almost annually in the semi-arid orogenic interior and account for 40% of the total suspended sediment flux of the Sutlej River at Wangtoo.

During a field visit in September 2009 (Figure 5.3A), we witnessed an intense rainstorm event that triggered widespread rockfalls, debrisflows, and mudflows, in the semi-arid region leeward of the main orographic barrier. The correlation of rainstorms and peak SSC events suggests that rainstorms frequently trigger landslides and enhance fluvial erosion due to increased river discharge.

Whereas the most intense rainstorms are generally associated with peak SSC events (Figure 5.4), numerous rainstorms leave no significant imprint on the SSC record. This effect may be related to the sediment availability, rainstorm location and intensity, or soil moisture thresholds as identified in other parts of the Himalaya [*Crozier*, 1999; *Gabet et al.*, 2004]. The frequent recurrence of peak SSC events during rainstorms in July and August could also indicate that rainfall induced runoff

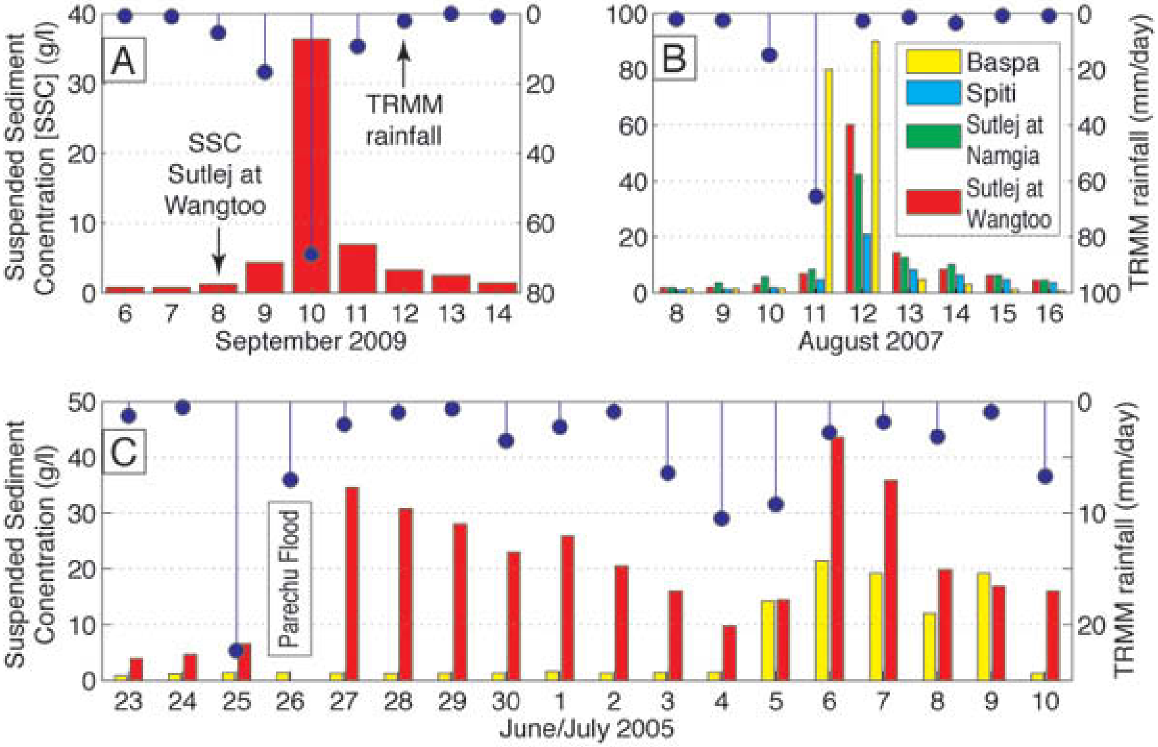

Figure 5.3: Relation between rainfall and peak SSC events. Rainfall indicates TRMM 3B42 derived daily rainfall rates of the Sutlej Valley at Wangtoo. SSC color-coding is indicated in panel B. (A) Peak SSC event triggered by a 3-day rainstorm. (B) Peak SSC event caused by a synoptic rainstorm affecting several catchments in the Sutlej Valley. Larger catchments show longer response times. (C) SSC response of the Sutlej River at Wangtoo to the Parechu flood and a successive rainstorm, which especially affected SSC levels in the Baspa River.

Table 5.3: Peak SSC days, sediment flux, and rainstorms. Total days indicate the number of combined daily river discharge and suspended sediment concentration days. The column "% total SSL" indicates the percentage of peak SSC days on the total SSL budget. Peak SSC events combine successive peak SSC days.

	River	*Total days*	*Peak SSC days (>99th SSC percentile)*					*Peak SSC events*	*Events caused by rainstorms*	
			days	99^{th} SSC percentile	mean SSY	combined SSL	% total SSL			
		(#)	(#)	(g/l)	(t km^{-2} day^{-1})	(10^3 t)	(%)	(#)	(#)	(%)
Tributaries	Ganvi	106	1	5.5	58.89	6.9	5.6	1	1	100
	Wanger	1470	15	1.3	20.49	81.0	9.8	5	3	60
	Baspa	1825	18	2.1	269.58	4799.8	61.9	7	4	57
	Spiti	615	6	8.1	32.20	2410.3	15.3	2	1	50
Main stem	SR Namgia	711	7	19.2	30.28	6560.3	32.0	4	3	75
	SR Jangi	286	3	7.8	13.08	1755.4	17.5	1	1	100
	SR Karchham	287	3	11.7	22.57	3134.0	8.6	2	1	50
	SR Wangtoo	1996	20	14.4	54.04	52221.9	30.1	8	5	63

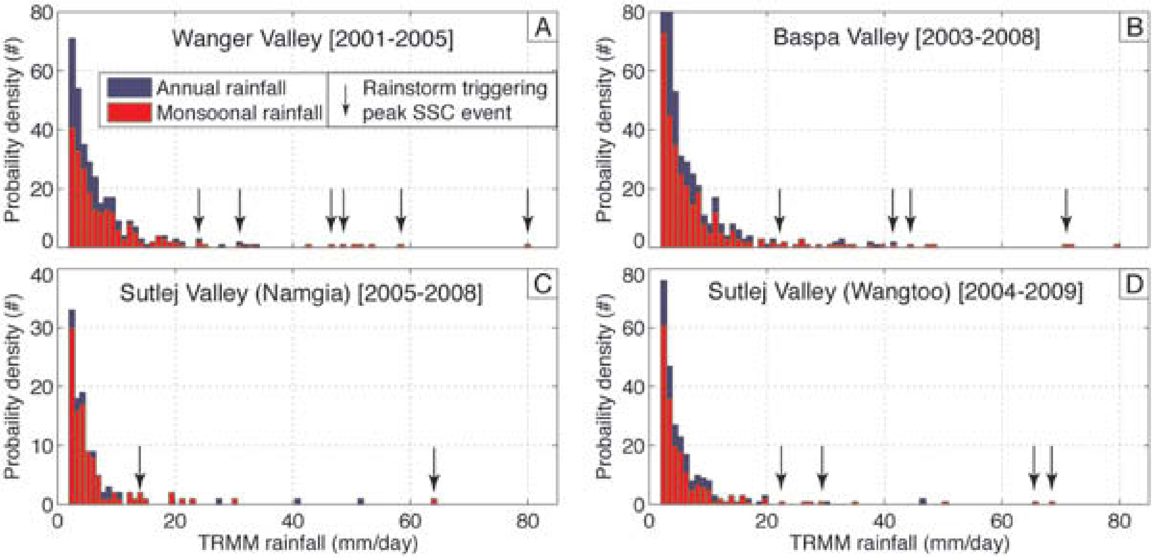

Figure 5.4: Rainstorms triggering peak SSC events. Histograms of daily TRMM 3B42 data displaying annual and monsoonal (June-September) rainfall during the given time-period. Arrows indicate rainstorms (≥10 mm/day), which are associated with peak SSC events.

in glacial areas represents an important sediment source [*Haritashya et al.*, 2006; *Singh et al.*, 2003].

Influence of floods

Besides rainstorms triggering landslides, floods are also associated with peak sediment flux, as they efficiently erode and transport sediment storage in the riverbed [*Baker and Kale*, 1998; *Bookhagen et al.*, 2005a; *Coppus and Imeson*, 2002; *Hartshorn et al.*, 2002]. On June 26th, 2005 a flood occurred in the Parechu River, the main tributary of the Spiti River, which was caused by the failure of a landslide dam that blocked the river. The landslide occurred in late spring/early summer of 2004 and formed an artificial lake, which covered in September 2004 an area of 1.9 km^2 with a maximum depth of about 40 m storing about 64 x 10^6 m^3 of water [*Gupta and Sah*, 2007]. The dam failure released a flood wave of about 20 m in height with a maximum discharge of about 2000 m^3/s estimated at the confluence with the Sutlej [*Gupta and Sah*, 2007]. Farther downstream the peak suspended sediment concentration of the Sutlej River at Wangtoo was measured to be 151 g/l [*SJVNL*, 2005] with an estimated peak discharge of 4000 m^3/s [*Kumar et al.*, 2007a]. The day preceding the flood, the TRMM data indicated heavy rainfall of 10-20 mm/day in semi-arid areas upstream of the landslide, and coincided with pronounced snow melt as indicated by MODIS imagery between the 23rd and 27th of June 2005. During the 5-day period, snow cover in the upstream area (5294 km^2) reduced by 52.3% from 830.1 km^2 (15.7 %) to 395.8 km^2 (7.5%). Therefore, it is likely that the dam failure was caused by a rain-on-snow event, which caused an increase in river discharge and hydrostatic pressure on the dam.

We estimate the suspended sediment load of the flood event (26.06 - 04.07.2005) at the Sutlej River at Wangtoo to be about 35 x 10^6 t, which equates to 80 t km^{-2} day^{-1} or 41% of the 2005 suspended sediment budget. This conservative estimate is based on an average daily discharge of 2000 m^3/s and a SSC of 50 g/l for the flooding day, when no measurements are available (Figure 5.3C).

Influence of glacial runoff

SSC measurements of proglacial streams in the western Himalaya and Karakorum are characterized by high suspended sediment yields [*Collins and Hasnain*, 1995; *Haritashya et al.*, 2006], underlining glaciers as important sediment sources. Based on temperature data and remote sensing imagery, we investigate the glaciers relation to peak SSC events. Such a peak SSC event occurred in the Spiti River during June 2008 in the absence of major earthquakes (Table C.1) or rainstorms (Figure 5.5A). Instead, the increase in SSC from early to mid June corresponds closely to an increase in air temperature. Despite the occurrence of intense rainfall events during mid and late June, the SSC decreased, which again corresponds to decreases in air temperature (Figure 5.5A). This correlation indicates that the flux of suspended sediment during this event was driven by changes in temperature, which suggests a snow- or glacial melt related source for the sediment discharge. During the initiation of this peak SSC event, snow covers less than 15% of the Spiti catchment and decreases moderately during the peak sediment discharge from 14.2 to 8.8% (Figure 5.5B). Therefore, it is unlikely that snow avalanches mobilized large amounts of sediment. In contrast, glacial ablation initiates, as the snowline retreats to glacial elevations, which generally corresponds to the discharge of subglacial sediment [e.g. *Haritashya et al.*, 2006]. Therefore, we conclude that glacial sediment discharge most likely accounts for this peak SSC event. For the measurement period from 23.04 to 29.08.2008 this peak SSC event (3-29 June) accounted for 58% of the total suspended sediment flux, corresponding to 3.1 x 10^6 tones suspended sediment load.

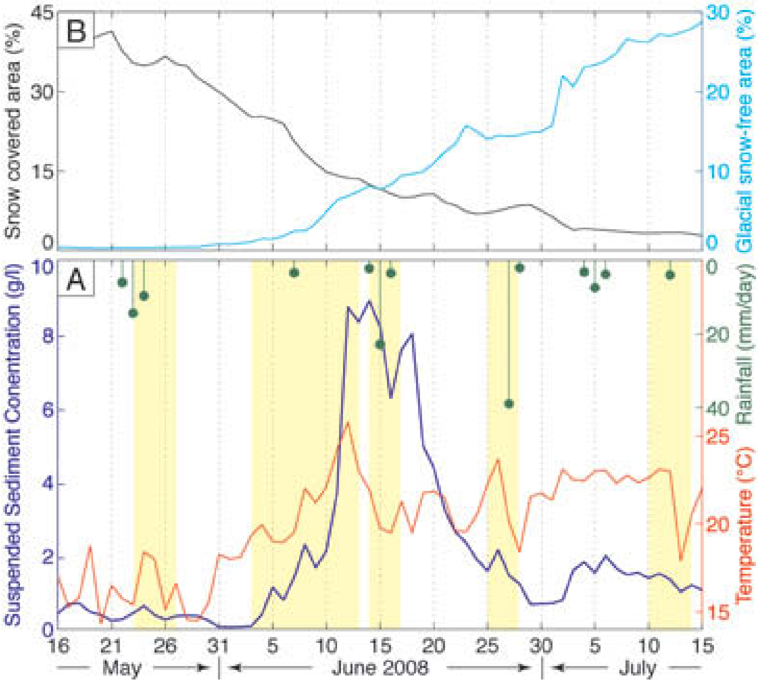

Figure 5.5: Peak SSC event related to glacial discharge. (A) Comparison of SSC in the Spiti River with TRMM 3B42 rainfall in the Spiti catchment and mean daily air temperature data from Namgia (cf. Figure 5.1A) during a two-month period in 2008. Yellow background indicates periods of corresponding periods of SSC and temperature variations. (B) Percentage of snow covered area and the percentage of glacial snow-free area in the Spiti catchment for the same period.

5.4.2 Hysteresis loops

In all catchments we find a strong correlation between daily river discharge and daily SSC (Figure 5.6). Peak SSC days are characterized by large residuals from the sediment rating curve and occur predominantly along with high river discharge during June to August in the Baspa, Spiti, and Sutlej Valley at Namgia.

We hypothesize, that this accumulation in peak SSC events in these catchments may be related to the occurrence large sedimentary fans, which cluster especially in glaciated areas of Tethyan sedimentary rocks (cf. Figure 5.1B). The strong correlation between river discharge and SSC suggests increased reworking of sediment storage in the riverbed as the river discharge increases.

In most catchments we find a weakly pronounced anticlockwise hysteresis loop as represented for the Sutlej River watershed at Wangtoo (Figure 5.7A). This anticlockwise hysteresis loop is most pronounced in the Wanger River (Figure 5.7B) and indicates less suspended sediment transport on the rising limb of the hydrograph (May, June) than on the falling limb (September, October) for a given discharge.

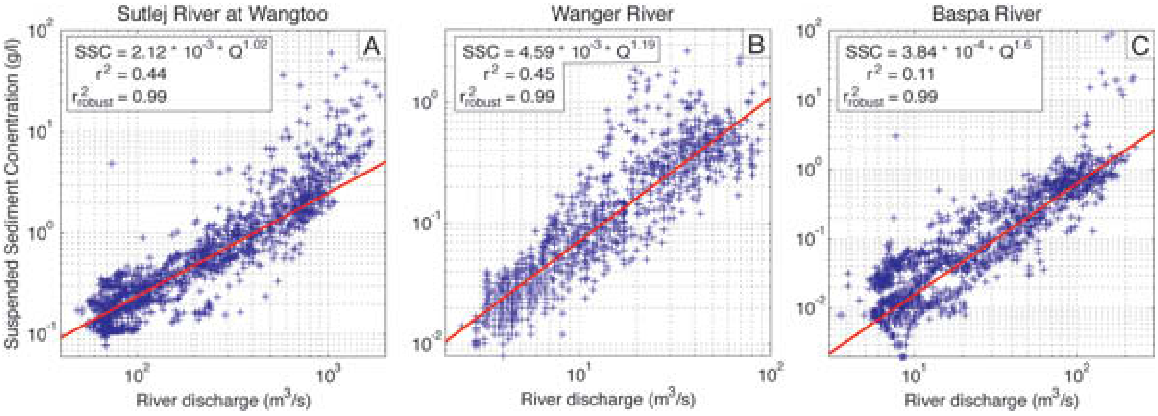

Figure 5.6: Sediment rating curve of the Sutlej River at Wangtoo, Wanger River, and Baspa River showing suspended sediment concentration (SSC) as a function of daily river discharge (Q). Note that the rating curve in A and C underestimates sediment flux, as it does not capture the peak SSC events adequately.

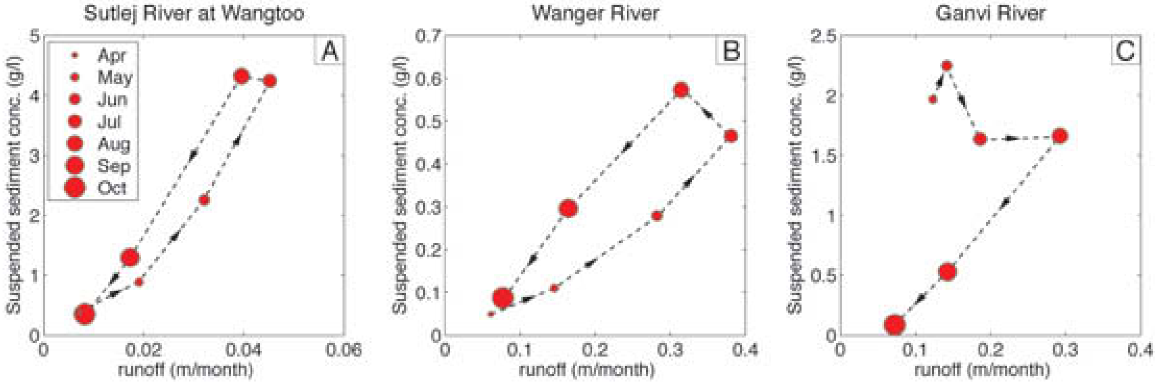

Figure 5.7: Hysteresis loops of the suspended sediment flux in the Sutlej River at Wangtoo, Wanger River, and Ganvi River.

In contrast, the Ganvi River is characterized by a clockwise hysteresis loop (Figure 5.7C), which needs to be interpreted with caution, as it is only based on two summer season records.

Possibly, the clockwise hysteresis effect in the Ganvi River is related to the increased reworking of readily available sediment during the onset of the monsoonal rainfall period in June. The weakly pronounced anticlockwise hysteresis pattern in the remaining catchments indicates higher SSC during late summer, which suggests a higher sediment contribution by glaciers. In a previous study, where we modeled the discharge of the Sutlej River, we found that peak glacial discharge occurs during August [*Wulf et al.*, in review]. This underlines the need to differentiate between frontal and internal regions of the Himalaya, which are characterized by different sediment sources, i.e. soils versus glacially derived sediments (Figure 5.1A).

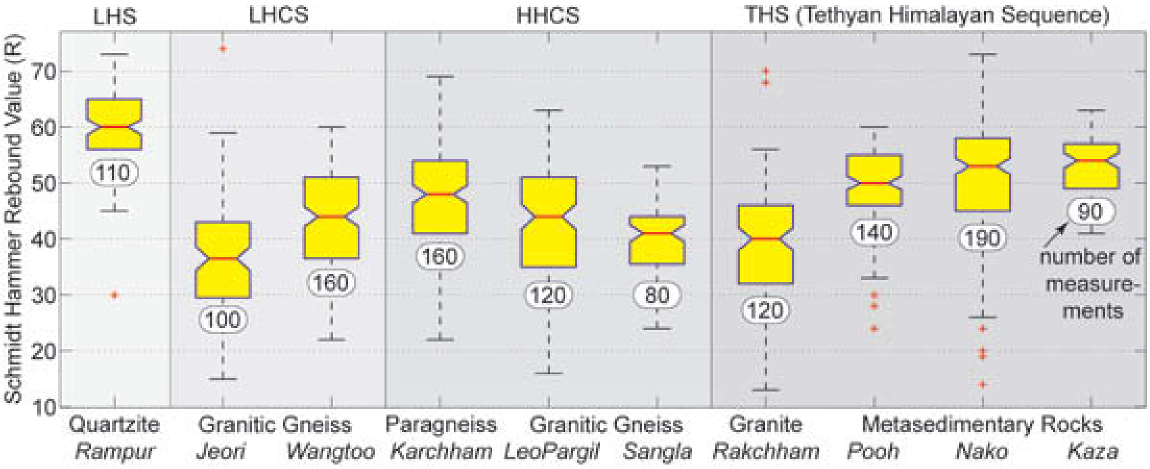

Figure 5.8: Rock strenght of Schmidt Hammer tests. Boxplots of Schmidt Hammer rebound values of different rock types in parts of the Lesser Himalayan Sequence (LHS), Lesser Himalayan Crystalline Sequence, High Himalayan Crystalline Sequence, and Tethyan Himalaya Sequence. Italic letters indicate the approximate location or lithostratigraphic group of each rock type (cf. Figure 5.1B).

5.4.3 Rock strength

Rock strength measurements of all studied rock types vary widely, such that the average standard deviation of the measurements for each rock type is 8.5 R (Schmidt hammer rebound values). Despite such variability, the average rock strength indicates some principle differences between rock types. The quartzite in the Lesser Himalayan Sequence is characterized by the highest rock strength (60.0 ± 6.6 R), whereas the granitic gneisses in the Lesser Himalayan Crystalline Sequence and the High Himalayan Crystalline Sequence indicate significantly lower rock strengths (40.7 ± 9.3 R), similar to the granitic intrusion in the Tethyan Himalayan Sequence (39.4 ± 10.3). Surprisingly, metasedimentary rocks of the Tethyan Himalayan Sequence yield, on average, a high rock strength (51.0 ± 7.6), which exceeds the rock strength of the paragneisses in the High Himalayan Crystalline Sequence (47.1 ± 8.7) (Figure 5.8). However, it should be noted that the metasedimentary rocks are characterized by a high joint density oriented along the foliation, which greatly reduces the cohesive strength of this rock type [*Selby*, 1980]. The large variability in rock strength measurements is mainly influenced by grain size, joint spacing, and sample numbers [*Aydin and Basu*, 2005].

5.4.4 Suspended sediment concentrations and yields

The mean annual suspended sediment concentration (SSC) shows a decreasing trend downstream along the Sutlej River from the Tibetan Plateau to the main Himalayan crest, followed by an increase towards the Himalayan front (Figure 5.9A). In contrast to the 8-fold decrease in mean annual SSC from the Tibetan Plateau to the main Himalayan crest, runoff increases by a factor of 20 (Table 5.1) and therefore, mean annual suspended sediment yields (SSY) (eq. 5.1) continuously increase (Figure 5.9A). Despite the high SSC levels at the Tibetan Plateau, low runoff in this arid region results in a comparably low suspended sediment yield (ca. 250 t km^{-2} yr^{-1}). In contrast, the main Himalayan crest is characterized by high runoff along with low SSC, which results in increased levels of mean annual SSY (ca. 1000 t km^{-2} yr^{-1}), as the increase in runoff exceeds the decrease in SSC. At the main Himalayan front runoff remains high, due to pronounced monsoonal precipitation along with high levels of SSC, which result in high SSY (ca. 1500 t km^{-2} yr^{-1}).

In the Tibetan Plateau region large-scale sediment fans characterize the hillslopes, which indicate high sediment supply, which is easily mobilize by increased river discharge or rainstorms. Despite the high rock strength of metasedimentary rocks at the Tibetan Plateau, we argue that glacial and periglacial processes are highly efficient to erode these layered and densely fractured rocks [*Heimsath and McGlynn*, 2008; *Molnar et al.*, 2007]. The decrease in mean annual SSC towards the main Himalayan crest region is primarily driven by an increase in snow and glacial melt [*Wulf et al.*, in review], which dilutes the suspended sediment concentration. This increase in runoff involves an increase in transport capacity, which might explain the increase in net erosion given the reduced rock strength at the Higher Himalaya with respect to the Tethyan Himalaya (Figure 5.8). The high SSC in the Himalayan front region correlates with an increase in soil cover, which is commonly detached by rain splash, creep, bioturbation, and shallow landsliding [*Burbank*, 2009; *Morgan*, 2004]. Despite the increase in protective vegetation cover, impulsive river discharge and surface runoff caused by frequent rainstorms might be efficient processes to detach soil cover.

5.4.5 Modern Himalayan erosion

Despite the difficulties in comparing different time spans of suspended sediment yields, the long-term mean of the suspended sediment flux in Himalayan rivers indicates some first-order trends and spatial patterns.

Table 5.4: Suspended sediment flux in Himalayan rivers. We first list tributaries followed by their corresponding main stem, shifting geographically from west to east. The catchment denudation rate is based on an average rock density of 2.65 g/cm^3 and accounts only for the suspended sediment flux.

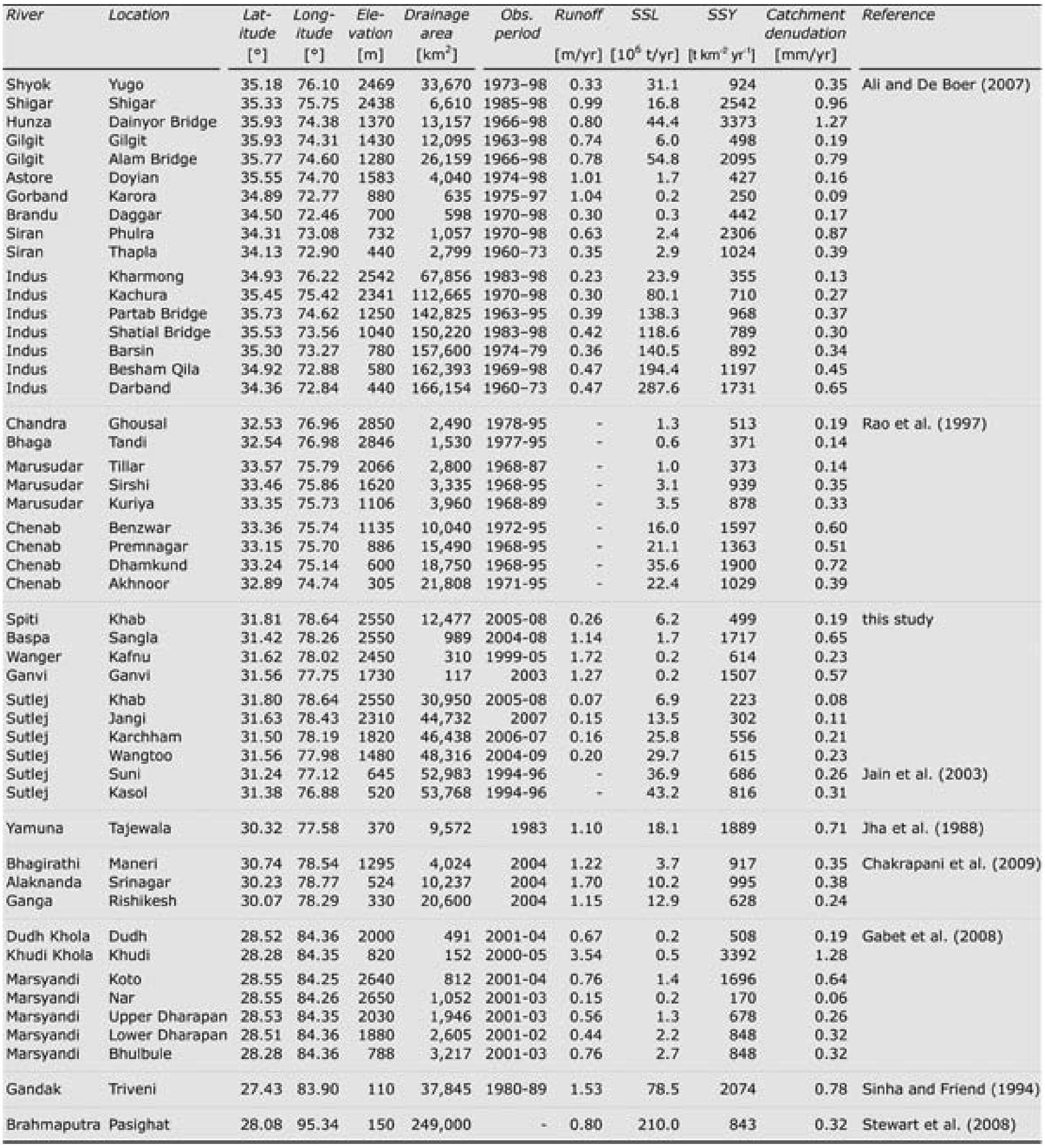

River	*Location*	*Latitude* [°]	*Longitude* [°]	*Elevation* [m]	*Drainage area* [km^2]	*Obs. period*	*Runoff* [m/yr]	*SSL* [10^6 t/yr]	*SSY* [t km^{-2} yr^{-1}]	*Catchment denudation* [mm/yr]	*Reference*
Shyok	Yugo	35.18	76.10	2469	33,670	1973–98	0.33	31.1	924	0.35	Ali and De Boer (2007)
Shigar	Shigar	35.33	75.75	2438	6,610	1985–98	0.99	16.8	2542	0.96	
Hunza	Dainyor Bridge	35.93	74.38	1370	13,157	1966–98	0.80	44.4	3373	1.27	
Gilgit	Gilgit	35.93	74.31	1430	12,095	1963–98	0.74	6.0	498	0.19	
Gilgit	Alam Bridge	35.77	74.60	1280	26,159	1966–98	0.78	54.8	2095	0.79	
Astore	Doyian	35.55	74.70	1583	4,040	1974–98	1.01	1.7	427	0.16	
Gorband	Karora	34.89	72.77	880	635	1975–97	1.04	0.2	250	0.09	
Brandu	Daggar	34.50	72.46	700	598	1970–98	0.30	0.3	442	0.17	
Siran	Phulra	34.31	73.08	732	1,057	1970–98	0.63	2.4	2306	0.87	
Siran	Thapla	34.13	72.90	440	2,799	1960–73	0.35	2.9	1024	0.39	
Indus	Kharmong	34.93	76.22	2542	67,856	1983–98	0.23	23.9	355	0.13	
Indus	Kachura	35.45	75.42	2341	112,665	1970–98	0.30	80.1	710	0.27	
Indus	Partab Bridge	35.73	74.62	1250	142,825	1963–95	0.39	138.3	968	0.37	
Indus	Shatial Bridge	35.53	73.56	1040	150,220	1983–98	0.42	118.6	789	0.30	
Indus	Barsin	35.30	73.27	780	157,600	1974–79	0.36	140.5	892	0.34	
Indus	Besham Qila	34.92	72.88	580	162,393	1969–98	0.47	194.4	1197	0.45	
Indus	Darband	34.36	72.84	440	166,154	1960–73	0.47	287.6	1731	0.65	
Chandra	Ghousal	32.53	76.96	2850	2,490	1978-95	-	1.3	513	0.19	Rao et al. (1997)
Bhaga	Tandi	32.54	76.98	2846	1,530	1977-95	-	0.6	371	0.14	
Marusudar	Tillar	33.57	75.79	2066	2,800	1968-87	-	1.0	373	0.14	
Marusudar	Sirshi	33.46	75.86	1620	3,335	1968-95	-	3.1	939	0.35	
Marusudar	Kuriya	33.35	75.73	1106	3,960	1968-89	-	3.5	878	0.33	
Chenab	Benzwar	33.36	75.74	1135	10,040	1972-95	-	16.0	1597	0.60	
Chenab	Premnagar	33.15	75.70	886	15,490	1968-95	-	21.1	1363	0.51	
Chenab	Dhamkund	33.24	75.14	600	18,750	1968-95	-	35.6	1900	0.72	
Chenab	Akhnoor	32.89	74.74	305	21,808	1971-95	-	22.4	1029	0.39	
Spiti	Khab	31.81	78.64	2550	12,477	2005-08	0.26	6.2	499	0.19	this study
Baspa	Sangla	31.42	78.26	2550	989	2004-08	1.14	1.7	1717	0.65	
Wanger	Kafnu	31.62	78.02	2450	310	1999-05	1.72	0.2	614	0.23	
Ganvi	Ganvi	31.56	77.75	1730	117	2003	1.27	0.2	1507	0.57	
Sutlej	Khab	31.80	78.64	2550	30,950	2005-08	0.07	6.9	223	0.08	
Sutlej	Jangi	31.63	78.43	2310	44,732	2007	0.15	13.5	302	0.11	
Sutlej	Karchham	31.50	78.19	1820	46,438	2006-07	0.16	25.8	556	0.21	
Sutlej	Wangtoo	31.56	77.98	1480	48,316	2004-09	0.20	29.7	615	0.23	
Sutlej	Suni	31.24	77.12	645	52,983	1994-96	-	36.9	686	0.26	Jain et al. (2003)
Sutlej	Kasol	31.38	76.88	520	53,768	1994-96	-	43.2	816	0.31	
Yamuna	Tajewala	30.32	77.58	370	9,572	1983	1.10	18.1	1889	0.71	Jha et al. (1988)
Bhagirathi	Maneri	30.74	78.54	1295	4,024	2004	1.22	3.7	917	0.35	Chakrapani et al. (2009)
Alaknanda	Srinagar	30.23	78.77	524	10,237	2004	1.70	10.2	995	0.38	
Ganga	Rishikesh	30.07	78.29	330	20,600	2004	1.15	12.9	628	0.24	
Dudh Khola	Dudh	28.52	84.36	2000	491	2001-04	0.67	0.2	508	0.19	Gabet et al. (2008)
Khudi Khola	Khudi	28.28	84.35	820	152	2000-05	3.54	0.5	3392	1.28	
Marsyandi	Koto	28.55	84.25	2640	812	2001-04	0.76	1.4	1696	0.64	
Marsyandi	Nar	28.55	84.26	2650	1,052	2001-03	0.15	0.2	170	0.06	
Marsyandi	Upper Dharapan	28.53	84.35	2030	1,946	2001-03	0.56	1.3	678	0.26	
Marsyandi	Lower Dharapan	28.51	84.36	1880	2,605	2001-02	0.44	2.2	848	0.32	
Marsyandi	Bhulbule	28.28	84.36	788	3,217	2001-03	0.76	2.7	848	0.32	
Gandak	Triveni	27.43	83.90	110	37,845	1980-89	1.53	78.5	2074	0.78	Sinha and Friend (1994)
Brahmaputra	Pasighat	28.08	95.34	150	249,000	-	0.80	210.0	843	0.32	Stewart et al. (2008)

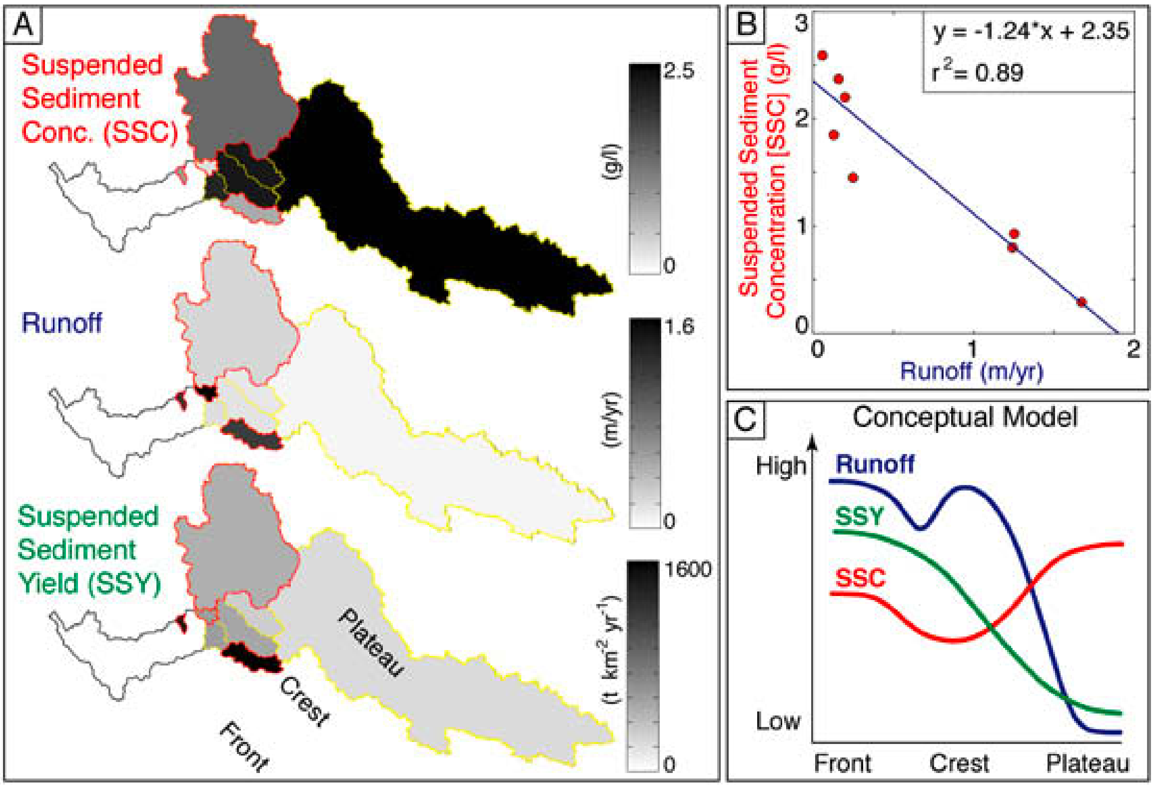

Figure 5.9: (A) **Spatial patterns in suspended sediment concentration (SSC), runoff, and suspended sediment yield (SSY)** of tributaries and Sutlej River catchments. Smaller catchments and tributaries overlie larger catchments. Runoff, SSC, and SSY data of each catchment is given in Table 5.1. (B) Negative correlation between mean annual SSC and runoff, weighted by the number of measurement years. (C) Conceptual model of the spatial distribution of SSC, runoff, and SSY from the Tibetan Plateau to the main Himalayan crest and the Himalayan Front.

Table 5.5: Suspended sediment flux in proglacial steams of the Himalaya and Karakorum. The catchment denudation rate is based on an average rock density of 2.65 g/cm^3, accounts only for the suspended sediment flux, and refers to the glacial catchment area, which exceeds the glacial area.

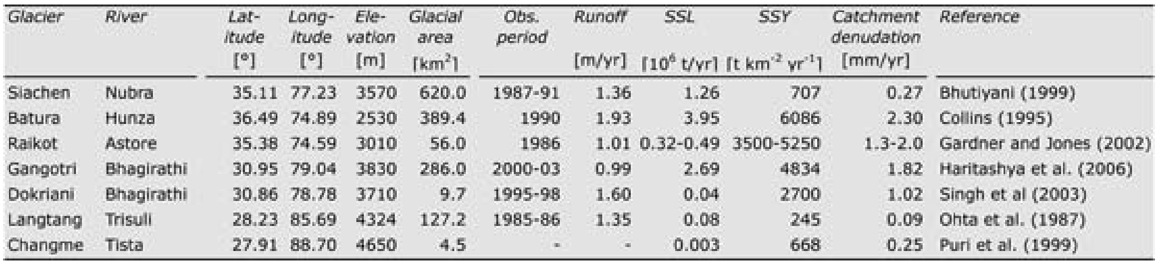

Glacier	*River*	*Latitude* [°]	*Longitude* [°]	*Elevation* [m]	*Glacial area* [km^2]	*Obs. period*	*Runoff* [m/yr]	*SSL* [10^6 t/yr]	*SSY* [t km^{-2} yr^{-1}]	*Catchment denudation* [mm/yr]	*Reference*
Siachen	Nubra	35.11	77.23	3570	620.0	1987-91	1.36	1.26	707	0.27	Bhutiyani (1999)
Batura	Hunza	36.49	74.89	2530	389.4	1990	1.93	3.95	6086	2.30	Collins (1995)
Raikot	Astore	35.38	74.59	3010	56.0	1986	1.01	0.32-0.49	3500-5250	1.3-2.0	Gardner and Jones (2002)
Gangotri	Bhagirathi	30.95	79.04	3830	286.0	2000-03	0.99	2.69	4834	1.82	Haritashya et al. (2006)
Dokriani	Bhagirathi	30.86	78.78	3710	9.7	1995-98	1.60	0.04	2700	1.02	Singh et al (2003)
Langtang	Trisuli	28.23	85.69	4324	127.2	1985-86	1.35	0.08	245	0.09	Ohta et al. (1987)
Changme	Tista	27.91	88.70	4650	4.5	-	-	0.003	668	0.25	Puri et al. (1999)

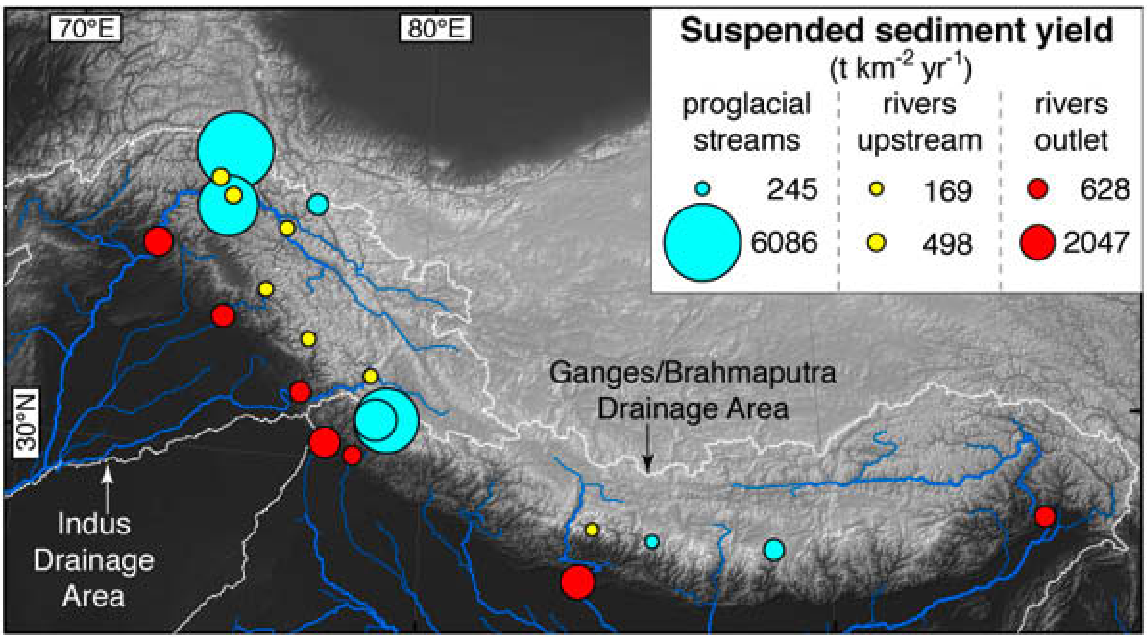

Figure 5.10: Suspended sediment yields along the Himalaya. Compilation of mean annual suspended sediment yield measurements in proglacial streams, upstream river catchments, and at outlet locations of major rivers. Data and respective references are given in Table 5.4 and Table 5.5.

In general, the high elevated, arid regions are characterized by low sediment yields, due to the low river discharge. This pattern is evident in the upstream catchments of the Indus, Chenab, Sutlej and Marsyandi River (Table 5.4). Farther downstream the sediment yield of these rivers increases gradually due to the high sediment flux of tributaries with a high glacial density, indicating high snowfall magnitudes, or intense monsoonal rainfall. These tributaries are generally characterized by high river discharge, which results in increased sediment flux. Consequently, the general north-to-south increase in Himalayan precipitation and runoff is also reflected in the sediment flux.

Sediment flux measurements in proglacial streams exhibit large variations in their suspended sediment yields (Table 5.5), which might be related to differences in lithologies, topography, glacial debris cover, and seasonal precipitation [*Scherler et al.*, 2011a,b]. Whereas some glaciers in the western Karakorum and western Himalaya are characterized by peak suspended sediment yields, exceeding those in monsoonal regions, others in the eastern Karakorum or central Himalaya exhibit low sediment yields, comparable to arid Plateau regions (Figure 5.10). Consequently, the glacial sediment yield exerts a large influence on the sediment flux characteristics of their downstream rivers. This is exemplified by the high sediment yield of the Hunza River

(3373 t km^{-2} yr^{-1}) that is fed by the Batura glacier (6086 t km^{-2} yr^{-1}), which contrasts the relatively low sediment yield of the Shyok River (924 t km^{-2} yr^{-1}) that is fed by the Siachen glacier (707 t km^{-2} yr^{-1}) (Table 5.5).

Interestingly, we do not observe a pronounced east-west trend in the Himalayan sediment flux, as noted by *Galy and France-Lanord* [2001]. Instead, most rivers are characterized by rather similar sediment yields at their outlet (Figure 5.10). This suggests a relatively uniform pattern of modern erosion at the mountain belt scale. Nearly constant rainfall amounts and extreme precipitation events along strike the Himalaya [*Bookhagen*, 2010; *Bookhagen and Burbank*, 2010], and our finding that monsoon precipitation appears to have the greatest influence on SSY may provide an explanation. However, we acknowledge that the available discharge dataset lacks spatially distributed sediment flux measurements from the central and eastern Himalaya.

5.5 Conclusion

In this study, we provide a comprehensive analysis of suspended sediment flux in the Sutlej Valley. Our analysis is based on ground measurements of river discharge and suspended sediment concentrations of eight catchments in the Sutlej Valley, which we analyze for general trends in suspended sediment flux and combine with remotely sensed rainfall and snow cover data to elucidate driving mechanisms for peak SSC. These data reveal four key conclusions: first, peak erosional events, which are characterized by high SSC, account for the bulk of the suspended sediment flux. SSC events that exceed the 90th percentile account leeward of the main orographic barrier for more than 50% of the total suspended sediment budget. Second, the peak SSC events, exceeding the 99th SSC percentile, coincide frequently (57-63%) with rainstorms, which trigger landslides especially in the semi-arid interior of the orogen. Furthermore, the Parechu Flood in June 2005 accounted for the peak suspended sediment flux and we identified glaciers to be associated with peak SSC event, as SSC variations correspond closely to temperature variations during the initiation period of glacial discharge in the Spiti Valley in 2008. Third, we find a general trend of increasing suspended sediment flux from the Tibetan Plateau to the Himalayan front. This trend is driven by a 20-fold increase in river discharge, which correlates with a 8-fold decrease in SSC. Fourth, in most catchments we find a weakly pronounced anticlockwise hysteresis loop, which indicates more suspended sediment transport during late summer, than during the onset of the monsoonal season. This indicates, that glacial discharge, which peaks in August, plays a vital role in the sediment supply of the

Sutlej River tributaries in the interior of the orogen. Overall, the combination of high runoff and low SSC levels at the main Himalayan crest suggests most suitable conditions hydropower stations in this region. Due to the general north-to-south drainage of the Himalaya, the crest region is drained by small to medium sized tributaries, which favors small to medium sized hydropower stations.

Chapter 6

Conclusions

In this study, I examined the general characteristics of and links between precipitation, river discharge, and sediment flux in the western Himalaya based on combined analyses of unique ground station data and remotely sensed imagery. The results of my analyses provide insights into precipitation gradients, spatial and temporal variations in the contribution of rainfall, snow- and glacial melt waters to river discharge, and their control on sediment fluxes in different climatic regions of the western Himalaya.

Due to the scarcity of ground-based observations, remote sensing imagery can be used as an important source of information to monitor several environmental variables in the Himalayan region. Comparison of remotely sensed TRMM 3B42 rainfall data with weather station records from the western Himalaya indicates that TRMM moderately well depicts rainfall in humid, frontal regions of the Himalaya within 10% of the weather station records, whereas it systematically overestimates weather station rainfall by a factor of up to 6 in the orogenic interior. This bias follows an inverse power-law relationship with mean annual precipitation, suggesting that TRMM 3B42 is less suited for rainfall monitoring in semi-arid to arid regions and requires calibration to ground station data.

The weather station data from the Sutlej catchment indicate that 40% of annual summer rainfall falls during 4-6 rainstorm events. In between years, however, the intensity of rainstorms in the orogenic interior varies considerably more than at the orogenic front. Similar to the distribution of rainfall events, the bulk of the suspended sediment flux occurs during a limited number of discharges. Particularly in semi-arid and arid interior regions of the orogen, those discharges with the 10% highest suspended sediment concentrations (SSC) transport more than 50% of the total suspended sediment. The data demonstrate that the highest sediment flux occurs during extreme monsoon rainstorm events, particularly in rivers draining the orogenic interior. Consequently, rainstorms are at present the most efficient process to mobilize and evacuate sediments from the orogen.

It has previously been argued that glaciers are highly efficient in eroding the high, elevated parts of the Himalaya, which is supported by high-suspended sediment yields of proglacial streams in the western Himalaya. Indeed, glaciated valleys often contain large volumes of sediment, in form of terraces, lake deposits, and moraines, but the glaciers seem to be incapable to transport their eroded material any further. This sediment evacuation appears to be most efficiently done by monsoonal rainstorms that account for landsliding and high river discharge. Therefore, it may be that distinct lag times exist between increased sediment supply during glacial cycles, and sediment evacuation during phases of enhanced monsoon intensity.

To differentiate the spatiotemporal distribution of rainfall, snow- and glacial melt to the Sutlej River discharge, I conducted a hydrological modeling study based on extensive remote-sensing calibration and adjustment procedures. This hydrological model accounts for the spatiotemporal variability in alpine terrain with high accuracy and could also be applied to other remote snow-covered regions to assess water resources. The spatial distribution of snow- and glacial melt is most pronounced at the main Himalayan crest and decreases towards the Tibetan Plateau. Under scenarios of future climate change, including higher temperatures, rising snowlines and declining glaciers, the long-term discharge of the Sutlej River is likely to be reduced, especially in the high-elevated internal parts of the orogen. Snow melt runoff may occur earlier in the year and decrease in magnitude while contributions from rainfall and glacial melt may increase on a short- to intermediate-term basis. The potential glacier meltdown and enhanced direct rainfall runoff, will also increase the downstream runoff variability.

In summary, the results from this thesis indicate that although runoff and discharge from snow and glacial meltwaters are important in areas located leeward of the main Himalayan crest, most sediment flux is associated with a limited number of monsoonal rainstorm events. If glaciers continue to shrink, and snow cover to decline, their contribution to discharge could dramatically drop, whereas sediment fluxes may stay constant or even increase if monsoon strength should increase. Such scenario would imply more rapid filling of hydropower reservoirs and increased turbine abrasion, which may by mitigated by improved preventive measures, including river discharge and sediment flux prediction models.

References

Akhtar, M., N. Ahmad, and M. J. Booij (2008), The impact of climate change on the water resources of hindukush-karakorum-himalaya region under different glacier coverage scenarios, *Journal of Hydrology*, *355*(1-4), 148–163.

Ali, K. F., and D. H. D. Boer (2007), Spatial patterns and variation of suspended sediment yield in the upper indus river basin, northern pakistan, *Journal of Hydrology*, *334*(3-4), 368–387.

Alizai, A., A. Carter, P. Clift, S. VanLaningham, J. Williams, and R. Kumar (2011), Sediment provenance, reworking and transport processes in the indus river by u-pb dating of detrital zircon grains, *Global and Planetary Change*, *76*(1-2), 33–55.

Allison, M. A., S. A. Kuehl, T. C. Martin, and A. Hassan (1998), Importance of flood-plain sedimentation for river sediment budgets and terrigenous input to the oceans: Insights from the brahmaputra-jamuna river, *Geology*, *26*(2), 175–178.

Anderson, E. A. (1976), *A point energy and mass balance model of a snow cover*, Silver Spring, Md.: Office of Hydrology, National Weather Service.

Arnold, N. S., I. C. Willis, M. J. Sharp, K. S. Richards, and W. J. Lawson (1996), A distributed surface energy-balance model for a small valley glacier. 1. development and testing for haut glacier d'Arolla, valais, switzerland, *Journal of Glaciology*, *42*(140), 77–89.

Avouac, J. P., and E. B. Burov (1996), Erosion as a driving mechanism of intracontinental mountain growth, *Journal of Geophysical Research*, *101*(B8), 17,747–17,769.

Aydin, A., and A. Basu (2005), The schmidt hammer in rock material characterization, *Engineering Geology*, (8), 1–14.

Baker, V. R., and V. Kale (1998), *Rivers Over Rock: Fluvial Processes in Bedrock Channels*, chap. The role of extreme events in shaping bedrock channels, pp. 153–165, Geophysics Monogrograph Series, Washington, DC.

Bales, R. C., N. P. Molotch, T. H. Painter, M. D. Dettinger, R. Rice, and J. Dozier (2006), Mountain hydrology of the western united states, *Water Resources Research*, *42*(8), 1–13.

Barnard, P. L., L. Owen, M. Sharma, and R. C. Finkel (2001), Natural and human-induced landsliding in the garhwal himalaya of northern india, *Geomorphology*, *40*(1-2), 21–35.

Barnett, T. P., J. C. Adam, and D. P. Lettenmaier (2005), Potential impacts of a warming climate on water availability in snow-dominated regions, *Nature*, *438*(7066), 303–9.

Barros, A. P., and T. J. Lang (2003), Monitoring the monsoon in the himalayas: Observations in central nepal, june 2001, *Monthly Weather Review*, *131*(7), 1408–1427.

Barros, A. P., and D. P. Lettenmaier (1994), Dynamic modeling of orographically induced precipitation, *Reviews of Geophysics*, *32*(3), 265–284.

Barros, A. P., M. Joshi, J. Putkonen, and D. W. Burbank (2000), A study of the 1999 monsoon rainfall in a mountainous region in central nepal using TRMM products and rain gauge observations, *Geophysical Research Letters*, *27*(22), 3683–3686.

Barros, A. P., G. Kim, E. Williams, and S. W. Nesbitt (2004), Probing orographic controls in the himalayas during the monsoon using satellite imagery, *Natural Hazards and Earth System Sciences*, *4*(1), 29–51.

Barros, A. P., S. Chiao, T. J. Lang, D. Burbank, and J. Putkonen (2006), From weather to climate—Seasonal and interannual variability of storms and implications for erosion processes in the himalaya, *Special Paper 398: Tectonics, Climate, and Landscape Evolution*, *398*(0), 17–38.

Bhambri, R., and T. Bolch (2009), Glacier mapping: a review with special reference to the indian himalayas, *Progress in Physical Geography*, *33*(5), 672–704.

Bhutiyani, M. (2000), Sediment load characteristics of a proglacial stream of siachen glacier and the erosion rate in nubra valley in the karakoram himalayas, india, *Journal of Hydrology*, *227*(1-4), 84–92.

Bierman, P., and E. J. Steig (1996), Estimating rates of denudation using cosmogenic isotope abundances in sediment, *Earth Surface Processes & Landforms*, *21*(2), 125–139.

Bierman, P. R. (1994), Using in situ produced cosmogenic isotopes to estimate rates of landscape evolution: A review from the geomorphic perspective, *Journal of Geophysical Research*, *99*(B7), 13,885–13,896.

Bilham, R., V. K. Gaur, and P. Molnar (2001), Earthquakes - himalayan seismic hazard, *Science*, *293*(5534), 1442–1444.

Blandford, T. R., K. S. Humes, B. J. Harshburger, B. C. Moore, V. P. Walden, and H. Ye (2008), Seasonal and synoptic variations in Near-Surface air temperature lapse rates in a mountainous basin, *Journal of Applied Meteorology and Climatology*, *47*(1), 249–261.

Blanford, H. (1884), On the connection of the himalayan snowfall with dry winds and seasons of drought in india, *Proc. Roy. Soc. London*, *37*, 3–22.

Bollasina, M., L. Bertolani, and G. Tartari (2002), Meteorological observations in the khumbu valley, nepal himalayas, 1994-1999, *Bullitin of Glacier Research*, *19*, 1–11.

Bookhagen, B. (2010), Appearance of extreme monsoonal rainfall events and their impact on erosion in the himalaya, *Geomatics, Natural Hazards and Risk*, *1*(1), 37–50.

Bookhagen, B., and D. W. Burbank (2006), Topography, relief, and TRMM-derived rainfall variations along the himalaya, *Geophysical Research Letters*, *33*(8), L08,405.

Bookhagen, B., and D. W. Burbank (2010), Toward a complete himalayan hydrological budget: Spatiotemporal distribution of snowmelt and rainfall and their impact on river discharge, *Journal of Geophysical Research*, *115*, F03,019, 25pp.

Bookhagen, B., R. C. Thiede, and M. R. Strecker (2005a), Abnormal monsoon years and their control on erosion and sediment flux in the high, arid northwest himalaya, *Earth and Planetary Science Letters*, *231*(1-2), 131–146.

Bookhagen, B., R. C. Thiede, and M. R. Strecker (2005b), Late quaternary intensified monsoon phases control landscape evolution in the northwest himalaya, *Geology*, *33*(2), 149–152.

Boos, W., and Z. Kuang (2010), Dominant control of the south asian monsoon by orographic insulation versus plateau heating, *Nature*, *463*, 218–223.

Braun, L. N., W. Grabs, and B. Rana (1993), Application of a conceptual Precipitation-Runoff model in the Langtang Khola Basin, nepal himalaya, *IAHS Publications*, *218*, 221–237.

Brock, B. W., and N. S. Arnold (2000), A spreadsheet-based (Microsoft excel) point surface energy balance model for glacier and snow melt studies, *Earth Surface Processes and Landforms*, *25*(6), 649–658.

Brock, B. W., C. Mihalcea, M. P. Kirkbride, G. Diolaiuti, M. E. J. Cutler, and C. Smiraglia (2010), Meteorology and surface energy fluxes in the 2005-2007 ablation seasons at the miage debris-covered glacier, mont blanc massif, italian alps, *Journal of Geophysical Research*, *115*(D9), 1–16.

Burbank, D. (2009), *Encyclopedia of Paleoclimatology and Ancient Environments*, chap. Mountain Uplift and Climate Change, pp. 596–606, Springer.

Burbank, D. W., J. Leland, E. Fielding, R. S. Anderson, N. Brozovic, M. R. Reid, and C. Duncan (1996), Bedrock incision, rock uplift and threshold hillslopes in the northwestern himalayas, *Nature*, *379*(6565), 505–510.

Burbank, D. W., A. E. Blythe, J. Putkonen, B. Pratt-Sitaula, E. Gabet, M. Oskin, A. Barros, and T. P. Ojha (2003), Decoupling of erosion and precipitation in the himalayas, *Nature*, *426*(6967), 652–655.

Burchfiel, B., Z. Chen, K. Hodges, Y. Liu, and L. Royden (1992), The south tibetan detachment system, himalayan orogen: extension contemporaneous with and parallel to shortening in a collisional mountain, *Geol. Soc. Am. Spec. Pap.*, *269*, 1–42.

Burg, J. P., P. Nievergelt, F. Oberli, D. Seward, P. Davy, and J. Maurin (1998), The namche barwa syntaxis: evidence for exhumation related to compressional crustal folding, *J. Southeast Asian Earth Sci.*, *16*(239-252), 239–252.

Burtin, A., L. Bollinger, R. Cattin, J. Vergne, and J. L. Nabelek (2010), Spatiotemporal sequence of himalayan debris flow from High-Frequency seismic noise analysis, *Journal of Geophysical Research-Earth Surface*, *114*, F04,009.

Campbell, F. B., and H. A. Bauder (1940), A rating-curve method for determining silt-discharge of streams, *EOS (Trans. Am. Geophys. Union)*, *21*, 603–607.

Carson, B. (1992), The land, the farmer, and the future: a soil fertility management strategy for nepal., *Tech. rep.*, Kathmandu, Nepal.

Cazorzi, F., and G. Dallafontana (1996), Snowmelt modelling by combining air temperature and a distributed radiation index, *Journal of Hydrology*, *181*(1-4), 169–187.

Chakrapani, G., and R. Saini (2009), Temporal and spatial variations in water discharge and sediment load in the alaknanda and bhagirathi rivers in himalaya, india, *Journal of Asian Earth Sciences*, *35*, 545–553.

Chalise, S., and N. Khanal (2001), An introduction to climate, hydrology and landslide hazards in the hindu kush-himalayan region., in *Landslide Hazard Mitigation in the Hindu Kush-Himalayas*, pp. 51–62, ICIMOD, Kathmandu.

Cheng, G. D., and T. H. Wu (2007), Responses of permafrost to climate change and their environmental significance, qinghai-tibet plateau, *Journal of Geophysical Research*, *112*(F2), F02S03.

Cleugh, H., R. Leuning, Q. Mu, and S. Running (2007), Regional evaporation estimates from flux tower and MODIS satellite data, *Remote Sensing of Environment*, *106*(3), 285–304.

Clift, P. D., N. Shimizu, G. D. Layne, J. S. Blusztajn, C. Gaedicke, H. U. Schluter, M. K. Clark, and S. Amjad (2001), Development of the indus fan and its significance for the erosional history of the western himalaya and karakoram, *Geological Society of America Bulletin*, *113*(8), 1039–1051.

Clift, P. D., K. V. Hodges, D. Heslop, R. Hannigan, H. V. Long, and G. Calves (2008), Correlation of himalayan exhumation rates and asian monsoon intensity, *Nature Geoscience*, *1*(12), 875–880.

Coll, C., V. Caselles, J. Galve, E. Valor, R. Niclos, J. Sanchez, and R. Rivas (2005), Ground measurements for the validation of land surface temperatures derived from AATSR and MODIS data, *Remote Sensing of Environment*, *97*(3), 288–300.

Collins, D. N., and S. I. Hasnain (1995), Runoff and sediment transport from giacierized basins at the himalayan scale, *International Association of Hydrological Sciences*, *226*(226), 17–25.

Coppus, R., and A. C. Imeson (2002), Extreme events controlling erosion and sediment transport in a semi-arid sub-andean valley, *Earth Surface Processes and Landforms*, *27*(13), 1365–1375.

Craddock, W. H., D. W. Burbank, B. Bookhagen, and E. J. Gabet (2007), Bedrock channel geometry along an orographic rainfall gradient in the upper marsyandi river valley in central nepal, *Journal of Geophysical Research-Earth Surface*, *112*, F03,007, 17pp.

Crozier, M. (1999), Prediction of rainfall-triggered landslides: a test of the antecdent water status model., *Earth Surface Processes and Landforms*, *24*, 825–833.

Curray, J., F. Emmel, and D. Moore (2003), The bengal fan: morphology, geometry, stratigraphy, history and processes, *Marine and Petroleum Geology*, *19*(10), 1191–1223.

Datt, P., P. K. Srivastava, P. S. Negi, and P. K. Satyawali (2008), Surface energy balance of seasonal snow cover for snow-melt estimation in N-W Himalaya, *Journal of Earth System Science*, *117*(5), 567–573.

de Ferranti, J. (2006), Digital elevation data of high asia, http://www.viewfinderpanoramas.org/.

Dimri, A. (2006), Surface and upper air fields during extreme winter precipitation over the western Himalayas, *Pure and Applied Geophysics*, *163*(8), 1679–1698.

Dimri, A. P., U. C. Mohanty, and M. Mandal (2004), Simulation of heavy precipitation associated with an intense western disturbance over western himalayas, *Natural Hazards*, *31*(2), 499–521.

Dinku, T., S. Chidzambwa, P. Ceccato, S. J. Connor, and C. F. Ropelewski (2008), Validation of high-resolution satellite rainfall products over complex terrain, *International Journal of Remote Sensing*, *29*(14), 4097–4110.

Dortch, J., L. Owen, C. Dietsch, M. Caffee, and K. Bovard (2011), Episodic fluvial incision of rivers and rock uplift in the himalaya and transhimalaya, *Geological Society of London*, *168*(783-804), 783–804.

Dozier, J., T. H. Painter, K. Rittger, and J. E. Frew (2008), Time-space continuity of daily maps of fractional snow cover and albedo from MODIS, *Advances in Water Resources*, *31*(11), 1515–1526.

Duan, K. Q., T. D. Yao, and L. G. Thompson (2006), Response of monsoon precipitation in the himalayas to global warming, *Journal of Geophysical Research*, *111*, D19,110.

Dury, G. H. (1981), *An Introduction to Environmental Systems*, Heinemann.

Edmond, J., and Y. Huh (1997), Chemical weathering yields from basement and orogenic terrains in hot and cold climates, in *Tectonic uplift and climate change*, pp. 330–350, Plenum Press, New York.

Einfalt, T., and S. Michaelides (2008), *Quality control of precipitation data, Precipitation: Advances in Measurement, Estimation and Prediction*, vol. Precipitation: Advances in Measurement, Estimation and Prediction.

Eriksson, M., X. JianChu, A. B. Shrestha, R. A. Vaidya, S. Nepal, and K. Sandstroem (2009), The changing himalayas: impact of climate change on water resources and livelihoods in the greater himalayas., *Tech. rep.*, ICIMOD.

FAO (2009), Land Cover Map of the Himalaya Region, Food and Agriculture Organization of the United Nations (FAO), Rome.

Farr, T. G., et al. (2007), The shuttle radar topography mission, *Reviews of Geophysics*, *45*(2), RG2004.

Ferguson, R. I. (1999), Snowmelt runoff models, *Progress in Physical Geography*, *23*(2), 205–227.

Fielding, E., B. Isacks, M. Barazangi, and C. Duncan (1994), How flat is tibet?, *Geology*, *22*(2), 163–167.

Finlayson, D. P., D. R. Montgomery, and B. Hallet (2002), Spatial coincidence of rapid inferred erosion within young metamorphic massifs in the himalayas., *Geology*, (30), 219–222.

Flohn, H. (1956), Zum klima der hochgebirge zentralasiens ii, *Meteorologische Rundschau*, *9*, 85–88.

Flohn, H. (1957), Large-scale aspects of the "summer monsoon" in south and east asia, *Journal of the Meteorological Society of Japan*, *75*, 180–186.

France-Lanord, C., and L. Derry (1997), Organic carbon burial forcing of the carbon cycle from himalayan erosion, *Nature*, *390*, 65–67.

Fritsch, F. N., and R. E. Carlson (1980), Monotone piecewise cubic interpolation, *SIAM Journal on Numerical Analysis*, *7*(2), 238–246.

Froehlich, W., and L. Starkel (1987), Normal and extreme monsoon rains: their role in the shaping of the darjeeling himalaya, *Studia Geomorphologica Carpatho-Balcanica*, *21*, 129–160.

Fu, C., and J. O. Fletcher (1985), The relationship between tibet tropical ocean thermal contrast and the interannual variability of indian monsoon rainfall., *Journal of Climate and Applied Meteorology*, *24*, 841–847.

Fu, P., and P. M. Rich (2002), A geometric solar radiation model with applications in agriculture and forestry, *Computers and Electronics in Agriculture*, *37*(1-3), 25–35.

Fuchs, G. (1975), Contributions to the geology of the north-western himalayas, *Tech. rep.*, Abhandlungen der Geologischen Bundesanstalt Vienna.

Gabet, E., D. Burbank, B. Prattsitaula, J. Putkonen, and B. Bookhagen (2008), Modern erosion rates in the high himalayas of nepal, *Earth and Planetary Science Letters*, *267*(3-4), 482–494.

Gabet, E. J., D. W. Burbank, J. K. Putkonen, B. A. Pratt-Sitaula, and T. Ojha (2004), Rainfall thresholds for landsliding in the himalayas of nepal, *Geomorphology*, *63*(3-4), 131–143.

Gadgil, S. (2003), The indian monsoon and its variability, *Annual Review of Earth and Planetary Sciences*, *31*, 429–467.

Gafurov, A., and A. Bárdossy (2009), Cloud removal methodology from MODIS snow cover product, *Hydrology and Earth System Sciences*, *13*(7), 1361–1373.

Galy, A., and C. France-Lanord (2001), Higher erosion rates in the Himalaya: Geochemical constraints on riverine fluxes, *Geology*, *29*(1), 23–26.

Gansser, A. (1964), *The Geology of the Himalayas*, Wiley Interscience, New York.

Gardner, J., and N. Jones (2002), *Himalaya to the Sea: Geology, Geomorphology and the Quaternary*, chap. Sediment transport and yield in the Raikot glacier, Routledge.

Garg, N. K., and Q. Hassan (2007), Alarming scarcity of water in india, *Current Science*, *93*(7), 932–941.

Garrick, M., C. Cunnane, and J. E. Nash (1978), A criterion of efficiency for rainfall-runoff models, *Journal of Hydrology*, *36*, 375–381.

Garzanti, E., G. Vezzoli, S. Ando, J. Lave, M. Attal, C. Francelanord, and P. Decelles (2007), Quantifying sand provenance and erosion (Marsyandi river, nepal himalaya), *Earth and Planetary Science Letters*, *258*(3-4), 500–515.

Gole, C., and S. Chitale (1966), Inland deltabuilding activity of the kosi river, *Journal of Hydraulic Division of the American Society of Civil Engineers*, *2*, 111–126.

Goodbred, S. L., and S. A. Kuehl (2000), The significance of large sediment supply, active tectonism, and eustasy on margin sequence development: Late quaternary stratigraphy and evolution of the ganges-brahmaputra delta, *Sediment. Geol.*, *133*(3-4), 227–248.

Goodbred, S. L., and S. A. Kuehl (2003), The production, transport, and accumulation of sediment: a cross-section of recent developments with an emphasis on climate effects, *Sediment. Geol.*, *162*(1-2), 1–3.

Goswami, B. N., V. Venugopal, D. Sengupta, M. S. Madhusoodanan, and P. K. Xavier (2006), Increasing trend of extreme rain events over india in a warming environment, *Science*, *314*(5804), 1442–1445.

Goswami, D. (1985), Brahmaputra river, assam, india: Physiography, basin denudation, and channel aggradation, *Water Resources Research*, *21*, 959–78.

Greuell, W., and J. Oerlemans (2005), Validation of AVHRR- and MODIS-derived albedos of snow and ice surfaces by means of helicopter measurements, *Journal of Glaciology*, *51*(172), 37–48.

Gumbel, E. J. (1958), *Statistics of Extremes*, Columbia University Press.

Gupta, V., and M. P. Sah (2007), Impact of the Trans-Himalayan landslide lake outburst flood (LLOF) in the satluj catchment, himachal pradesh, india, *Natural Hazards*, *45*(3), 379–390.

Gurtz, J., A. Baltensweiler, and H. Lang (1999), Spatially distributed hydrotope-based modelling of evapotranspiration and runoff in mountainous basins, *Hydrological Processes*, *13*(17), 2751–2768.

Hahn, D. G., and S. Manabe (1975), The role of mountains in the south asian monsoon circulation, *Journal of Atmospheric Science*, *32*, 1515–1541.

Hall, D., G. A. Riggs, V. V. Salomonson, N. E. DiGirolamo, and K. J. Bayr (2002), MODIS snow-cover products, *Remote Sensing of Environment*, *83*(1-2), 181–194.

Hall, D. K., and G. A. Riggs (2007), Accuracy assessment of the MODIS snow products, *Earth Science*, *1547*, 1534–1547.

Hall, D. K., G. A. Riggs, and V. V. Salomonson (1995), Development of methods for mapping global snow cover using moderate resolution imaging spectroradiometer data, *Remote Sensing of Environment*, *54*(2), 127–140.

Hallet, B., L. Hunter, and J. Bogenc (1996), Rates of erosion and sediment evacuation by glaciers: A review of field data and their implications, *Global and Planetary Change*, *12*(1-4), 213–235.

Halley, E. (1686), An historical account of the trade winds and monsoons observable in the seas between and near the tropics with an attempt to assign a physical cause of the traid winds, *Philosophical Transactions of the Royal Society London*, *16*, 153–168.

Hancock, G., R. Anderson, and K. Whipple (1998), *Rivers over rock: fluvial processes in bedrock channels*, chap. Beyond power: bedrock river incision process and form, pp. 35–60, American Geophysical Union, Geophysical Monograph, Washington, DC.

Haritashya, U., P. Singh, N. Kumar, and R. Gupta (2006), Suspended sediment from the gangotri glacier: Quantification, variability and associations with discharge and air temperature, *Journal of Hydrology*, *321*, 116–130.

Hartshorn, K., N. Hovius, W. Dade, and R. Slingerland (2002), Climate-driven bedrock incision in an active mountain belt, *Science*, *297*, 2036–2038.

Hatwar, H. R., B. P. Yadav, and Y. V. Rama Rao (2005), Prediction of western disturbances and associated weather over western himalayas, *Current Science*, *88*(6), 913–920.

Heim, A., and A. Gansser (1939), Central himalaya geological observations of the swiss expedition 1936, *Tech. rep.*, Zurich.

Heimsath, A. (2000), Himalayan erosion, http://www.public.asu.edu/ aheimsat/publications/Heimsath

Heimsath, A. M., and R. McGlynn (2008), Quantifying periglacial erosion in the nepal high himalaya, *Geomorphology*, *97*(1-2), 5–23.

Hock, R. (1999), A distributed temperature-index ice- and snowmelt model including potential direct solar radiation, *Journal of Glaciology*, *45*(149), 101–111.

Hock, R. (2003), Temperature index melt modelling in mountain areas, *Journal of Hydrology*, *282*(1-4), 104–115.

Hodges, K. V. (2000), Tectonics of the himalaya and southern tibet from two perspectives, *Geol. Soc. Am., Bull.*, *112*, 324–350.

Houze, R. A. J., K. L. Rasmussen, S. Medina, S. R. Brodzik, and U. Romatschke (2011), Anomalous atmospheric events leading to the summer 2010 floods in pakistan, *Bulletin of the American Meteorological Society*, *92*(3), 291–298.

Huete, A., K. Didan, T. Miura, and e. al. (2002), Overview of the radiometric and biophysical performance of the modis vegetation indices, *Remote Sensing of Environment*, *83*(1-2), 195–213.

Huffman, G. J., R. F. Adler, D. T. Bolvin, G. Gu, E. J. Nelkin, K. P. Bowman, Y. Hong, E. F. Stocker, and D. B. Wolff (2007), The TRMM multisatellite precipitation analysis (TMPA): Quasi-Global, multiyear, Combined-Sensor precipitation estimates at fine scales, *Journal of Hydrometeorology*, *8*(1), 38–38.

Huss, M., D. Farinotti, A. Bauder, and M. Funk (2008), Modelling runoff from highly glacierized alpine drainage basins in a changing climate, *Hydrological Processes*, *22*(19), 3888–3902.

Immerzeel, W. (2008), Historical trends and future predictions of climate variability in the brahmaputra basin, *Internation Journal of Climatology*, *28*(2), 243–254.

Immerzeel, W. W., P. Droogers, S. M. de Jong, and M. F. P. Bierkens (2009), Large-scale monitoring of snow cover and runoff simulation in Himalayan river basins using remote sensing, *Remote Sensing of Environment*, *113*(1), 40–49, doi:10.1016/j.rse.2008.08.010.

Immerzeel, W. W., L. P. H. van Beek, and M. F. P. Bierkens (2010), Climate change will affect the asian water towers, *Science*, *328*(5984), 1382–5.

IPCC (2007), *Climate Change 2007: Impacts, Adaptation and Vulnerability*, Cambridge Univ. Press, Contribution of Working Group II to the Fourth Assessment Report of the Intergovernmental Panel on Climate Change, (M.L. Parry, O.F. Canziani, J.P. Palutikof, P.J. van der Linden and C.E. Hanson).

Ives, J., and B. Messerli (1989), *The Himalayan dilemma: reconciling development and conservation*, 295 pp., London and New York: Routledge.

Jain, S. K., P. Singh, A. K. Saraf, and S. M. Seth (2003), Estimation of sediment yield for a rain, snow and glacier fed river in the western himalayan region, *Water Resources Management*, *17*(5), 377–393.

Jha, P., V. Subramanian, and R. Sitasawad (1988), Chemical and sediment mass transfer in the yamuna river - a tributary of the ganges system, *Journal of Hydrology*, *104*, 237–246.

Jodha, N. S. (1985), Population growth and the decline of common property resources in rajasthan, india, *Population and Development Review*, *11*(2).

Kääb, A., F. Paul, M. Maisch, M. Hoelzle, and W. Haeberli (2002), The new remote-sensing-derived swiss glacier inventory: II. first results, *Annals of Glaciology*, *34*, 362–366.

Kale, V. (2002), Fluvial geomorphology of indian rivers: an overview, *Progress in Physical Geography*, *26*(3), 400–433.

Kale, V., S. Karlekar, and L. Deodhar (1986), Channel morphology and hydraulic characteristics of vashishthi river, maharashtra, *Transactions Institute of Indian Geographers*, *8*, 113–126.

Katz, O., Z. Reches, and J.-C. Roegiers (2000), Evaluation of mechanical rock properties using a schmidt hammer, *International Journal of Rock Mechanics and Mining Sciences*, *37*, 723–728.

Kehrwald, N. M., L. G. Thompson, T. D. Yao, E. Mosley-Thompson, U. Schotterer, V. Alfimov, J. Beer, J. Eikenberg, and M. E. Davis (2008), Mass loss on himalayan glacier endangers water resources, *Geophys. Res. Lett.*, *35*(22), L22,503–6.

Klein, A. G., and A. C. Barnett (2003), Validation of daily MODIS snow cover maps of the upper rio grande river basin for the 2000-2001 snow year, *Remote Sensing of Environment*, *86*(2), 162–176.

Klootwijk, C., F. Gee, J. Peirce, G. Smith, and P. McFadden (1992), An early india contact: paleomagnetic constraints from ninetyeast ridge, *Geology*, *20*, 395–398.

Kripalani, R. H., K. Ashwini, and S. Sabade (2003), Western himalayan snow cover and indian monsoon rainfall: A re-examination with insat and ncep/ncar data, *Theoretical and Applied Climatology*, *74*, 1–18.

Kumar, K. K., K. Kamala, B. Rajagopalan, M. P. Hoerling, J. K. Eischeid, S. K. Patwardhan, G. Srinivasan, B. N. Goswami, and R. Nemani (2011), The once and future pulse of indian monsoonal climate, *Climate Dynamics*, *36*(11-12), 2159–2170.

Kumar, R., J. Bales, R. Jubach, P. Gyamba, M. Kane, and A. Scott (2007a), Flash-flood warning for the upper sutlej river basin, northern india, *Tech. rep.*

Kumar, V., P. Singh, and V. Singh (2007b), Snow and glacier melt contribution in the beas river at pandoh dam, himachal pradesh, india / contribution de la fonte nivale et glaciaire a la riviere beas au barrage pandoh, himachal pradesh, inde, *Hydrological Sciences Journal*, *52*(2), 376–388.

Lal, D., N. B. W. Harris, K. K. Sharma, Z. Gu, L. Ding, T. Liu, W. Dong, M. W. Caffee, and J. T. J. a (2003), Erosion history of the tibetan plateau since the last interglacial: constraints from the first studies of cosmogenic 10Be from tibetan bedrock, *Earth and Planetary Science Letters*, *217*(1-2), 33–42.

Lang, H., and L. Braun (1990), On the information content of air temperature in the context of snow melt estimation, (190).

Lang, T. J., and A. P. Barros (2002), An investigation of the onsets of the 1999 and 2000 monsoons in central nepal, *Monthly Weather Review*, *130*(5), 1299–1299.

Lang, T. J., and A. P. Barros (2004), Winter storms in the central himalayas, *Journal of the Meteorological Society of Japan*, *82*(3), 829–844.

Larson, K., R. Buergmann, R. Bilham, and J. Freymueller (1999), Kinematics of the india-eurasia collision zone from gps measurements, *Journal of Geophysical Research*, *104*, 1077–1093.

Lawrence, D. M., and A. G. Slater (2005), A projection of severe near-surface permafrost degradation during the 21st century, *Geophysical Research Letters*, *32*(24), L24,401–5.

Leopold, L. B., and W. W. Emmett (1976), Bedload measurements, East Fork River, wyoming, *Proceedings of the National Academy of Science*, *73*(4), 1000–1004.

Li, X., and M. W. Williams (2008), Snowmelt runoff modelling in an arid mountain watershed , tarim basin , china, *Hydrological Processes*, *22*(19), 3931–3940.

Liu, X. D., and B. D. Chen (2000), Climatic warming in the tibetan plateau during recent decades, *Internation Journal of Climatology*, *20*(14), 1729–1742.

Lundquist, J. D., and D. R. Cayan (2007), Surface temperature patterns in complex terrain: Daily variations and long-term change in the central sierra nevada, california, *Journal of Geophysical Research*, *112*(D11), 1–15.

Male, D. H., and R. J. Granger (1981), Snow surface energy exchange, *Water Resources Research*, *17*(3), 609–609.

Martinec, J. (1975), Snowmelt - runoff model for stream flow forecasts, *Nordic Hydrology*, *6*(3), 145–154.

Maussion, F., D. Scherer, R. Finkelnburg, J. Richters, W. Yang, and T. Yao (2010), WRF simulation of a precipitation event over the tibetan plateau, china – an assessment using remote sensing and ground observations, *Hydrology and Earth System Sciences Discussions*, *7*(3), 3551–3589.

May, W. (2004), Variability and extremes of daily rainfall during the indian summer monsoon in the period 1901-1989, *Global and Planetary Change*, *44*(1-4), 83–105.

McCabe, G. J., M. P. Clark, and L. E. Hay (2007), Rain-on-snow events in the western united states, *Bullitin of the American Meteorological Sociaty*, *88*(3), 319.

McDonald, R. I., P. Green, D. Balk, B. M. Fekete, C. Revenga, M. Todd, and M. Montgomery (2011), Urban growth, climate change, and freshwater availability, *Proceedings of the National Academy of Science*, *108*(15), 6312–6317.

McFarland, M., R. Miller, and C. Neale (1990), Land surface temperature derived from the SSM/I passive microwave brightness temperatures, *Geoscience and Remote Sensing*, *28*(5), 839 – 845.

Meade, R. H. (1988), *Physical and chemical weathering in geochemical cycles*, chap. Movement and storage of sediment in river systems, pp. 165–179, Dordrecht: Kluver.

Meehan, W. (1991), *Influences of forest and rangeland management on salmonid fishes and their habitats*, American Fisheries Society, Bethesda, MD.

Meehl, G. (1994), Coupled land-ocean-atmosphere processes and south asian monsoon variability, *Science*, *266*(5183), 263–267.

Meehl, G. A., and W. M. Washington (1993), South asian summer monsoon variability in a model with doubled atmospheric carbon dioxide concentration, *Science*, *260*(5111), 1101–1104.

Miller, C., U. Kloetzli, W. Frank, M. Thoeni, and B. Grasemann (2000), Proterozoic crustal evolution in the nw himalaya (india) as recorded by circa 1.80 ga mafic and 1.84 ga granitic magmatism, *Precambrian Res.*, *103*, 191–206.

Milliman, J., and R. Meade (1983), Worldwide delivery of river sediment to the oceans, *Journal of Geology*, *91*, 1–21.

Milliman, J. D., and J. P. M. Syvitski (1992), Geomorphic/Tectonic control of sediment discharge to the ocean: The importance of small mountainous rivers, *The Journal of Geology*, *100*(5), 525–544.

Minder, J. R., P. W. Mote, and J. D. Lundquist (2010), Surface temperature lapse rates over complex terrain: Lessons from the cascade mountains, *Journal of Geophysical Research*, *115*, D14,122, 13 pp.

Mohindra, R., and B. Prakash (1994), Geomorphology and neotectonic activity of the gandak megafan and adjoining areas, middle gangetic plains, *Journal of Geological Society of India*, *43*, 149–57.

Molnar, P., and P. England (1990), Late cenozoic uplift of mountain ranges and global climate change: chicken or egg?, *Nature*, *346*(6279), 29–34.

Molnar, P., and P. Tapponnier (1975), Cenozoic tectonics of asia: Effects of a continental collision, *Science*, *189*(4201), 419–426.

Molnar, P., R. S. Anderson, and S. P. Anderson (2007), Tectonics, fracturing of rock, and erosion, *Journal of Geophysical Research*, *112*(F3), 1–12.

Molotch, N. P., and D. Norte (2009), Reconstructing snow water equivalent in the rio grande headwaters using remotely sensed snow cover data and a spatially distributed snowmelt model, *Hydrological Processes*, *1089*, 1076–1089.

Monteith, J. L. (1965), Evaporation and environment, *Symposia of the Society for Experimental Biology*, *19*, 205–234.

Morgan, R. P. C. (2004), *Soil erosion and conservation*, 320 pp., Wiley-Blackwell.

Mu, Q., F. A. Heinsch, M. Zhao, and S. W. Running (2007), Development of a global evapotranspiration algorithm based on MODIS and global meteorology data, *Remote Sensing of Environment*, *111*(4), 519–536.

Nash, J. E., and J. V. Sutcliffe (1970), River flow forecasting through conceptual models. part i: a discussion of principles, *Journal of Hydrology*, *10*, 282–290.

Ohmura, A. (2001), Physical basis for the Temperature-Based Melt-Index method, *Journal of Applied Meteorology*, *40*(4), 753–761.

Ohta, T., Y. Fukushima, M. Suzuki, H. Motoyama, K. Kawashima, and H. Kubota (1987), Suspended sediment yield in a glaciated watershed of langtang valley, nepal himalayas., *Bullitin of Glacier Research*, *5*, 19–24.

Owen, L. A., R. C. Finkel, P. L. Barnard, H. Z. Ma, K. Asahi, M. W. Caffee, and E. Derbyshire (2005), Climatic and topographic controls on the style and timing of late quaternary glaciation throughout tibet and the himalaya defined by be-10 cosmogenic radionuclide surface exposure dating, *Quaternary Science Reviews*, *24*(12-13), 1391–1411.

Pan, M., H. Li, and E. Wood (2010), Assessing the skill of satellite-based precipitation estimates in hydrologic applications, *Water Resources Research*, *46*(9), 1–10.

Parajka, J., and G. Blöschl (2006), Validation of MODIS snow cover images over austria, *Hydrology and Earth System Sciences Discussions*, *3*(4), 1569–1601.

Paul, F., A. Kääb, M. Maisch, T. Kellenberger, and W. Haeberli (2002), The new remote-sensing-derived Swiss glacier inventory: I. Methods, *Annals of Glaciology*, *34*(1), 355–361.

Pellicciotti, F., B. Brock, U. Strasser, P. Burlando, M. Funk, and J. Corripio (2005), An enhanced temperature-index glacier melt model including the shortwave radiation balance: development and testing for Haut Glacier d'Arolla, Switzerland, *Journal of Glaciology*, *51*(175), 573–587.

Plummer, M., and F. M. Phillips (2003), A 2-D numerical model of snow/ice energy balance and ice flow for paleoclimatic interpretation of glacial geomorphic features, *Quaternary Science Reviews*, *22*(14), 1389–1406.

Pratt-Sitaula, B., M. Garde, D. W. Burbank, M. Oskin, A. Heimsath, and E. Gabet (2007), Bedload-to-suspended load ratio and rapid bedrock incision from himalayan landslide-dam lake record, *Quaternary Research*, *68*(1), 111–120.

Prince, S. D., S. J. Goetz, R. O. Dubayah, K. P. Czajkowski, and M. Thawley (1998), Inference of surface and air temperature, atmospheric precipitable water and vapor pressure deficit using advanced very High-Resolution radiometer satellite observations: comparison with field observations, *Journal of Hydrology*, *213*(1-4), 230–249.

Puri, V. (1999), Glaciohydrological and suspended sediment load studies in the melt water channel of changme khangpu glacier, mangam district, sikkim, in *Symposium on Snow, Ice and Glaciers - A Himalayan Prospective*, Lucknow.

Putkonen, J. K. (2004), Continuous snow and rain data at 500 to 4400 m altitude near annapurna, nepal, 1999-2001, *Arctic, Antarctic, and Alpine Research*, *36*(2), 244–248.

Ramage, C. (1971), *Monsoon Meteorology*, 296 pp., International Geophysical Service, San Diego, CA.

Rango, A., and J. Martinec (1995), Revisiting the Degree-Day method for snowmelt computations, *Water Resources Bulletin*, *31*(4), 657–669.

Rao, S. V. N., M. V. Rao, and K. S. Ramasasitri (1997), A study of sedimentation in chenab basin in western himalayas, *Nordic Hydrology*, *28*(3), 201–216.

Rawat, J., M. Haigh, and M. Rawat (1992), Hydrological response of a himalayan pine forest micro-watershed, preliminary results., in *Proceedings of the International Symposium on Hydrology of Mountainous Areas*, pp. 28–30, Simla.

Raymo, M. E., and W. F. Ruddiman (1992), Tectonic forcing of late cenozoic climate, *Nature*, *359*(6391), 117–122.

Raymo, M. E., W. E. Ruddiman, and P. N. Froelich (1988), Influence of late cenozoic mountain building on ocean geochemical cycles., *Geology*, *16*, 649–653.

Reiners, P. W., T. A. Ehlers, S. G. Mitchell, and D. R. Montgomery (2003), Coupled spatial variations in precipitation and long-term erosion rates across the washington cascades, *Nature*, *426*(6967), 645–647.

Reiners, P. W., T. A. Ehlers, and P. K. Zeitler (2005), Past, present, and future of thermochronology, *Reviews in Mineralogy and Geochemistry*, *58*(1), 1–18.

Rodell, M., I. Velicogna, and J. S. Famiglietti (2009), Satellite-based estimates of groundwater depletion in india, *Nature*, *460*(7258), 999–1002.

Roe, G. H. (2003), Orographic precipitation and the relief of mountain ranges, *Journal of Geophysical Research*, *108*(B6).

Roe, G. H. (2005), Orographic precipitation, *Annual Review of Earth and Planetary Sciences*, *33*, 645–671.

Rolland, C. (2003), Spatial and seasonal variations of air temperature lapse rates in alpine regions, *Journal of Climate*, *16*, 1032–1046.

Rowley, D. B. (1996), Age of initiation of collision between india and asia: a review of stratigraphic data., *Earth Planetary Science Letters*, *145*, 1–13.

Salomonson, V., and Apple (2004), Estimating fractional snow cover from MODIS using the normalized difference snow index, *Remote Sensing of Environment*, *89*(3), 351–360.

Sapiano, M. R. P. (2009), An evaluation of high resolution precipitation products at low resolution, *International Journal of Climatology*, *30*(9), 1416–1422.

Schaefli, B., and H. V. Gupta (2007), Do nash values have value?, *Hydrological Processes*, *2080*, 2075–2080.

Scherler, D., B. Bookhagen, and M. R. Strecker (2011a), Spatially variable response of himalayan glaciers to climate change affected by debris cover, *Nature Geoscience*, *4*, 156–159, doi:10.1038/ngeo1068.

Scherler, D., B. Bookhagen, and M. R. Strecker (2011b), Hillslope-glacier coupling: the interplay of topography and glacial dynamics in high asia, *J. Geophys. Res.*, *116*(F02019), 21pp.

Seeber, L., and V. Gornitz (1983), River profiles along the himalayan arc as indicators of active tectonics, *Tectonophysics*, *92*(4), 335–337.

Seko, K. (1987), Seasonal variation of altitudinal dependence of precipitation in langtang valley, nepal himalayas, *Bullitin of Glacier Research*, *5*, 41–47.

Selby, M. (1980), A rock mass strength classification for geomorphic purposes: with tests from antarctica and new zealand, *Zeitschrift fur Geomorphologie*, *24*, 31–51.

Sharma, D. (2006), Floods and flash floods in himachal pradesh: A geographical analysis.

Shekhar, M. S., H. Chand, S. Kumar, K. Srinivasan, and A. Ganju (2010), Climate-change studies in the western himalaya, *Annals of Glaciology*, *51*(54), 105–112.

Sicart, J. E., R. Hock, and D. Six (2008), Glacier melt, air temperature, and energy balance in different climates: The bolivian tropics, the french alps, and northern sweden, *Journal of Geophysical Research*, *113*, D24,113.

Singh, P., and L. Bengtsson (2003), Effect of warmer climate on the depletion of snowcovered area in the satluj basin in the western himalayan region, *Hydrological Sciences Journal*, *48*(3), 413–425.

Singh, P., and L. Bengtsson (2004), Hydrological sensitivity of a large himalayan basin to climate change, *Hydrological Processes*, *18*(13), 2363–2385.

Singh, P., and S. K. Jain (2002), Snow and glacier melt in the satluj river at bhakra dam in the western himalayan region, *Hydrological Sciences Journal*, *47*(1), 93–106.

Singh, P., and S. K. Jain (2003), Modelling of streamflow and its components for a large himalayan basin with predominant snowmelt yields, *Hydrological Sciences Journal*, *48*(2), 257–276.

Singh, P., and N. Kumar (1997), Effect of orography on precipitation in the western himalayan region, *Journal of Hydrology*, *199*(1-2), 183–206.

Singh, P., G. Spitzbart, H. Hubl, and H. W. Weinmeister (1997), Hydrological response of snowpack under rain-on-snow events: a field study, *Journal of Hydrology*, *202*(1-4), 1–20.

Singh, P., K. S. Ramasatri, N. Kumar, and N. K. Bhatnagar (2003), Suspended sediment transport from the dokriani glacier in the garhwal himalayas, *Nordic Hydrology*, *34*(3), 221–244.

Sinha, R., and P. Friend (1994), River systems and their sediment flux, indo-gangetic plains, northern bihar, india, *Sedimentology*, *41*, 825–845.

SJVNL (2005), Concept paper on silt content in satluj river., *Tech. rep.*

Small, E. E., and R. Anderson (1995), Geomorphically driven late cenozoic rock uplift in the sierra nevada, california, *Science*, *270*, 277–280.

Stephens, G. L., R. D. Cess, M. H. Zhang, P. Pilewskie, and F. P. J. Valero (1996), How much solar radiation do clouds absorb?, *Science*, *271*(5252), 1131.

Stewart, R., B. Hallet, P. Zeitler, M. Malloy, C. Allen, and D. Trippett (2008), Brahmaputra sediment flux dominated by highly localized rapid erosion from the easternmost himalaya, *Geology*, *36*(9), 711–714.

Thayyen, R., J. Gergan, and D. Dobhal (2005), Slope lapse rates of temperature in Din Gad (Dokriani GIacier) catchment garhwal himalaya, lndia, *Bulletin of Glaciological Research*, *22*, 31–37.

Thayyen, R. J., J. T. Gergan, and D. P. Dobhal (2007), Role of glaciers and snow cover on headwater river hydrology in monsoon regime - micro-scale study of din gad catchment, garhwal himalaya, india, *Current Science*, *92*(3), 376–382.

Thiede, R. C., B. Bookhagen, J. R. Arrowsmith, E. R. Sobel, and M. R. Strecker (2004), Climatic control on rapid exhumation along the southern himalayan front, *Earth and Planetary Science Letters*, *222*(3-4), 791–806.

Tian, Y. D., et al. (2009), Component analysis of errors in satellite-based precipitation estimates, *Journal of Geophysical Research*, *114*, D24,101.1–15.

Vance, D., M. Bickle, S. Ivy-Ochs, and P. W. Kubik (2003), Erosion and exhumation in the himalaya from cosmogenic isotope inventories of river sediments, *Earth and Planetary Science Letters*, *206*(3-4), 273–288.

Vancutsem, C., P. Ceccato, T. Dinku, and S. J. Connor (2010), Evaluation of MODIS land surface temperature data to estimate air temperature in different ecosystems over africa, *Remote Sensing of Environment*, *114*(2), 449–465.

Vannay, J.-C., and B. Grasemann (1998), Inverted metamorphism in the high himalaya of himachal pradesh (nw india): Phase equilibria versus thermobarometry, *Schweizer Mineralogische und Petrographische Mitteilungen*, *78*, 107–132.

Vannay, J. C., B. Grasemann, M. Rahn, W. Frank, A. Carter, V. Baudraz, and M. Cosca (2004), Miocene to holocene exhumation of metamorphic crustal wedges in the NW himalaya: Evidence for tectonic extrusion coupled to fluvial erosion, *Tectonics*, *23*(1).

Viviroli, D., M. Zappa, J. Gurtz, and R. Weingartner (2009), An introduction to the hydrological modelling system PREVAH and its pre- and post-processing-tools, *Environmental Modelling & Software*, *24*(10), 1209–1222.

von Blanckenburg, F. (2005), The control mechanisms of erosion and weathering at basin scale from cosmogenic nuclides in river sediment, *Earth and Planetary Science Letters*, *237*(3-4), 462–479.

Wagnon, P., P. Ribstein, G. Kaser, and P. Berton (1999), Energy balance and runoff seasonality of a bolivian glacier, *Global and Planetary Change*, *22*(1-4), 49–58.

Wagnon, P., et al. (2007), Four years of mass balance on chhota shigri glacier, himachal pradesh, india, a new benchmark glacier in the western himalaya, *Journal of Glaciology*, *53*(183), 603–611.

Wan, Z. (2008), New refinements and validation of the MODIS Land-Surface Temperature/Emissivity products, *Remote Sensing of Environment*, *112*(1), 59–74.

Wan, Z., and J. Dozier (1996), A generalized split-window algorithm for retrieving land-surface temperature from space, *IEEE Transactions on Geoscience and Remote Sensing*, *34*(4), 892–905.

Wan, Z., Y. Zhang, and Q. Zhang (2004), Quality assessment and validation of the MODIS global land surface temperature, *International Journal of Remote Sensing*, *25*(1), 261–274.

WDI (2010), World bank, World Development Indicators, ESDS international, University of Manchester.

Webster, P., V. Magana, T. Palmer, J. Shukla, and R. Tomas (1998), Monsoons: processes, predictability, and the prospects for prediction, *Journal of Geophysical Research*, *103*, 14,451–14,510.

Webster, P. J., V. E. Toma, and H. Kim (2011), Were the 2010 pakistan floods predictable?, *Geophysical Research Letters*, *38*, L04,806, 5pp.

Weiers, S. (1995), Zur klimatologie des NW-Karakorum und angrenzender gebiete. statistische analysen unter einbeziehung von wettersatellitenbildern und eines geographischen informationssystems (GIS), *Bonner geographische Abhandlungen*, *92*(92), 169.

Wells, N., and J. Dorr (1987), Shifting of the kosi river, northern india, *Geology*, *15*, 204–207.

West, A. J., A. Galy, and M. Bickle (2005), Tectonic and climatic controls on silicate weathering, *Earth and Planetary Science Letters*, *235*(1-2), 211–228.

White, A. F., and A. E. Blum (1995), Effects of climate on chemical weathering in watersheds, *Geochimica et Cosmochimica Acta*, *59*(9), 1729–1747.

Winiger, M., M. Gumpert, and H. Yamout (2005), Karakorum-Hindukush-western himalaya: assessing high-altitude water resources, *Hydrological Processes*, *19*(12), 2329–2338.

WMO (1986), Intercomparison of models of snowmelt runoff, *Tech. rep.*, World Meteorological Organization.

Wobus, C., A. Heimsath, K. Whipple, and K. Hodges (2005), Active out-of-sequence thrust faulting in the central nepalese himalaya, *Nature*, *434*, 1008–1011.

Wohl, E., and D. Cenderelli (1988), *Flooding in the Himalaya Mountains*, pp. 77–99, Geological Society of India, Bangalore.

Wolman, M. G., and J. P. Miller (1960), Magnitude and frequency of forces in geomorphic processes, *Journal of Geology*, *68*(1), 54–74.

Wulf, H., B. Bookhagen, and D. Scherler (2010), Seasonal precipitation gradients and their impact on fluvial sediment flux in the northwest himalaya, *Geomorphology*, *118*(1-2), 13–21.

Wulf, H., B. Bookhagen, and D. Scherler (in review), Differentiating between rainfall, snow, and glacier contributions to river discharge in western himalaya using distributed hydrological modeling, *Water Resources Research*.

Yanai, M., C. Li, and Z. Song (1992), Seasonal heating of the tibetan plateau and its effects on the evolution of the asian summer monsoon., *Journal of the Meteorological Society of Japan*, *70*, 319–351.

Yao, T. D., X. J. Guo, L. Thompson, K. Q. Duan, N. L. Wang, J. C. Pu, B. Q. Xu, X. X. Yang, and W. Z. Sun (2006), delta o-18 record and temperature change over the past 100 years in ice cores on the tibetan plateau, *Global and Planetary Change*, *49*(1), 1–9.

Yasunari, T. (1976), Seasonal weather variations in khumbu himal, *Seppyo*, *38*, 74–83.

Yasunari, T., and J. Inoue (1978), Characteristics of monsoonal precipitation around peaks and ridges in shorong and khumbu himal, *Seppyo*, *40*, 26–32.

Yin, A., and T. Harrison (2000), Geologic evolution of the himalayan-tibetan orogen, *Annual Reviews of Earth Planetary Science*, *28*, 211–280.

Zeitler, P. K., et al. (2001), Erosion, himalayan tectonics and the geomorphology of metamorphism, *GSA Today*, *11*, 4–8.

Zhao, L., C. L. Ping, D. Q. Yang, G. D. Cheng, Y. J. Ding, and S. Y. Liu (2004), Changes of climate and seasonally frozen ground over the past 30 years in qinghai-xizang (tibetan) plateau, china, *Global and Planetary Change*, *43*(1-2), 19–31.

Appendix A: Weather station details

Table A.1: Location and data availability of weather stations in Himachal Pradesh operated by the Indian Meteorological Department (IMD) and the Bhakra Beas Management Board (BBMB). The weather stations are grouped by the orogenic front and the orogenic interior and sorted alphabetically.

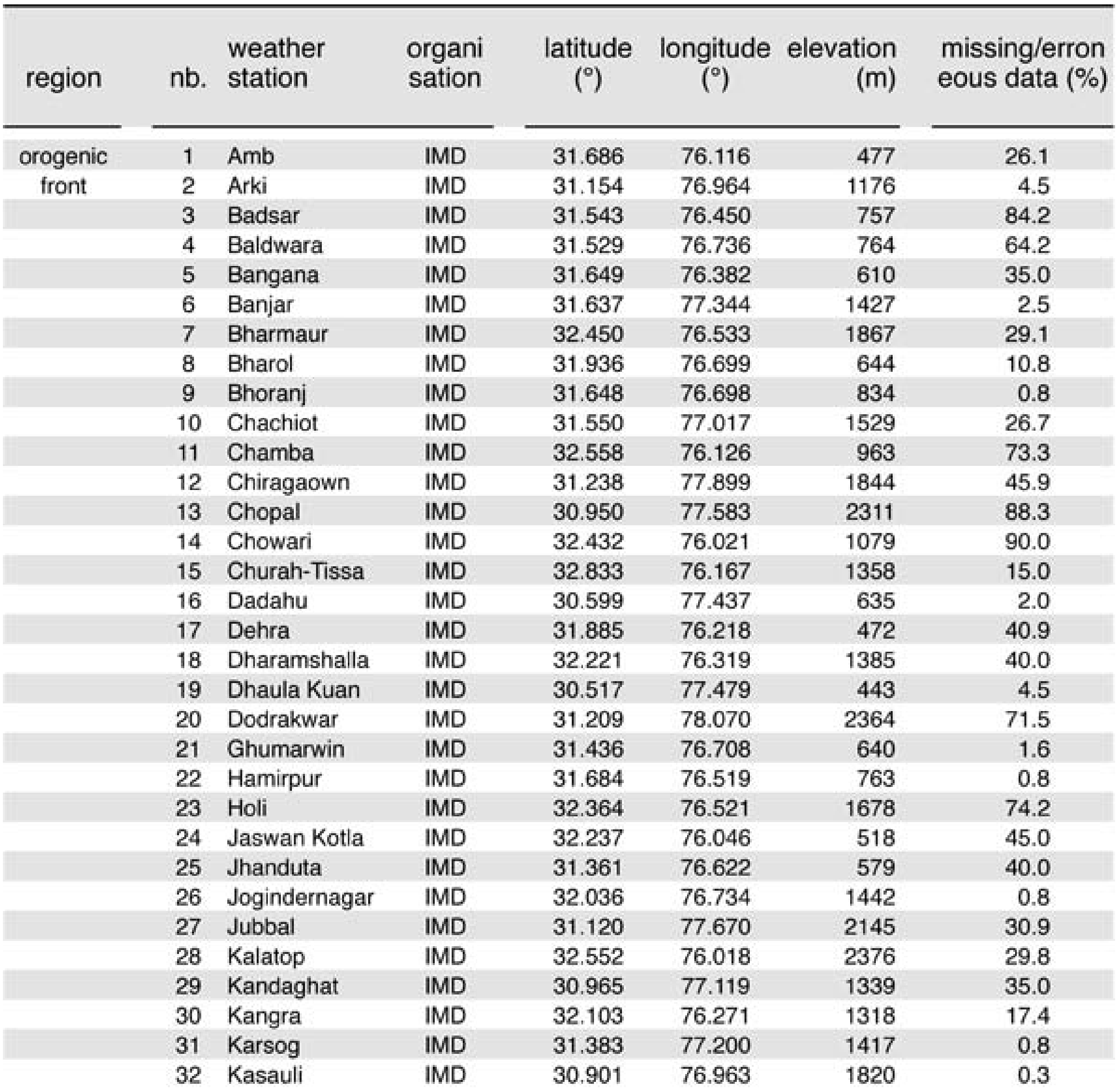

region	nb.	weather station	organi sation	latitude (°)	longitude (°)	elevation (m)	missing/erron eous data (%)
orogenic front	1	Amb	IMD	31.686	76.116	477	26.1
	2	Arki	IMD	31.154	76.964	1176	4.5
	3	Badsar	IMD	31.543	76.450	757	84.2
	4	Baldwara	IMD	31.529	76.736	764	64.2
	5	Bangana	IMD	31.649	76.382	610	35.0
	6	Banjar	IMD	31.637	77.344	1427	2.5
	7	Bharmaur	IMD	32.450	76.533	1867	29.1
	8	Bharol	IMD	31.936	76.699	644	10.8
	9	Bhoranj	IMD	31.648	76.698	834	0.8
	10	Chachiot	IMD	31.550	77.017	1529	26.7
	11	Chamba	IMD	32.558	76.126	963	73.3
	12	Chiragaown	IMD	31.238	77.899	1844	45.9
	13	Chopal	IMD	30.950	77.583	2311	88.3
	14	Chowari	IMD	32.432	76.021	1079	90.0
	15	Churah-Tissa	IMD	32.833	76.167	1358	15.0
	16	Dadahu	IMD	30.599	77.437	635	2.0
	17	Dehra	IMD	31.885	76.218	472	40.9
	18	Dharamshalla	IMD	32.221	76.319	1385	40.0
	19	Dhaula Kuan	IMD	30.517	77.479	443	4.5
	20	Dodrakwar	IMD	31.209	78.070	2364	71.5
	21	Ghumarwin	IMD	31.436	76.708	640	1.6
	22	Hamirpur	IMD	31.684	76.519	763	0.8
	23	Holi	IMD	32.364	76.521	1678	74.2
	24	Jaswan Kotla	IMD	32.237	76.046	518	45.0
	25	Jhanduta	IMD	31.361	76.622	579	40.0
	26	Jogindernagar	IMD	32.036	76.734	1442	0.8
	27	Jubbal	IMD	31.120	77.670	2145	30.9
	28	Kalatop	IMD	32.552	76.018	2376	29.8
	29	Kandaghat	IMD	30.965	77.119	1339	35.0
	30	Kangra	IMD	32.103	76.271	1318	17.4
	31	Karsog	IMD	31.383	77.200	1417	0.8
	32	Kasauli	IMD	30.901	76.963	1820	0.3

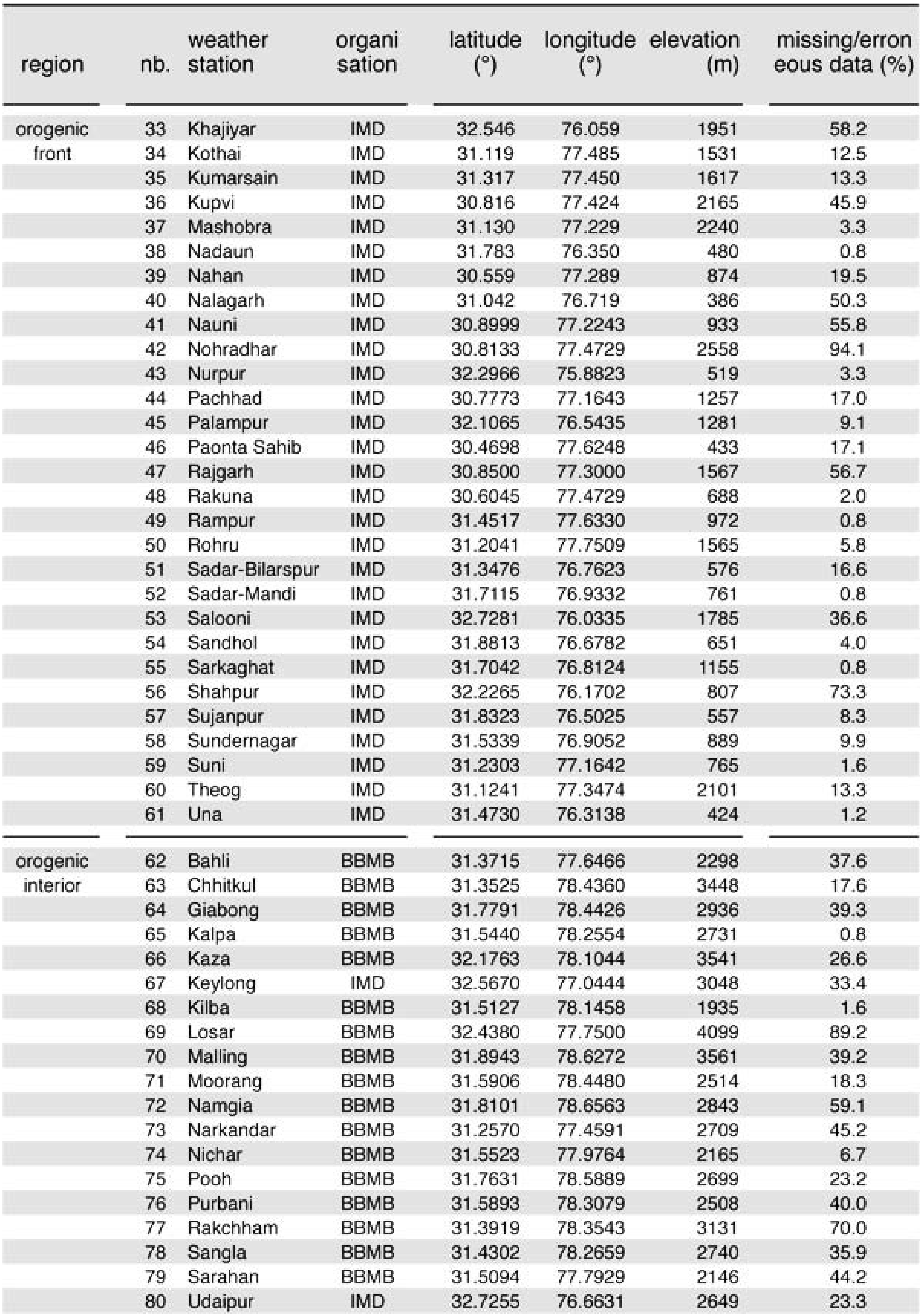

region	nb.	weather station	organi sation	latitude (°)	longitude (°)	elevation (m)	missing/erroneous data (%)
orogenic front	33	Khajiyar	IMD	32.546	76.059	1951	58.2
	34	Kothai	IMD	31.119	77.485	1531	12.5
	35	Kumarsain	IMD	31.317	77.450	1617	13.3
	36	Kupvi	IMD	30.816	77.424	2165	45.9
	37	Mashobra	IMD	31.130	77.229	2240	3.3
	38	Nadaun	IMD	31.783	76.350	480	0.8
	39	Nahan	IMD	30.559	77.289	874	19.5
	40	Nalagarh	IMD	31.042	76.719	386	50.3
	41	Nauni	IMD	30.8999	77.2243	933	55.8
	42	Nohradhar	IMD	30.8133	77.4729	2558	94.1
	43	Nurpur	IMD	32.2966	75.8823	519	3.3
	44	Pachhad	IMD	30.7773	77.1643	1257	17.0
	45	Palampur	IMD	32.1065	76.5435	1281	9.1
	46	Paonta Sahib	IMD	30.4698	77.6248	433	17.1
	47	Rajgarh	IMD	30.8500	77.3000	1567	56.7
	48	Rakuna	IMD	30.6045	77.4729	688	2.0
	49	Rampur	IMD	31.4517	77.6330	972	0.8
	50	Rohru	IMD	31.2041	77.7509	1565	5.8
	51	Sadar-Bilarspur	IMD	31.3476	76.7623	576	16.6
	52	Sadar-Mandi	IMD	31.7115	76.9332	761	0.8
	53	Salooni	IMD	32.7281	76.0335	1785	36.6
	54	Sandhol	IMD	31.8813	76.6782	651	4.0
	55	Sarkaghat	IMD	31.7042	76.8124	1155	0.8
	56	Shahpur	IMD	32.2265	76.1702	807	73.3
	57	Sujanpur	IMD	31.8323	76.5025	557	8.3
	58	Sundernagar	IMD	31.5339	76.9052	889	9.9
	59	Suni	IMD	31.2303	77.1642	765	1.6
	60	Theog	IMD	31.1241	77.3474	2101	13.3
	61	Una	IMD	31.4730	76.3138	424	1.2
orogenic interior	62	Bahli	BBMB	31.3715	77.6466	2298	37.6
	63	Chhitkul	BBMB	31.3525	78.4360	3448	17.6
	64	Giabong	BBMB	31.7791	78.4426	2936	39.3
	65	Kalpa	BBMB	31.5440	78.2554	2731	0.8
	66	Kaza	BBMB	32.1763	78.1044	3541	26.6
	67	Keylong	IMD	32.5670	77.0444	3048	33.4
	68	Kilba	BBMB	31.5127	78.1458	1935	1.6
	69	Losar	BBMB	32.4380	77.7500	4099	89.2
	70	Malling	BBMB	31.8943	78.6272	3561	39.2
	71	Moorang	BBMB	31.5906	78.4480	2514	18.3
	72	Namgia	BBMB	31.8101	78.6563	2843	59.1
	73	Narkandar	BBMB	31.2570	77.4591	2709	45.2
	74	Nichar	BBMB	31.5523	77.9764	2165	6.7
	75	Pooh	BBMB	31.7631	78.5889	2699	23.2
	76	Purbani	BBMB	31.5893	78.3079	2508	40.0
	77	Rakchham	BBMB	31.3919	78.3543	3131	70.0
	78	Sangla	BBMB	31.4302	78.2659	2740	35.9
	79	Sarahan	BBMB	31.5094	77.7929	2146	44.2
	80	Udaipur	IMD	32.7255	76.6631	2649	23.3

Appendix B: Supplementary material for Chapter 4

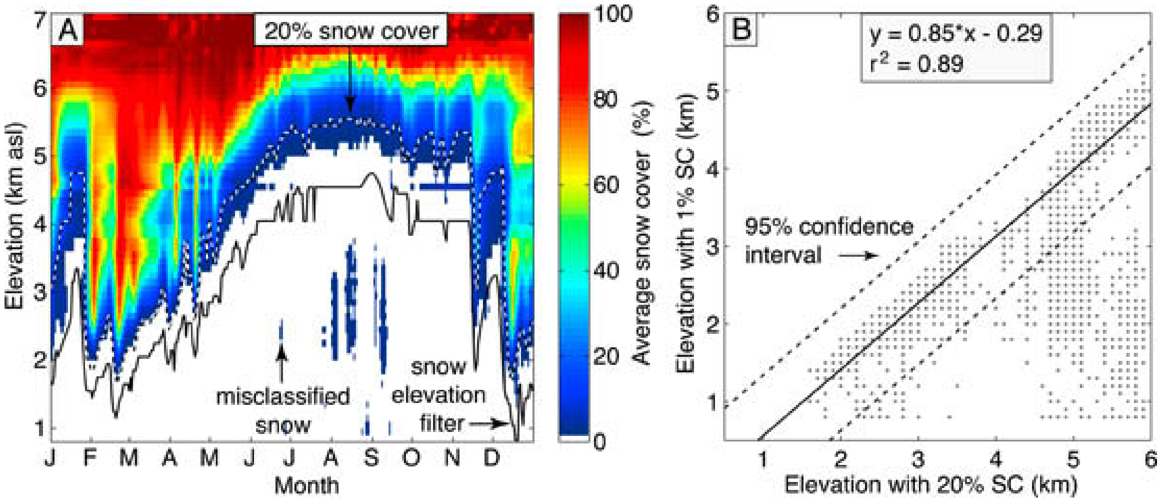

Figure B.1: (A) Average snow cover (SC) at each 0.1 km elevation interval between 0.9 and 7.2 km during the year 2003. Solid white line represents the snow-cover elevation filter for snow/cloud confusions. (B) Weighted regression of elevation intervals of 0.1 km with >1% versus >20% average snow cover during the years 2000 to 2008. Clouds misclassified as snow occur predominantly during the Indian summer monsoon at elevations below 4 km.

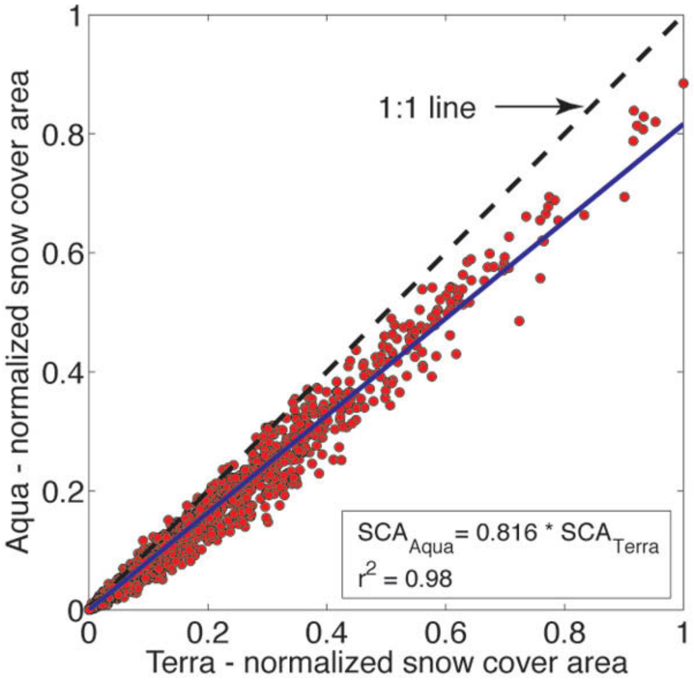

Figure B.2: Comparison of the normalized snow cover area (SCA) obtained by MODIS Terra and Aqua satellites of identical cloud free subsets within the study area. The Aqua satellite consistently underestimates the SCA of Terra by a factor of 0.816 ± 0.004. For all dual daily snow observation in our study area from 2002 to 2008 we found a lower (higher) FSC by Aqua in 64.4% (22.8%) of all cases.

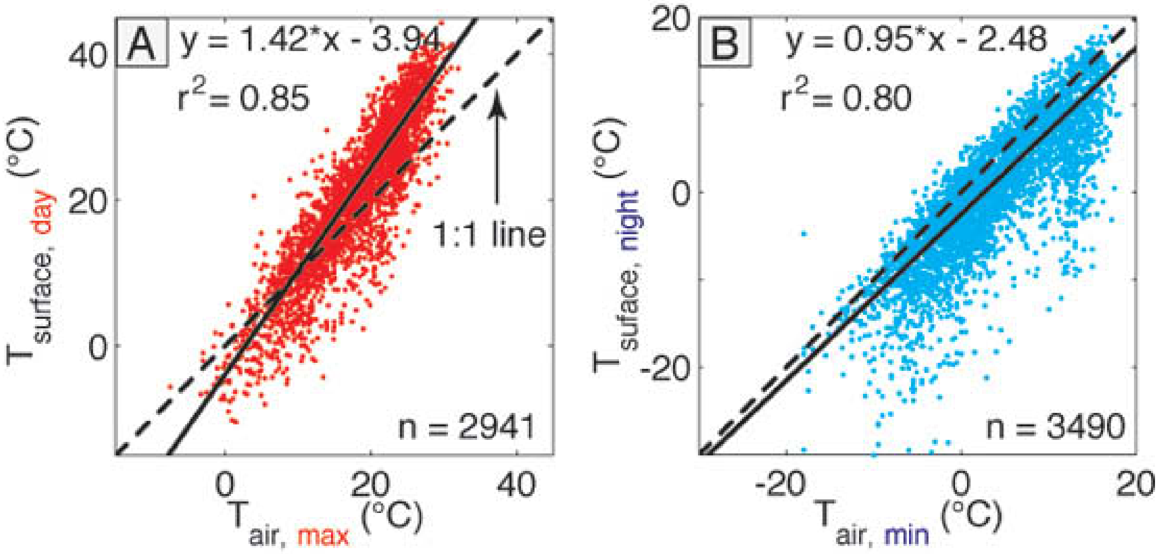

Figure B.3: (A) Linear regression of daily maximum air temperatures from Kalpa, Rakchham, and Namgia (cf. Figure 4.1) versus daytime MODIS Aqua land surface temperatures (Tsurface) weighted by the satellite sensor angle. (B) Same regression as in A for air minimum temperatures versus MODIS Terra nighttime surface temperatures.

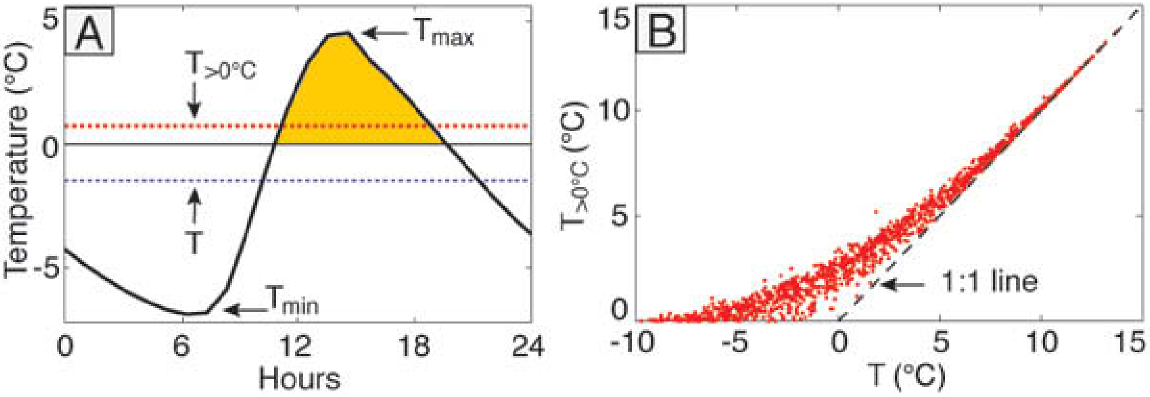

Figure B.4: (A) Diurnal temperature cycle recorded by the automated weather station (WS) on February 2, 2008 in Khab (cf. Figure 4.1). Hourly temperatures above zero (shaded in grey) account for daily melt. Therefore, we drive melt by the daily mean positive temperature (T>0°C) instead of the mean daily temperatures (T). (B) Example of the temperature distribution between T and T>0°C based on MODIS data from 2000 to 2008.

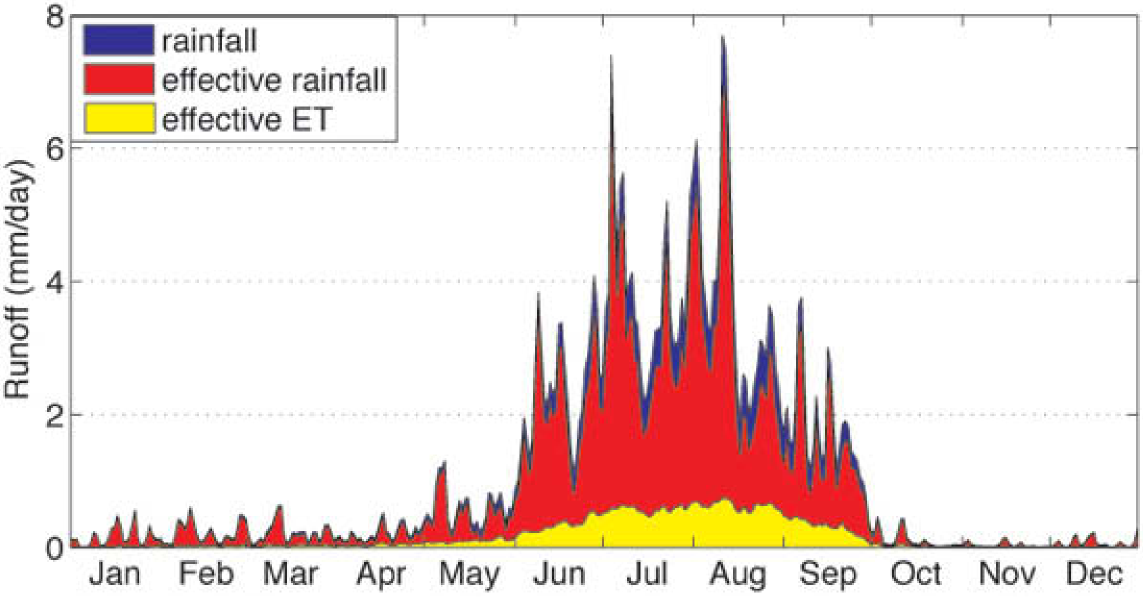

Figure B.5: (A) Mean annual rainfall and evapotranspiration (ET) cycle in the Sutlej Catchment. Runoff by effective rainfall takes evapotranspiration losses into account, which amount to 16% of the mean annual rainfall. The mean annual effective evapotranspiration in the Sutlej Valley is 14.8 mm/m2.

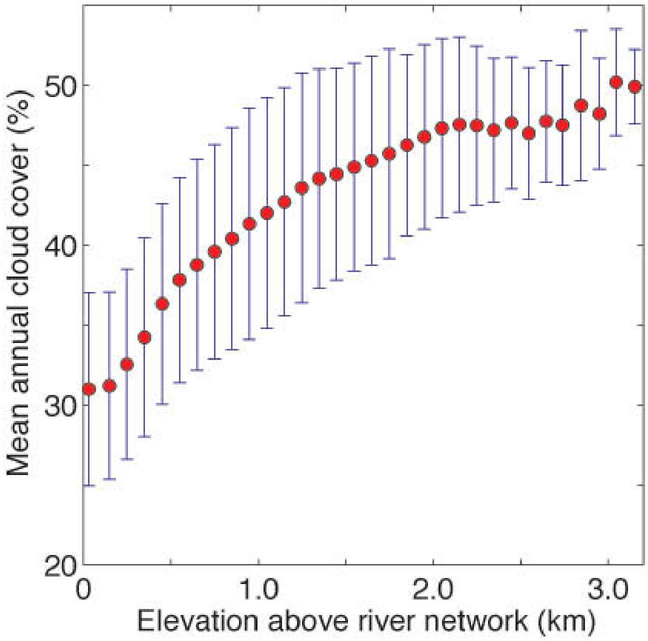

Figure B.6: Distribution of cloud cover in the Sutlej Valley with respect to elevations above the river network. Cloud cover increases from the valley floor to the mountaintop throughout the study area.

Appendix C: Earthquake details

Table C.1: List of earthquakes in the study area. Data provided by the Incorporated Research Institutions for Seismology (http://www.iris.washington.edu). Abbreviations of the magnitude types indicate the moment magnitude (MW), body-wave magnitude (MB), and surface-wave magnitude (MS). Abbreviations of the earthquake catalogues indicate the Bulletin of the International Seismological Centre (ISCCD), Quick Epicenter Determinations (QED), Monthly Hypocenter Data File (MHDF), Weekly Hypocenter Data File (WHDF), a list distributed by the National Earthquake Information Service (FINGER), and historical earthquake data listed in a hydropower project report (www.powermin.nic.in/whats_new/PFR/HP/Luhri_Hep.pdf).

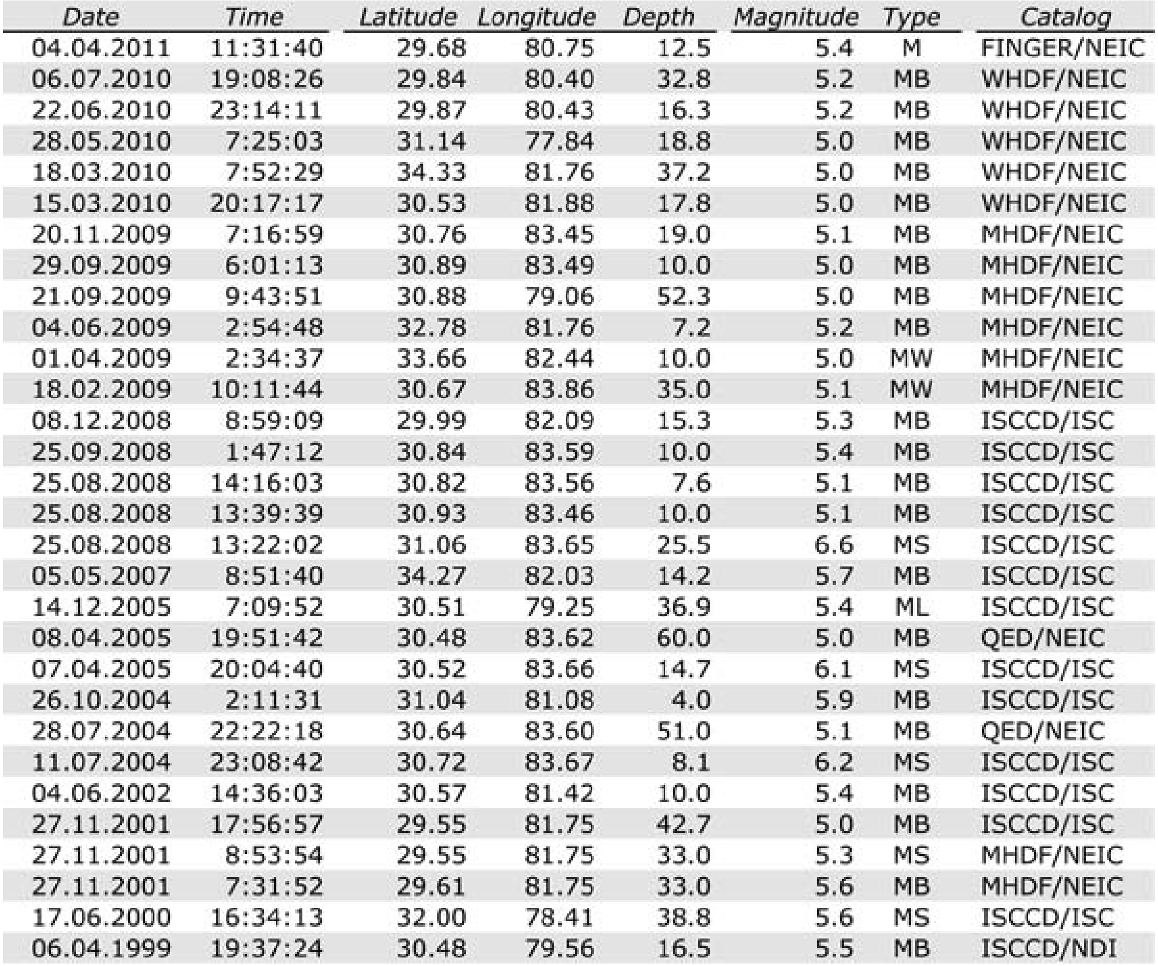

Date	Time	Latitude	Longitude	Depth	Magnitude	Type	Catalog
04.04.2011	11:31:40	29.68	80.75	12.5	5.4	M	FINGER/NEIC
06.07.2010	19:08:26	29.84	80.40	32.8	5.2	MB	WHDF/NEIC
22.06.2010	23:14:11	29.87	80.43	16.3	5.2	MB	WHDF/NEIC
28.05.2010	7:25:03	31.14	77.84	18.8	5.0	MB	WHDF/NEIC
18.03.2010	7:52:29	34.33	81.76	37.2	5.0	MB	WHDF/NEIC
15.03.2010	20:17:17	30.53	81.88	17.8	5.0	MB	WHDF/NEIC
20.11.2009	7:16:59	30.76	83.45	19.0	5.1	MB	MHDF/NEIC
29.09.2009	6:01:13	30.89	83.49	10.0	5.0	MB	MHDF/NEIC
21.09.2009	9:43:51	30.88	79.06	52.3	5.0	MB	MHDF/NEIC
04.06.2009	2:54:48	32.78	81.76	7.2	5.2	MB	MHDF/NEIC
01.04.2009	2:34:37	33.66	82.44	10.0	5.0	MW	MHDF/NEIC
18.02.2009	10:11:44	30.67	83.86	35.0	5.1	MW	MHDF/NEIC
08.12.2008	8:59:09	29.99	82.09	15.3	5.3	MB	ISCCD/ISC
25.09.2008	1:47:12	30.84	83.59	10.0	5.4	MB	ISCCD/ISC
25.08.2008	14:16:03	30.82	83.56	7.6	5.1	MB	ISCCD/ISC
25.08.2008	13:39:39	30.93	83.46	10.0	5.1	MB	ISCCD/ISC
25.08.2008	13:22:02	31.06	83.65	25.5	6.6	MS	ISCCD/ISC
05.05.2007	8:51:40	34.27	82.03	14.2	5.7	MB	ISCCD/ISC
14.12.2005	7:09:52	30.51	79.25	36.9	5.4	ML	ISCCD/ISC
08.04.2005	19:51:42	30.48	83.62	60.0	5.0	MB	QED/NEIC
07.04.2005	20:04:40	30.52	83.66	14.7	6.1	MS	ISCCD/ISC
26.10.2004	2:11:31	31.04	81.08	4.0	5.9	MB	ISCCD/ISC
28.07.2004	22:22:18	30.64	83.60	51.0	5.1	MB	QED/NEIC
11.07.2004	23:08:42	30.72	83.67	8.1	6.2	MS	ISCCD/ISC
04.06.2002	14:36:03	30.57	81.42	10.0	5.4	MB	ISCCD/ISC
27.11.2001	17:56:57	29.55	81.75	42.7	5.0	MB	ISCCD/ISC
27.11.2001	8:53:54	29.55	81.75	33.0	5.3	MS	MHDF/NEIC
27.11.2001	7:31:52	29.61	81.75	33.0	5.6	MB	MHDF/NEIC
17.06.2000	16:34:13	32.00	78.41	38.8	5.6	MS	ISCCD/ISC
06.04.1999	19:37:24	30.48	79.56	16.5	5.5	MB	ISCCD/NDI

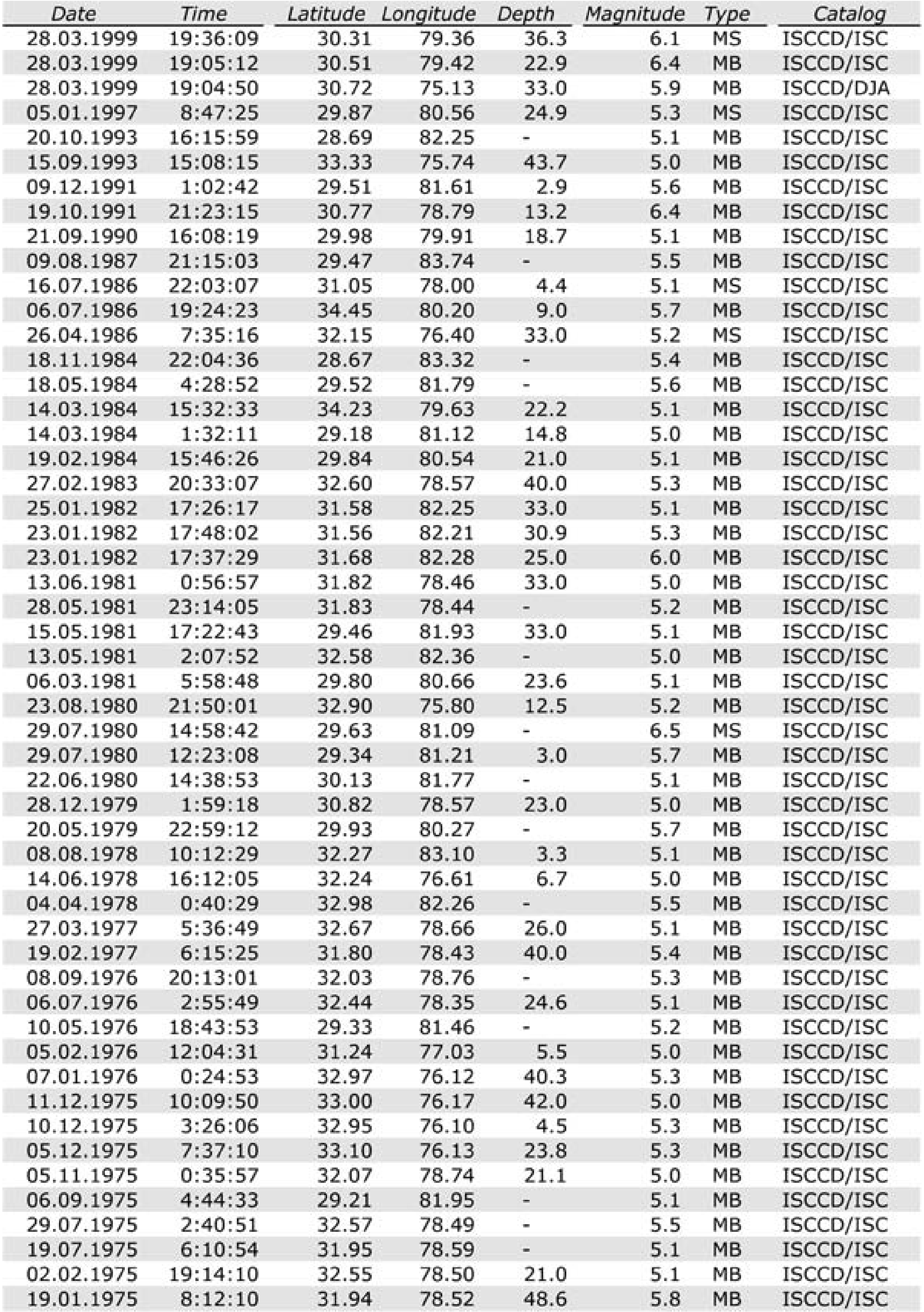

Date	Time	Latitude	Longitude	Depth	Magnitude	Type	Catalog
28.03.1999	19:36:09	30.31	79.36	36.3	6.1	MS	ISCCD/ISC
28.03.1999	19:05:12	30.51	79.42	22.9	6.4	MB	ISCCD/ISC
28.03.1999	19:04:50	30.72	75.13	33.0	5.9	MB	ISCCD/DJA
05.01.1997	8:47:25	29.87	80.56	24.9	5.3	MS	ISCCD/ISC
20.10.1993	16:15:59	28.69	82.25	-	5.1	MB	ISCCD/ISC
15.09.1993	15:08:15	33.33	75.74	43.7	5.0	MB	ISCCD/ISC
09.12.1991	1:02:42	29.51	81.61	2.9	5.6	MB	ISCCD/ISC
19.10.1991	21:23:15	30.77	78.79	13.2	6.4	MB	ISCCD/ISC
21.09.1990	16:08:19	29.98	79.91	18.7	5.1	MB	ISCCD/ISC
09.08.1987	21:15:03	29.47	83.74	-	5.5	MB	ISCCD/ISC
16.07.1986	22:03:07	31.05	78.00	4.4	5.1	MS	ISCCD/ISC
06.07.1986	19:24:23	34.45	80.20	9.0	5.7	MB	ISCCD/ISC
26.04.1986	7:35:16	32.15	76.40	33.0	5.2	MS	ISCCD/ISC
18.11.1984	22:04:36	28.67	83.32	-	5.4	MB	ISCCD/ISC
18.05.1984	4:28:52	29.52	81.79	-	5.6	MB	ISCCD/ISC
14.03.1984	15:32:33	34.23	79.63	22.2	5.1	MB	ISCCD/ISC
14.03.1984	1:32:11	29.18	81.12	14.8	5.0	MB	ISCCD/ISC
19.02.1984	15:46:26	29.84	80.54	21.0	5.1	MB	ISCCD/ISC
27.02.1983	20:33:07	32.60	78.57	40.0	5.3	MB	ISCCD/ISC
25.01.1982	17:26:17	31.58	82.25	33.0	5.1	MB	ISCCD/ISC
23.01.1982	17:48:02	31.56	82.21	30.9	5.3	MB	ISCCD/ISC
23.01.1982	17:37:29	31.68	82.28	25.0	6.0	MB	ISCCD/ISC
13.06.1981	0:56:57	31.82	78.46	33.0	5.0	MB	ISCCD/ISC
28.05.1981	23:14:05	31.83	78.44	-	5.2	MB	ISCCD/ISC
15.05.1981	17:22:43	29.46	81.93	33.0	5.1	MB	ISCCD/ISC
13.05.1981	2:07:52	32.58	82.36	-	5.0	MB	ISCCD/ISC
06.03.1981	5:58:48	29.80	80.66	23.6	5.1	MB	ISCCD/ISC
23.08.1980	21:50:01	32.90	75.80	12.5	5.2	MB	ISCCD/ISC
29.07.1980	14:58:42	29.63	81.09	-	6.5	MS	ISCCD/ISC
29.07.1980	12:23:08	29.34	81.21	3.0	5.7	MB	ISCCD/ISC
22.06.1980	14:38:53	30.13	81.77	-	5.1	MB	ISCCD/ISC
28.12.1979	1:59:18	30.82	78.57	23.0	5.0	MB	ISCCD/ISC
20.05.1979	22:59:12	29.93	80.27	-	5.7	MB	ISCCD/ISC
08.08.1978	10:12:29	32.27	83.10	3.3	5.1	MB	ISCCD/ISC
14.06.1978	16:12:05	32.24	76.61	6.7	5.0	MB	ISCCD/ISC
04.04.1978	0:40:29	32.98	82.26	-	5.5	MB	ISCCD/ISC
27.03.1977	5:36:49	32.67	78.66	26.0	5.1	MB	ISCCD/ISC
19.02.1977	6:15:25	31.80	78.43	40.0	5.4	MB	ISCCD/ISC
08.09.1976	20:13:01	32.03	78.76	-	5.3	MB	ISCCD/ISC
06.07.1976	2:55:49	32.44	78.35	24.6	5.1	MB	ISCCD/ISC
10.05.1976	18:43:53	29.33	81.46	-	5.2	MB	ISCCD/ISC
05.02.1976	12:04:31	31.24	77.03	5.5	5.0	MB	ISCCD/ISC
07.01.1976	0:24:53	32.97	76.12	40.3	5.3	MB	ISCCD/ISC
11.12.1975	10:09:50	33.00	76.17	42.0	5.0	MB	ISCCD/ISC
10.12.1975	3:26:06	32.95	76.10	4.5	5.3	MB	ISCCD/ISC
05.12.1975	7:37:10	33.10	76.13	23.8	5.3	MB	ISCCD/ISC
05.11.1975	0:35:57	32.07	78.74	21.1	5.0	MB	ISCCD/ISC
06.09.1975	4:44:33	29.21	81.95	-	5.1	MB	ISCCD/ISC
29.07.1975	2:40:51	32.57	78.49	-	5.5	MB	ISCCD/ISC
19.07.1975	6:10:54	31.95	78.59	-	5.1	MB	ISCCD/ISC
02.02.1975	19:14:10	32.55	78.50	21.0	5.1	MB	ISCCD/ISC
19.01.1975	8:12:10	31.94	78.52	48.6	5.8	MB	ISCCD/ISC

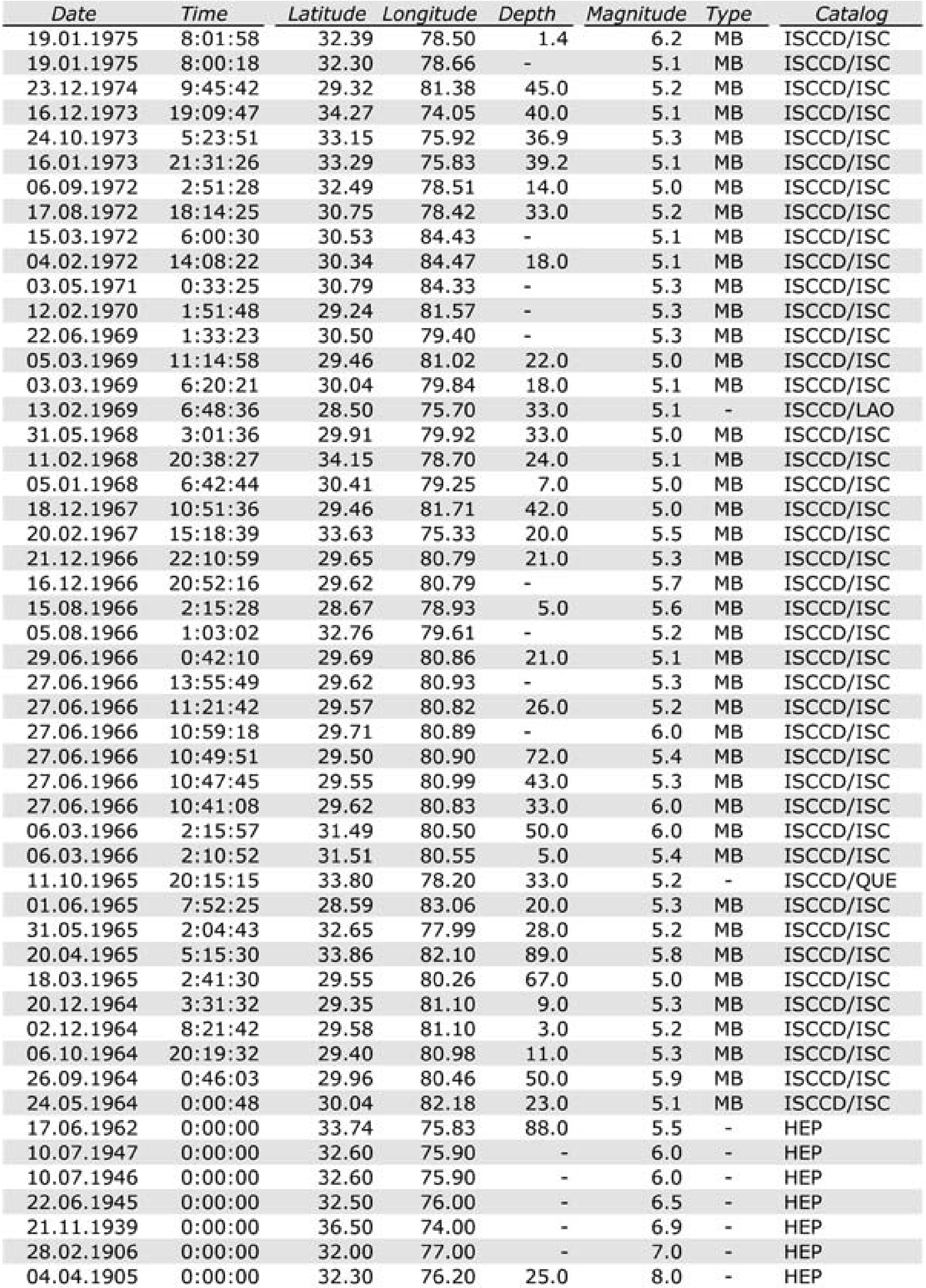

Date	Time	Latitude	Longitude	Depth	Magnitude	Type	Catalog
19.01.1975	8:01:58	32.39	78.50	1.4	6.2	MB	ISCCD/ISC
19.01.1975	8:00:18	32.30	78.66	-	5.1	MB	ISCCD/ISC
23.12.1974	9:45:42	29.32	81.38	45.0	5.2	MB	ISCCD/ISC
16.12.1973	19:09:47	34.27	74.05	40.0	5.1	MB	ISCCD/ISC
24.10.1973	5:23:51	33.15	75.92	36.9	5.3	MB	ISCCD/ISC
16.01.1973	21:31:26	33.29	75.83	39.2	5.1	MB	ISCCD/ISC
06.09.1972	2:51:28	32.49	78.51	14.0	5.0	MB	ISCCD/ISC
17.08.1972	18:14:25	30.75	78.42	33.0	5.2	MB	ISCCD/ISC
15.03.1972	6:00:30	30.53	84.43	-	5.1	MB	ISCCD/ISC
04.02.1972	14:08:22	30.34	84.47	18.0	5.1	MB	ISCCD/ISC
03.05.1971	0:33:25	30.79	84.33	-	5.3	MB	ISCCD/ISC
12.02.1970	1:51:48	29.24	81.57	-	5.3	MB	ISCCD/ISC
22.06.1969	1:33:23	30.50	79.40	-	5.3	MB	ISCCD/ISC
05.03.1969	11:14:58	29.46	81.02	22.0	5.0	MB	ISCCD/ISC
03.03.1969	6:20:21	30.04	79.84	18.0	5.1	MB	ISCCD/ISC
13.02.1969	6:48:36	28.50	75.70	33.0	5.1	-	ISCCD/LAO
31.05.1968	3:01:36	29.91	79.92	33.0	5.0	MB	ISCCD/ISC
11.02.1968	20:38:27	34.15	78.70	24.0	5.1	MB	ISCCD/ISC
05.01.1968	6:42:44	30.41	79.25	7.0	5.0	MB	ISCCD/ISC
18.12.1967	10:51:36	29.46	81.71	42.0	5.0	MB	ISCCD/ISC
20.02.1967	15:18:39	33.63	75.33	20.0	5.5	MB	ISCCD/ISC
21.12.1966	22:10:59	29.65	80.79	21.0	5.3	MB	ISCCD/ISC
16.12.1966	20:52:16	29.62	80.79	-	5.7	MB	ISCCD/ISC
15.08.1966	2:15:28	28.67	78.93	5.0	5.6	MB	ISCCD/ISC
05.08.1966	1:03:02	32.76	79.61	-	5.2	MB	ISCCD/ISC
29.06.1966	0:42:10	29.69	80.86	21.0	5.1	MB	ISCCD/ISC
27.06.1966	13:55:49	29.62	80.93	-	5.3	MB	ISCCD/ISC
27.06.1966	11:21:42	29.57	80.82	26.0	5.2	MB	ISCCD/ISC
27.06.1966	10:59:18	29.71	80.89	-	6.0	MB	ISCCD/ISC
27.06.1966	10:49:51	29.50	80.90	72.0	5.4	MB	ISCCD/ISC
27.06.1966	10:47:45	29.55	80.99	43.0	5.3	MB	ISCCD/ISC
27.06.1966	10:41:08	29.62	80.83	33.0	6.0	MB	ISCCD/ISC
06.03.1966	2:15:57	31.49	80.50	50.0	6.0	MB	ISCCD/ISC
06.03.1966	2:10:52	31.51	80.55	5.0	5.4	MB	ISCCD/ISC
11.10.1965	20:15:15	33.80	78.20	33.0	5.2	-	ISCCD/QUE
01.06.1965	7:52:25	28.59	83.06	20.0	5.3	MB	ISCCD/ISC
31.05.1965	2:04:43	32.65	77.99	28.0	5.2	MB	ISCCD/ISC
20.04.1965	5:15:30	33.86	82.10	89.0	5.8	MB	ISCCD/ISC
18.03.1965	2:41:30	29.55	80.26	67.0	5.0	MB	ISCCD/ISC
20.12.1964	3:31:32	29.35	81.10	9.0	5.3	MB	ISCCD/ISC
02.12.1964	8:21:42	29.58	81.10	3.0	5.2	MB	ISCCD/ISC
06.10.1964	20:19:32	29.40	80.98	11.0	5.3	MB	ISCCD/ISC
26.09.1964	0:46:03	29.96	80.46	50.0	5.9	MB	ISCCD/ISC
24.05.1964	0:00:48	30.04	82.18	23.0	5.1	MB	ISCCD/ISC
17.06.1962	0:00:00	33.74	75.83	88.0	5.5	-	HEP
10.07.1947	0:00:00	32.60	75.90	-	6.0	-	HEP
10.07.1946	0:00:00	32.60	75.90	-	6.0	-	HEP
22.06.1945	0:00:00	32.50	76.00	-	6.5	-	HEP
21.11.1939	0:00:00	36.50	74.00	-	6.9	-	HEP
28.02.1906	0:00:00	32.00	77.00	-	7.0	-	HEP
04.04.1905	0:00:00	32.30	76.20	25.0	8.0	-	HEP